CHEMICAL REVIEWS

pubs.acs.org/CR

Review

Rechargeable Alkali-Ion Battery Materials: Theory and Computation

Anton Van der Ven,* Zhi Deng, Swastika Banerjee, and Shyue Ping Ong*

Cite This: *Chem. Rev.* 2020, 120, 6977–7019

Read Online

ABSTRACT: Since its development in the 1970s, the rechargeable alkali-ion battery has proven to be a truly transformative technology, providing portable energy storage for devices ranging from small portable electronics to sizable electric vehicles. Here, we present a review of modern theoretical and computational approaches to the study and design of rechargeable alkali-ion battery materials. Starting from fundamental thermodynamics and kinetics phenomenological equations, we rigorously derive the theoretical relationships for key battery properties, such as voltage, capacity, alkali diffusivity, and other electrochemically relevant computable quantities. We then present an overview of computational techniques for the study of rechargeable alkali-ion battery materials, followed by a critical review of the literature applying these techniques to yield crucial insights into battery operation and performance. Finally, we provide perspectives on outstanding challenges and opportunities in the theory and computation of rechargeable alkali-ion battery materials.

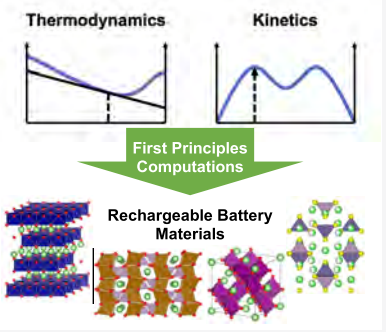

CONTENTS

Special Issue: Beyond Li-Ion Battery Chemistry

Received: September 23, 2019
Published: February 5, 2020

https://dx.doi.org/10.1021/acs.chemrev.9b00601
Chem. Rev. 2020, 120, 6977–7019

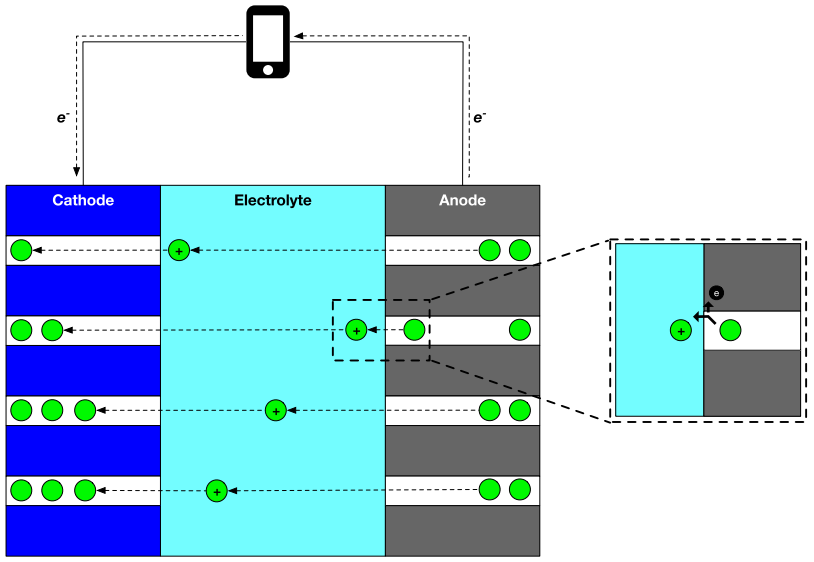

Figure 1. Schematic of a rechargeable battery during the discharging process. Green circles indicate the mobile ions (e.g., Li^+, Na^+, Mg^{2+}). During charge, the direction of the mobile ion migration is reversed.

1. INTRODUCTION

The rechargeable lithium-ion battery (LIB)[1] is one of the key enablers of the modern age. With an unrivaled combination of portability and energy density, LIBs are ubiquitous in consumer electronics such as cell phones and laptops and are the leading energy storage candidate for the clean energy grid and the electrification of transportation. It is therefore unsurprising that LIBs and closely related modifications based on other alkali and multivalent ions (e.g., Na^+, K^+, Mg^{2+}, Ca^{2+}) have been the subject of extensive research since the 1970s up to the present day, of which there are many extensive reviews on the topic.[2−4]

This review will focus on a relatively modern arsenal in rechargeable battery materials research: first-principles or ab initio calculations. In the parlance of computational materials science, first-principles calculations refer to methods that approximate solutions to the quantum mechanical Schrödinger equation (such as density functional theory or DFT)[5,6] using computers, which can be combined with thermodynamics and kinetics phenomenological equations to predict the properties of a collection of atoms. Although the development of such methods precedes the discovery of the LIB, it is only in recent decades that methodological,[7,8] software,[9] and computing advances have made their application to the study and prediction of materials properties over diverse chemistries practical and scalable.[10] The scope of this review includes all rechargeable alkali-ion batteries working on the rocking-chair mechanism (LIBs and its relatives) but is focused on first-principles techniques only. The aim is to elucidate the theoretical foundations behind the prediction of battery properties, with a smaller emphasis placed on the specific methodologies (e.g., choice of DFT functional or parameters) used for their computation.

The modern-day rechargeable battery, as shown in Figure 1, is a device that stores energy through a chemical process in which a mobile ion (e.g., Li^+, Na^+) is reversibly shuttled between two electrodes through an electronically insulating and ionically conducting electrolyte. Typically, the electrodes are intercalation compounds that store the mobile ions in a topotactic manner within a host lattice,[2] although some electrodes operate via a conversion/alloying mechanism.[11,12] During discharge, the ions are transported from the anode through the electrolyte to the cathode, releasing electrons to perform electrical work in an external circuit in the process. During charge, an applied voltage reverses this ion migration process. Throughout this review, the cathode is defined as the positive electrode during discharge, as per the typical convention used in the literature. The majority of cathodes are transition metal oxides and chalcogenides, where the insertion/removal of the ion is accompanied by the reduction/oxidation of a transition metal ion. Anodes are typically various forms of carbon or alloys and, in selected cases, made by the active metal. The electrolyte is usually an organic solvent (e.g., carbonates or ethers) with an added salt (e.g., $LiPF_6$),[13] although polymers and, more recently, ceramic superionic conductors[14−16] can be used in an all-solid-state battery architecture.

A rechargeable battery should ideally have high gravimetric and volumetric energy density, high rate capability (power), long cycle life, good safety, and low cost. The gravimetric and volumetric energy density are governed by the average voltage of the battery and the capacity (number of mobile ions that can be stored per unit weight or volume), while the rate capability is governed by the kinetics of the ion and electron transport. The cycle life is governed by the reversibility of the charge/discharge process at the materials as well as device level. The remainder of this review is structured as follows:

- In section 2, we will first develop a firm theoretical foundation for various battery properties and how these properties relate to computable thermodynamic and kinetic quantities.
- In section 3, we will delve into the specific computational techniques used to calculate battery properties. We will start with a brief introduction to density functional theory (DFT),[5,6] the current workhorse approach to solve the Schrödinger equation, followed by an exposition of how the outputs of DFT computations can be used with various simulation methodologies to obtain battery properties.
- In section 4, we will review how DFT-based computational techniques have been applied in providing insights

https://dx.doi.org/10.1021/acs.chemrev.9b00601
Chem. Rev. 2020, 120, 6977−7019

into battery electrodes and electrolytes. Owing to the vast body of research on rechargeable batteries, our review will focus on selected *advanced* computational studies where DFT calculations are utilized in conjunction with other computational techniques and analysis (e.g., Monte Carlo, molecular dynamics) to provide deep insights into battery properties.

- Finally, we conclude this review by providing perspectives on outstanding challenges and opportunities for theoretical modeling of rechargable alkali-ion batteries.

2. THEORY

Throughout this section, we will derive the key relationships and equations using the most common lithium-ion battery chemistry where Li^+ is the main mobile species. All equations can be modified for other mobile species.

2.1. Thermodynamics of Rechargeable Batteries

2.1.1. Equilibrium and the Nernst Equation. The open circuit voltage (OCV) of an electrochemical cell is a thermodynamic quantity. It is the voltage across the electrodes when the battery as a whole, consisting of anode, cathode and electrolyte, has reached equilibrium. Equilibrium at constant temperature, pressure, and number of atoms within the battery occurs when the total Gibbs free energy has reached a minimum with respect to internal degrees of freedom. As a concrete example, consider the rechargeable LIB shown in Figure 1. The electrolyte only allows the passage of Li^+ cations but prevents the passage of electrons. Any Li that migrates from the anode to the cathode must leave behind an electron in the anode and create an electron hole in the cathode (inset of Figure 1). The imbalance of charge within the individual electrodes produces a difference in electrostatic potential within the various components of the battery until electrostatic forces counter the chemical forces that drive Li from anode to cathode.

In treating the thermodynamics of a Li-ion shuttle battery, we follow the approach of Radin et al.[17] To this end, it is convenient to introduce five internal degrees of freedom: $N^{C}_{Li^+}$, $N^{A}_{Li^+}$, and $N^{E}_{Li^+}$, which refer to the number of Li^+ in the cathode, anode, and electrolyte respectively and $N^{C}_{e^-}$ and $N^{A}_{e^-}$, which track the number of valence electrons in the cathode and anode, respectively. When the electrode and electrolyte phases are individually large relative to surfaces and interfaces, it is possible to express the total Gibbs free energy of the battery as a sum of the free energies of the individual components as

$$G(N^{C}_{Li^+}, N^{A}_{Li^+}, N^{E}_{Li^+}, N^{C}_{e^-}, N^{A}_{e^-}) = G^{C}(N^{C}_{Li^+}, N^{C}_{e^-}) + G^{A}(N^{A}_{Li^+}, N^{A}_{e^-}) + G^{E}(N^{E}_{Li^+}) \quad (1)$$

where an implicit dependence on temperature T, pressure P, and number of atoms of the other components is assumed. Additional surface and interface free energies must be included in the sum of eq 1 if the electrode particles adopt nano-dimensions[18,19] or for supercapacitors where the electrode/electrolyte interface area is maximized.

The Li *electrochemical* potential in a particular phase α, i.e., anode, cathode, or electrolyte, is defined as

$$\eta^{\alpha}_{Li^+} = \frac{\partial G^{\alpha}}{\partial N^{\alpha}_{Li^+}} \quad (2)$$

where the partial derivative is taken holding all other variables constant. A similar expression holds for the electron electrochemical potential as

$$\eta^{\alpha}_{e^-} = \frac{\partial G^{\alpha}}{\partial N^{\alpha}_{e^-}} \quad (3)$$

The electrochemical potentials measure how the free energy of α changes as a charged species is added. The electrochemical potentials can be related to the more conventional *chemical* potentials for neutral species. For example, the Li chemical potential of the phase α is defined as the change in free energy upon addition of neutral Li atoms according to

$$\mu^{\alpha}_{Li} = \frac{\partial G^{\alpha}}{\partial N^{\alpha}_{Li}} = \frac{\partial G^{\alpha}}{\partial N^{\alpha}_{Li^+}}\frac{\partial N^{\alpha}_{Li^+}}{\partial N^{\alpha}_{Li}} + \frac{\partial G^{\alpha}}{\partial N^{\alpha}_{e^-}}\frac{\partial N^{\alpha}_{e^-}}{\partial N^{\alpha}_{Li}} = \eta^{\alpha}_{Li^+} + \eta^{\alpha}_{e^-} \quad (4)$$

where the chain rule of differentiation along with the constraint that $dN^{\alpha}_{Li} = dN^{\alpha}_{Li^+} = dN^{\alpha}_{e^-}$ has been used to express μ^{α}_{Li} in terms of the Li^+ and electron electrochemical potentials $\eta^{\alpha}_{Li^+}$ and $\eta^{\alpha}_{e^-}$.

For a battery in open circuit, the equilibrium state occurs when the total free energy (eq 1) is minimized with respect to redistributions of Li^+ between the electrodes and electrolyte. Because the total number of Li ions in the battery $N_{Li} = N^{C}_{Li^+} + N^{A}_{Li^+} + N^{E}_{Li^+}$ is constant, there are therefore only two independent variables, which, without loss of generality, we have chosen to be $N^{C}_{Li^+}$ and $N^{E}_{Li^+}$. Setting partial derivatives of G with respect to $N^{C}_{Li^+}$ and $N^{E}_{Li^+}$ equal to zero yields the following equilibrium criteria

$$\left(\frac{\partial G}{\partial N^{C}_{Li^+}}\right)_{N^{E}_{Li^+}} = \frac{\partial G^{C}}{\partial N^{C}_{Li^+}} + \frac{\partial G^{A}}{\partial N^{A}_{Li^+}}\left(\frac{\partial N^{A}_{Li^+}}{\partial N^{C}_{Li^+}}\right) = \eta^{C}_{Li^+} - \eta^{A}_{Li^+} = 0 \quad (5)$$

$$\left(\frac{\partial G}{\partial N^{E}_{Li^+}}\right)_{N^{C}_{Li^+}} = \frac{\partial G^{E}}{\partial N^{E}_{Li^+}} + \frac{\partial G^{A}}{\partial N^{A}_{Li^+}}\left(\frac{\partial N^{A}_{Li^+}}{\partial N^{E}_{Li^+}}\right) = \eta^{E}_{Li^+} - \eta^{A}_{Li^+} = 0 \quad (6)$$

Taken together, these relations state that the Li^+ electrochemical potential must be uniform throughout a battery in open circuit at equilibrium, i.e., $\eta^{C}_{Li^+} = \eta^{E}_{Li^+} = \eta^{A}_{Li^+}$.

The above equilibrium criteria allow us to derive the Nernst equation, which relates the OCV to intrinsic thermodynamic properties of the electrodes. The voltage, V, of the battery, as measured with a voltmeter inserted between the anode and the cathode in open circuit, is determined by the difference in electron electrochemical potentials of the cathode, $\eta^{C}_{e^-}$, and anode, $\eta^{A}_{e^-}$, according to

$$V = -\frac{\eta^{c}_{e^-} - \eta^{a}_{e^-}}{e} = -\frac{\mu^{C}_{Li} - \mu^{A}_{Li}}{e} \quad (7)$$

where e is the charge of an electron. The second equality emerges when invoking eq 4 to express $\eta^{\alpha}_{e^-} = \mu^{\alpha}_{Li} - \eta^{\alpha}_{Li^+}$ and then using the equilibrium criterion (eq 5) to cancel out the Li electrochemical potentials. This shows that the equilibrium voltage of a LIB is equal to a difference in Li chemical potentials between the anode and the cathode. A general expression for the Nernst equation when shuttling A^{z+} cations between anode and cathode takes the form

$$V = -\frac{\mu^{C}_{A} - \mu^{A}_{A}}{ze} \quad (8)$$

where z represents the oxidation state of the specie A (e.g., $z = 2$ for a Mg-ion battery).

2.1.2. Relationship between Voltage Profiles and Free Energies. A consequence of the Nernst relationship (eq 7) is

https://dx.doi.org/10.1021/acs.chemrev.9b00601
Chem. Rev. 2020, 120, 6977−7019

that a measurement of the voltage of the battery reveals a wealth of information about the intrinsic thermodynamic properties of the electrodes at different states of charge. When metallic Li is used as a reference anode, μ_{Li}^{A} is a constant (i.e., $\mu_{Li}^{A} = \mu_{Li}^{o}$, the chemical potential of pure Li, which only depends on temperature and pressure), and the measured voltage profile is then directly proportional to the Li chemical potential of the cathode, μ_{Li}^{C}. Chemical potentials can be derived from the Gibbs free energies of the individual active electrode materials according to eq 4. The shape of the voltage profile as a function of the shuttled Li is therefore determined by the concentration dependence of the Gibbs free energy of the electrodes.

The Li chemical potential has a convenient graphical representation in free energy versus concentration diagrams. The form of the graphical representation depends on the type of electrode, how the concentrations are defined and how the free energies are normalized:

- **Intercalation electrode**: The Li concentration of an intercalation compound x is defined as the ratio of Li atoms to available interstitial sites, which is proportional to the number of host formula units. For example, the number of available octahedral sites in layered Li_xCoO_2 is equal to the number of CoO_2 units, N_{CoO_2}, such that $x = N_{Li}/N_{CoO_2}$ where N_{Li} represents the number of Li in the crystal. Likewise, the free energy is conventionally normalized by the number of host units, e.g., $g = G/N_{CoO_2}$ for Li_xCoO_2. The chemical potential in a g versus x plot is then simply the slope of the free energy as illustrated in Figure 2a.
- **Alloy electrode**: For an alloy reaction, the concentration x refers to the relative fraction of Li. For example, when Li reacts with a Si anode to form Li_xSi_{1-x}, $x = N_{Li}/(N_{Li} + N_{Si})$ and the free energy is more appropriately normalized by the total number of atoms, i.e., $g = G/(N_{Li} + N_{Si})$. The Li chemical potential is then the intercept of the tangent to g with the $x = 1$ axis as illustrated in Figure 2b.
- **Conversion electrode**: For displacement and conversion reactions that result in a redistribution of other species, the free energy needs to be represented in higher dimensional composition spaces. Consider an electrode reaction that couples the insertion of Li with the simultaneous extrusion of a transition metal M from the starting compound M_yA_{1-x-y} as follows

$$x\mathrm{Li} + \mathrm{M}_y\mathrm{A}_{1-x-y} \rightarrow y\mathrm{M} + \mathrm{Li}_x\mathrm{A}_{1-x-y} \quad (9)$$

This reaction must be represented in a ternary composition space as illustrated in Figure 2c. The voltage is still related to the Li chemical potential according to eq 7, which in a ternary free energy diagram corresponds to the intersection of a tangent plane to the free energy g with the $x = 1$ axis, where g is defined as the free energy per atom (i.e., $g = G/(N_{Li} + N_M + N_A)$).

The voltage curves of intercalation and alloying reactions often exhibit a variety of sloping regions, steps and plateaus that reflect the existence of solid solutions, compounds and first-order phase transformations. Figure 3 schematically shows the relationship between voltage profiles and free energies for olivine Li_xFePO_4,[20] layered Li_xCoO_2[21−23] and spinel $Li_xMn_2O_4$,[24,25] the three canonical intercalation cathodes of the past three decades. While the chemistry of an electrode material undoubtedly plays a role in determining voltages, many

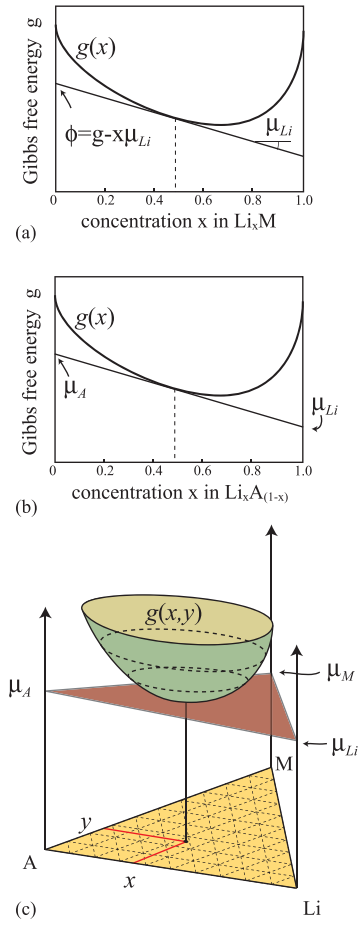

Figure 2. Graphical relationship between the Li chemical potential μ_{Li} and the concentration-dependent free energy g for (a) an intercalation electrode, (b) an alloy electrode, and (c) a conversion electrode.

qualitative features of a voltage profile can be traced to the crystal structure of the host compound.

Li_xFePO_4 (Figure 4a) hosts Li over an interstitial network that has one-dimensional connectivity. The voltage profile of Li_xFePO_4 is dominated by a plateau due to a large miscibility gap between a Li-lean α-Li_xFePO_4 and a Li-rich β-Li_xFePO_4. The plateau emerges because the Li chemical potential remains constant inside the two-phase coexistence region as a result of the common tangent construction.

Li_xCoO_2 (Figure 4b) is a layered compound that accommodates Li ions within octahedral sites that form two-dimensional triangular lattices. Li_xCoO_2 has a richer voltage profile that is characteristic of many other layered intercalation compounds, exhibiting multiple small plateaus, sloping regions, and steps.[17] $LiCoO_2$ starts out in the O3 crystal structure, using the notation of Delmas.[26] It undergoes a two-phase reaction upon Li removal, resulting in a plateau between $Li_{0.93}CoO_2$ and $Li_{0.75}CoO_2$.[21] This two-phase reaction masks an intriguing insulator to metal electronic transition that remains to be understood. Further removal of Li from Li_xCoO_2 occurs through a solid solution, characterized by Li vacancy disorder within the Li layers. At $x = {}^1/_2$, the Li ions and vacancies order within each Li layer, which manifests itself as a small step in the voltage profile.[21] At dilute Li concentrations, the O3 host structure undergoes structural transformations to the H1-3 and O1 crystal structures as a result of stacking sequence changes between CoO_2 slabs across emptied Li layers.[23,27,28] These transitions

https://dx.doi.org/10.1021/acs.chemrev.9b00601
Chem. Rev. 2020, 120, 6977−7019

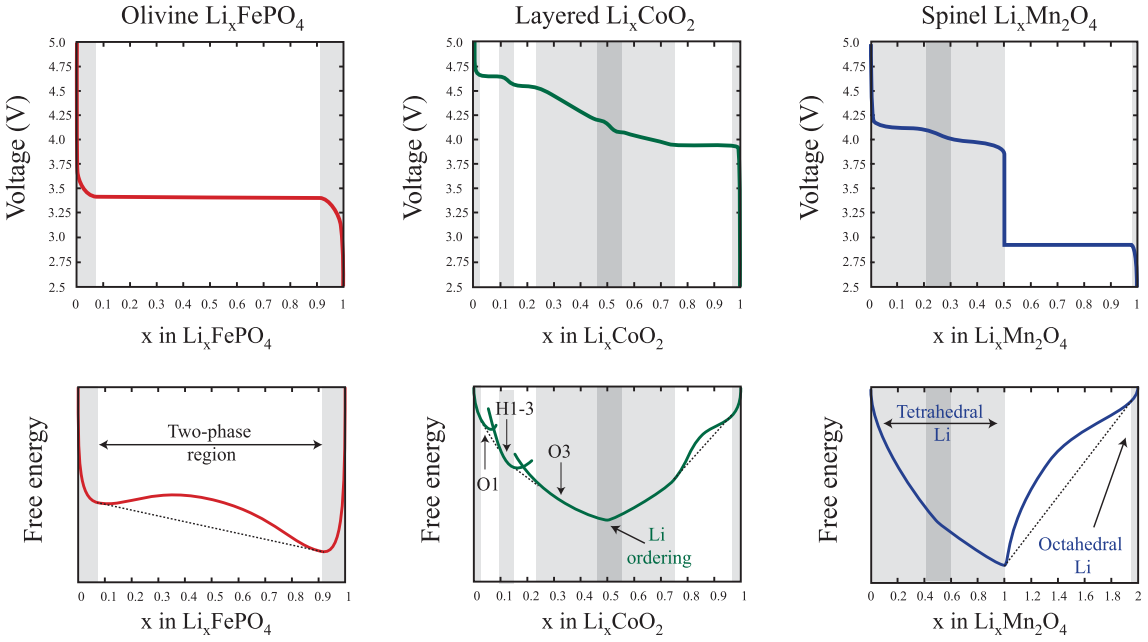

Figure 3. Schematic illustration of the voltage curves of Li_xFePO_4, Li_xCoO_2, and $Li_xMn_2O_4$ and their relationship to the Gibbs free energies of each compound. The dashed lines in the free energy plots represent common tangents, which coincide with plateaus in the voltage profiles. The gray regions denote single phase regions (light gray are solid solutions, and dark gray correspond to ordered phases).

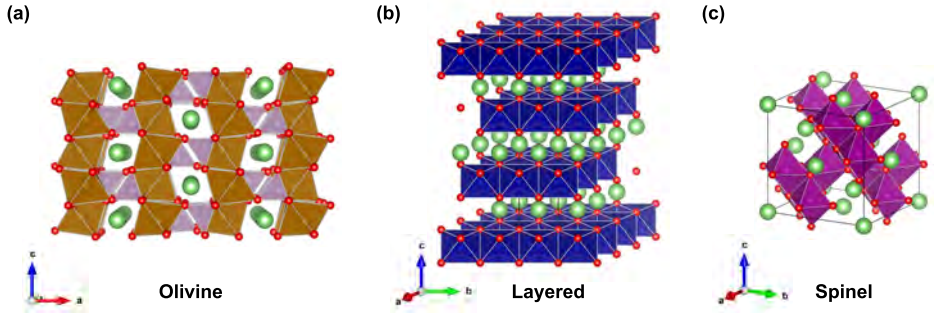

Figure 4. Crystal structures of (a) $LiFePO_4$, (b) $LiCoO_2$, and (c) $LiMn_2O_4$. Green atoms are lithium and red atoms are oxygen. Yellow octahedra and gray tetrahedra in (a) are FeO_6 and PO_4, respectively. Blue octahedra in (b) are CoO_6. Magenta octahedra in (c) are MnO_6.

appear as plateaus separated by small steps as illustrated in the voltage profile of Li_xCoO_2 in Figure 3.

The spinel form of $Li_xMn_2O_4$ (Figure 4c) has both tetrahedrally and octahedrally coordinated Li interstitial sites that form a three-dimensional network.[25] The availability of two types of interstitial sites in $Li_xMn_2O_4$ is responsible for the large step in the voltage profile. While Li prefers the tetrahedral sites of spinel oxides, the host crystal has twice as many octahedral sites. Li initially fills the tetrahedral sites at around 4 V until all tetrahedral sites are filled at $x = 1$. Further Li insertion can only be accommodated by the octahedral sites. However, octahedral sites reside between pairs of tetrahedral sites, preventing the simultaneous occupancy of nearest neighbor tetrahedral and octahedral sites. The further insertion of Li, therefore, proceeds according to a two-phase reaction, resulting in a wide plateau in the voltage curve between $LiMn_2O_4$ and $Li_2Mn_2O_4$.

The interpretation of features in the voltage profile becomes more ambiguous when other ions redistribute upon Li insertion or removal, as occurs during displacement and conversion reactions. If the composition changes of the electrode occur in a ternary composition space during Li insertion, for example, both a solid solution within a single phase as well as a two-phase reaction result in sloping voltage profiles. Only during a three-phase reaction will the voltage exhibit a plateau because the common tangent plane to the free energies of the three coexisting phases, which determines the Li chemical potential, remains constant. This is schematically illustrated for the $Li + Cu_{0.5}TiS_2 \rightarrow \frac{1}{2}Cu + LiTiS_2$ displacement reaction in Figure 5.[29] The insertion of Li into the spinel form of $Cu_{0.5}TiS_2$ is accompanied by the simultaneous displacement of Cu, resulting in a three phase microstructure consisting of $Cu_{0.5}TiS_2$, $LiTiS_2$, and metallic Cu. The electrochemical insertion of Li simply changes the relative phase fractions of each phase, without altering the compositions of the individual phases. The common tangent plane (gray plane in Figure 5), therefore, remains fixed as the Li concentration of the electrode is varied, resulting in a constant voltage and hence a plateau in the voltage profile.

2.1.3. Electrochemical, Chemical, and Electrostatic Potentials. It is common to separate the electrochemical potentials of charged species such as Li^+ and electrons into a chemical term and an electrostatic part according to[30,31]

$$\eta_{Li^+} = \mu_{Li^+} + e\phi \tag{10}$$

https://dx.doi.org/10.1021/acs.chemrev.9b00601
Chem. Rev. 2020, 120, 6977−7019

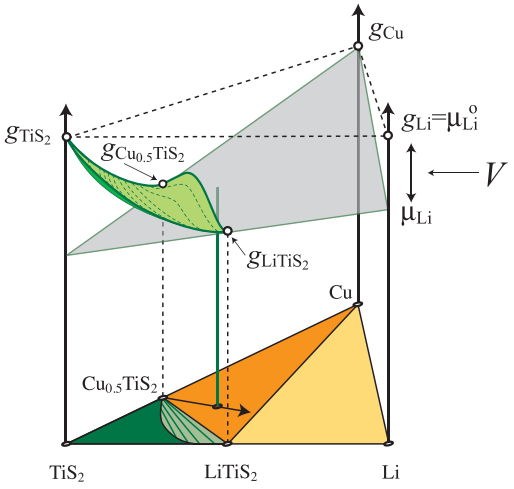

Figure 5. Schematic illustration of the common tangent plane to the free energy for a three-phase coexistence during a displacement reaction. This example shows a schematic free energy for the $Li + Cu_{0.5}TiS_2 \rightarrow \frac{1}{2}Cu + LiTiS_2$ displacement reaction, which occurs along the arrow in the orange three phase triangle. Adapted from ref 29. Copyright 2014 the Royal Society of Chemistry.

$$\eta_{e^-} = \mu_{e^-} - e\phi \tag{11}$$

where ϕ refers to a local electrostatic potential.

The electrostatic potential is conventionally referenced to zero when the solid is electrically neutral. There is ambiguity, however, as to how to separate the electrochemical potential into a chemical and electrostatic component, and it is only when making comparisons between regions having the same chemical composition that variations in ϕ can be made to strictly coincide with classical notions of an electrostatic potential. For a detailed discussion of these subtleties, we refer the reader to the text book of Newman.[30]

The electron electrochemical potential, η_{e^-}, is known as the Fermi level. The Fermi level corresponds to the electron energy at which the Fermi−Dirac distribution has a value of 0.5 in solids whose electronic structure can be approximated by single-particle energy bands. The Fermi level of typical metals have a negligible temperature dependence and can therefore be approximated by the highest energy of the occupied states of the conduction band at zero Kelvin. In semiconductors and insulators, the Fermi level usually resides within the band gap separating valence and conduction bands. As is evident from eq 10, η_{e^-} becomes equal to the electron chemical potential μ_{e^-} when the electrostatic potential ϕ is equal to zero. The chemical potential, μ_{e^-}, is generally assumed to be independent of the electrostatic ϕ.

The chemical potential of Li^+ of a solid, μ_{Li^+}, appearing in eq 10, can be related to the Li chemical potential, μ_{Li}, and the electron chemical potential, μ_{e^-}, by combining eqs 4, 10, and 11 according to

$$\mu_{Li^+} = \mu_{Li} - \mu_{e^-} \tag{12}$$

The Li chemical potential μ_{Li}, which is equal to the change in free energy of the solid upon the insertion of a neutral Li atom, is generally assumed to be independent of the electrostatic potential of the solid.

The expression of the electrochemical potential of an ion A^z with oxidation state, z, is

$$\eta_{A^z} = \mu_{A^z} + ze\phi \tag{13}$$

where similar expressions for the chemical potential term μ_{A^z} hold as for μ_{Li^+}. While eqs 10 and 11, and eq 13 more generally, are convenient to work with when solving for the dynamic response of a battery, they are not necessary in a formal phenomenological description of a battery as the fundamental quantities that drive kinetic processes are imbalances in electrochemical potentials.

2.1.4. Equilibrium across Electrode/Electrolyte Interfaces. An electrostatic potential difference emerges across an electrode/electrolyte interface as a result of a redistribution of Li^+ between the two phases that are driven by chemical imbalances. For example, Li may have a lower chemical potential in the electrolyte than in the electrode and will experience a driving force to migrate from the electrode to the electrolyte when they are put in contact with each other. An example is shown in the inset in Figure 1. Because the electrolyte is an insulating phase, any Li that migrates from the electrode to the electrolyte must leave behind an electron, thereby producing a charge imbalance between the electrode and electrolyte. Most electrodes have a high electronic conductivity, while good electrolytes have a high Li^+ conductivity. Hence, excess negative charge will segregate to the electrode side of the electrode/electrolyte interface, while the excess positive charge in the electrolyte will segregate to the electrolyte side of the electrode/electrolyte interface. Most of the potential drop between the electrode and electrolyte is therefore concentrated across the interface, resulting in large electric fields in a thin region along the interface. At some point, the resulting electric field becomes large enough to counter the chemical driving forces and the transfer of Li^+ ceases, resulting in a local equilibrium across the interface.

According to eq 6, equilibrium across the electrode/electrolyte interface will set in when the Li^+ electrochemical potentials are equal in the two phases, i.e., $\eta^A_{Li^+} = \eta^E_{Li^+}$. By setting $\eta^A_{Li^+} = \mu^A_{Li} - \eta^A_{e^-}$ (using eq 4) equal to $\eta^E_{Li^+} = \mu^E_{Li^+} + e\phi^E$, it is possible (together with eq 11) to relate the electrostatic potential drop across the interface to differences in chemical potentials according to

$$-e\Delta\phi = \mu^{\,A}_{Li} - \mu^{\,E}_{Li^+} - \mu^{\,A}_{e^-} \tag{14}$$

where $\Delta\phi = \phi^A - \phi^E$ is the change in electrostatic potential when passing from the interior of the anode to the interior of the electrolyte. The larger the chemical imbalances, as manifested by the differences in the chemical potentials on the right-hand side of eq 14, the larger the change in electrostatic potential across the interface. A similar expression holds at the cathode/electrolyte interface.

The equilibrium criterion across the electrode/electrolyte interface as given by eq 14 is general and does not assume that the electrode or electrolyte are dilute. The chemical potentials that appear in the interface equilibrium criterion depend on the local concentration as well as other thermodynamic boundary conditions, such as temperature and pressure. The Li chemical potential of an intercalation compound, for example, is a function of the local Li concentration. Similarly, and in contrast to metallic electrodes such as platinum or pure lithium, the electron chemical potential, μ_{e^-}, of an intercalation compound will also depend on the band filling of the solid, which in turn depends on the local Li concentration within the electrode. This is because the position of the Fermi level of an intercalation compound is a function of its Li concentration. When

https://dx.doi.org/10.1021/acs.chemrev.9b00601
Chem. Rev. 2020, 120, 6977−7019

anisotropic stress states are present (e.g., due to coherency between an electrode and a solid electrolyte), it is necessary to derive chemical potentials from a Helmholtz free energy (as opposed to a Gibbs free energy) that is a function of composition, temperature, and *strain* to ensure that the chemical potentials also depend on the local strain state.[32,33]

The detailed variation of the electrostatic potential and atomic structure across electrode/electrolyte interfaces of alkali-ion batteries is complex and remains poorly characterized and understood.[13,34] This structure, however, undoubtedly plays an important role in determining the kinetics of the electrochemical reactions that occur at the interface. For simple, unpassivated metallic electrodes, it is well established that a diffuse double layer emerges within a liquid electrolyte at the electrode/electrolyte interface. The diffuse layer contains charge that compensates the excess charge on the surface of the electronically conducting electrode. For example, when the surface of the electrode is negatively charged, positively charged cations within the electrolyte will segregate toward the electrode surface. The excess concentration of the segregated cations tends to be spread over a finite width that is typically on the order of several nanometers. The diffuseness of the interface region arises from thermal agitation, the tendency of cations to be surrounded by a solvation shell in the electrolyte, and the complex structure of electrolyte solvent molecules.[30,31]

The polarization behavior of an electrode/electrolyte interface in the absence of electrochemical reactions is similar to that of a pair of capacitor plates. A variety of models of increasing sophistication have been formulated for the molecular structure of diffuse double layers based on the pioneering work of Helmholtz, Gouy, and Chapman and Stern. Detailed descriptions of these interface models can be found in the classic textbooks of Newman[30] and Bard and Faulkner.[31] The textbook models of electrode/electrolyte interface structures, however, have been developed for highly idealized systems such as the mercury electrode. The structure of electrode/electrolyte interfaces in Li-ion batteries is more complex.[13,34] One complicating factor is the formation of interphase layers that arise from decomposition reactions when an electrode and the components of the electrolyte chemically react upon contact. An example is the solid electrolyte interface (SEI) that forms at the anode/electrolyte interface of most Li-ion batteries. The phases, their composition and crystal structure, and the nanostructure of the SEI that forms on graphite anodes, for example, remains poorly understood and challenging to characterize experimentally.[34] This poses challenges when developing theoretical models that describe the thermodynamics of electrode/electrolyte interfaces in alkali-ion batteries.[35,36] The electrode/electrolyte interfaces of all solid-state batteries are more amenable to experimental characterization. A notable difference between solid electrolytes and liquid electrolytes is that the counteranions are fixed within the crystal resulting in a space charge region within the solid electrolyte.[36−38]

2.2. Kinetics of Elementary Processes

2.2.1. Electrode/Electrolyte Interface Kinetics. The electrochemical reaction at the electrolyte/electrode interface is an essential kinetic process that must occur during charging and discharging of a battery. As a concrete example, consider the electrochemical reaction across the anode/electrolyte interface. The driving force for this reaction is an imbalance between the Li^+ electrochemical potentials across the interface. This occurs when

$$\Delta\eta_{Li^+} = \eta^{A}_{Li^+} - \eta^{E}_{Li^+} \tag{15}$$

referred to as an overpotential, deviates from zero. The electrochemical potentials, $\eta^{A}_{Li^+}$ and $\eta^{E}_{Li^+}$, appearing in eq 15, are the local electrochemical potentials of the anode and electrolyte immediately adjacent to the anode/electrolyte interface. According to eq 6, $\Delta\eta_{Li^+}$ is equal to zero in equilibrium. An interface reaction will occur, however, when $\Delta\eta_{Li^+}$ deviates from zero in order to restore local equilibrium at the interface. If $\Delta\eta_{Li^+}$ is negative, Li^+ ions will flow from the electrolyte into the anode, while the reverse occurs when $\Delta\eta_{Li^+}$ is positive. The value of $\Delta\eta_{Li^+}$ depends on the Li and electron concentrations at the interface and any other thermodynamic boundary conditions such as temperature and local stresses (or strains).

The net Li^+ flux, J_{Li^+}, across the interface (from the electrode to the electrolyte), will be a function of $\Delta\eta_{Li^+}$[17]

$$J_{Li^+} = f(\Delta\eta_{Li^+}) \tag{16}$$

The function f must be equal to zero in the absence of a driving force to ensure that thermodynamic equilibrium criteria are satisfied in the absence of a driving force across the interface. A commonly used response function is the Butler−Volmer equation[30,31]

$$J_{Li^+} = J^{0}_{Li^+}\left\{\exp\left(\frac{\alpha\Delta\eta_{Li^+}}{k_B T}\right) - \exp\left(-\frac{(1-\alpha)\Delta\eta_{Li^+}}{k_B T}\right)\right\} \tag{17}$$

where k_B is Boltzmann's constant, T is the temperature, $J^{0}_{Li^+}$ is the exchange flux, and α is a symmetry factor that takes a value between 0 and 1. Both the exchange current and symmetry factor are often treated as empirical parameters to be fit to experimental data.

For small overpotentials, $\Delta\eta_{Li^+}$, the above equation can be linearized as

$$J_{Li^+} \approx J^{0}_{Li^+}\frac{\Delta\eta_{Li^+}}{k_B T} \tag{18}$$

If interface kinetics is very fast compared to other kinetics in the adjacent electrode and electrolyte, $\Delta\eta_{Li^+}$ will be close to zero. In this regime, the local equilibrium approximation becomes valid and the Li concentration at the interface is then determined by the thermodynamic condition that $\eta^{A}_{Li^+} = \eta^{E}_{Li^+}$.

The Butler−Volmer expression, eq 17, can be put in a form that is more commonly used in the electrochemistry literature[30] by expressing the overpotential $\Delta\eta_{Li^+}$ in terms of the difference in electrostatic potential upon crossing the interface, $\Delta\phi = \phi^{A} - \phi^{E}$, according to[17]

$$\Delta\eta_{Li^+} = e(\Delta\phi - \Delta\phi^{\circ}) \tag{19}$$

provided that $-e\Delta\phi^{\circ}$ is defined to be equal to $\mu^{A}_{Li} - \mu^{E}_{Li^+} - \mu^{A}_{e^-}$. This relation follows by inserting eqs 4, 10, and 11 into eq 15.

Alternatives to the Butler−Volmer interface response function have been formulated based on Marcus theory.[39−41] Because of the absence of accurate structural models at the atomic scale of electrode/electrolyte interfaces in Li-ion batteries, most interface response functions formulated to date remain phenomenological and are expressed in terms of empirical parameters to be fit to experimental measurements.

2.2.2. Ion Transport in Electrodes. Ion transport within the electrodes and electrolyte plays a crucial role in the kinetic response of a battery. At a phenomenological level, transport is described with flux expressions that relate ion fluxes to gradients

https://dx.doi.org/10.1021/acs.chemrev.9b00601
Chem. Rev. 2020, 120, 6977−7019

in chemical or electrochemical potentials. In an intercalation compound that is metallic, a Li flux emerges in the presence of a gradient in the Li chemical potential according to[42]

$$J_{\mathrm{Li}} = -L\nabla\mu_{\mathrm{Li}} \tag{20}$$

where the Onsager transport coefficient, L, is a measure of the Li mobility within the crystal structure of the intercalation compound. While the kinetic coefficient L describes a nonequilibrium process, it can be related to fluctuations that occur at equilibrium due to the fluctuation−dissipation theorem of statistical mechanics.[43−45] Even in equilibrium, Li ions migrate throughout the crystal as a result of stochastic hops between neighboring Li sites. After a time t, each Li ion, i, will have migrated by a vector $\Delta\vec{R}_i$, which connects the end points of its trajectory as illustrated in Figure 6a.

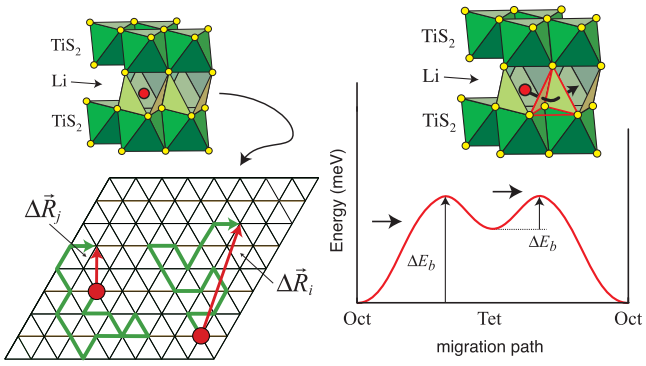

(a) Li hops in layered $LiTiS_2$ (b) Migration barriers

Figure 6. Li migration in the prototypical $LiTiS_2$ intercalation cathode. (a) Li ions perform stochastic hops between neighboring sites, even in equilibrium, and wander throughout the crystal. The end points of their trajectories, $\Delta\vec{R}_i$, appear in the statistical mechanics expressions for the macroscopic transport coefficients. In this illustration, Li ions wander over the octahedral sites of a layered intercalation compound, which form two-dimensional triangular lattices. (b) Migration barriers ΔE_b appearing in the transition state theory hop frequency expression correspond to the energy barrier along the minimal energy path between local minima. Li hops between the octahedral sites of common layered intercalation compounds proceed through an intermediate tetrahedral site, which usually corresponds to a local minimum on the minimal energy surface.

For interstitial diffusion within an intercalation host, the Onsager transport coefficient can be expressed as an ensemble average of the square of the sum of all the Li trajectory vectors according to[45]

$$L = \frac{1}{\Omega k_{\mathrm{B}}T}\frac{\left\langle \left(\sum_i \Delta\vec{R}_i\right)^2 \right\rangle}{2dMt} \tag{21}$$

where Ω is the volume per Li interstitial site and M is the number of interstitial sites of the solid. For Li_xCoO_2, for example, $M = N_{CoO_2}$ and Ω is the volume per Li_xCoO_2 unit. The angular brackets in eq 21 denote a statistical mechanical ensemble average at equilibrium. eq 21 assumes a sufficiently high symmetry of the interstitial sublattice such that L has the same value in all directions, with d referring to the dimensionality of the interstitial sublattice (e.g., $d = 1$ for Li_xFePO_4, $d = 2$ for Li_xCoO_2, and $d = 3$ for spinel $Li_xMn_2O_4$). In crystals that have low symmetry, L becomes a rank two tensor.[45,46]

eq 21 in essence measures the mean square of the displacement of the center of mass of the collection of diffusing Li ions; the more that the center of mass of a collection of Li ions in a host wanders at equilibrium, the more mobile it will be when a driving force such as a chemical potential gradient is applied.

The trajectories of each Li ion in a typical intercalation compound arises from the succession of elementary Li-vacancy exchanges, which can be treated as rare stochastic events that occur after the hopping Li ion has undergone a large number of vibrational excitations. Transition state theory provides an estimate for the frequency of such rare events according to[47]

$$\Gamma = \nu^* e^{-\Delta E_b/k_{\mathrm{B}}T} \tag{22}$$

where ν^* is the vibrational prefactor having units of seconds^{-1} and ΔE_b is an energy barrier that the migrating Li ion must overcome as it hops from one site to a vacant neighboring site. The vibrational prefactor measures the change in vibrational entropy as an atom migrates from an initial equilibrium site through an activated state. ΔE_b corresponds to the energy barrier along the minimum energy pathway connecting the end states of the hop, whereby all other ions of the crystal are allowed to fully relax.[47] A minimal energy pathway is schematically illustrated in Figure 6b, which shows a Li ion in a layered intercalation compound migrating between nearest neighbor octahedral sites by passing through an intermediate tetrahedral site. In the particular example of Figure 6b, the intermediate tetrahedral site corresponds to a local minimum in the energy landscape and is a site in which Li will thermalize before continuing on to an adjacent octahedral site.[48]

The phenomenological flux expression, eq 20, can be converted to Fick's first law using the chain rule of differentiation

$$J_{\mathrm{Li}} = -D\nabla C \tag{23}$$

where the composition C is defined as the number of Li ions per unit volume. For a homogeneous solid, $C = N/(M\Omega) = x/\Omega$, where N refers to the number of Li ions and $x = N/M$ is the number of filled Li sites. In a solid with concentration gradients, C will be a function of position $\vec{r}$. For an intercalation compound, the diffusion coefficient D is related to L according to

$$D = L\Omega\left(\frac{\partial\mu_{\mathrm{Li}}}{\partial x}\right) = L\Omega\left(\frac{\partial^2 g}{\partial x^2}\right) \tag{24}$$

where g is the free energy of the compound normalized by the number of interstitial sites M. In describing Li diffusion in intercalation compounds, it is common to factor the chemical diffusion coefficient, D, in terms of a "jump" diffusion coefficient and a thermodynamic factor, Θ, according to $D = D_J\Theta$,[49] where

$$D_J = \frac{\Omega k_{\mathrm{B}}T}{x}L = \frac{\left\langle \left(\sum_i \Delta\vec{R}_i\right)^2 \right\rangle}{2dNt} \tag{25}$$

and

$$\Theta = \frac{\partial\left(\frac{\mu_{\mathrm{Li}}}{k_{\mathrm{B}}T}\right)}{\partial \ln x} \tag{26}$$

It is straightforward to verify that the product of D_J and Θ is equivalent to eq 24. This factorization is especially convenient because the thermodynamic factor, Θ, is a measure of the deviation from thermodynamic ideality of the intercalation host. Θ reduces to 1 at dilute Li concentrations, where interactions among Li can be neglected and the Li chemical potential can be

https://dx.doi.org/10.1021/acs.chemrev.9b00601
Chem. Rev. 2020, 120, 6977−7019

approximated with the ideal solution form of $\mu = \mu^o + k_B T \ln x$. At nondilute Li concentrations, Li−Li interactions become important, and the thermodynamic factor Θ deviates from 1. Θ can attain very high values at compositions where the Li ions order because ordered phases have thermodynamic properties that deviate strongly from that of an ideal solid solution.[50,51]

By expanding the square of the sum of ionic displacement vectors in eq 25, the jump diffusion coefficient D_J can be written as

$$D_J = \frac{\sum_i \langle \Delta \vec{R}_i^{\,2} \rangle}{2dNt} + \frac{\sum_i \sum_{j \neq i} \langle \Delta \vec{R}_i \Delta \vec{R}_j \rangle}{2dNt} \tag{27}$$

where the first term corresponds to the tracer diffusion coefficient, D^*, defined as

$$D^* = \frac{\sum_i \langle \Delta \vec{R}_i^{\,2} \rangle}{2dNt} \tag{28}$$

The second term in eq 27 measures correlations between the trajectories of different Li-ions. This term is generally positive such that D_J is greater than the tracer diffusion coefficient. The ratio between D^* and D_J is referred to as the Haven ratio, H_R,[52] and in view of the above relation can be expressed as

$$\frac{1}{H_R} = \frac{D_J}{D^*} = 1 + \frac{\sum_i \sum_{j \neq i} \langle \Delta \vec{R}_i \Delta \vec{R}_j \rangle}{\sum_i \langle \Delta \vec{R}_i^{\,2} \rangle} \tag{29}$$

The Haven ratio is a measure of the degree with which the trajectories of different atoms are correlated to each other. It becomes equal to one in the absence of any correlations between different diffusing atoms. This is asymptotically approached in the dilute limit, where diffusing atoms rarely encounter each other while they migrate through the crystal. At nondilute concentrations (for example, in most solid electrolytes), correlations between different diffusing ions become important and generally result in a Haven ratio that is less than one.

The Haven ratio is not to be confused with the more commonly known correlation factor, f, which measures correlations between successive hops of the same atom and is defined as

$$f = \frac{\langle \Delta \vec{R}^2 \rangle}{n \Delta r^2} \tag{30}$$

where $\Delta \vec{R}$ connects the end points of the trajectory of a particular diffusing atom after performing n hops and where Δr^2 is the square of an elementary hop distance. The correlation factor is equal to 1 for a random walk where successive hops of an individual atom are completely uncorrelated. Diffusion that is correlated leads to a correlation factor that is less than 1 and is less efficient than that of a purely random walk.

While kinetic Monte Carlo or molecular dynamics simulations are generally necessary to calculate the various metrics of diffusion described above, there are simple analytical expressions for D_J, Θ, and hence D for intercalation compounds that are both thermodynamically and kinetically ideal. A thermodynamically ideal intercalation compound refers to one in which interactions among the Li-ions and vacancies can be neglected. Ideal solution theory predicts that the thermodynamic factor for a thermodynamically ideal intercalation compound that hosts Li in only one type of interstitial site reduces to $\Theta = 1/(1 - x)$, where x is the Li concentration (fraction of filled interstitial sites). A kinetically ideal intercalation compound refers to one in which every Li-ion hop has an identical hop frequency, Γ, independent of the local concentration and degree of ordering. For a kinetically ideal intercalation compound $D_J = (1-x)\rho\Delta r^2\Gamma$, where ρ is a geometric factor that depends on the connectivity of the Li-interstitial network and where Δr is the distance of each hop.[53] This leads to the remarkable result that the chemical diffusion coefficient, $D = D_J\Theta$, of a thermodynamically and kinetically ideal intercalation compound has no explicit concentration dependence, i.e., $D = \rho\Delta r^2\Gamma$ (there may be an implicit concentration dependence if Γ is a function of the average concentration). As the name implies, thermodynamically and kinetically ideal intercalation compounds do not exist in reality. However, the analytical expressions of their diffusion coefficients can be used to estimate diffusion coefficients for intercalation compounds at dilute concentrations (i.e., $x \approx 0$ or $x \approx 1$), where ideal solution theory is a good approximation and where all hop environments tend to be identical.

Not all electrodes are intercalation compounds. Promising anode chemistries, for example, rely on alloying reactions.[54,55] Ionic transport in an alloy is more complex than in an intercalation compound, as it involves fluxes of several species and usually occurs through substitutional exchanges mediated by dilute concentrations of vacancies. The phenomenological and statistical mechanical theory of substitutional diffusion in alloys is reviewed elsewhere.[56−58]

2.2.3. Coupled Ionic and Electronic Transport. The flux expressions, eqs 20 and 23, assume that the electronic conductivity within the electrode is not rate limiting. This is generally true in electrode materials that are metallic, where the electronic mobility is sufficiently high to screen any long-range electrostatic fields. While electrode materials with high electronic mobilities are preferred for practical battery applications, there are, nevertheless, several chemistries with sluggish electronic conductivities that have proven to be viable electrode materials in Li ion batteries. Olivine Li_xFePO_4 is one notable example.[59] When the electron mobility is similar to or less than that of the Li mobility, it becomes necessary to explicitly track the electron distribution throughout the solid as well the electric fields that emerge when local charge imbalances occur. The fluxes of Li^+ and e^- are then driven by gradients in the Li^+ and e^- *electrochemical* potentials according to

$$J_{Li^+} = -L_{Li^+,Li^+}\nabla\eta_{Li^+} - L_{Li^+,e^-}\nabla\eta_{e^-} \tag{31}$$

$$J_{e^-} = -L_{e^-,Li^+}\nabla\eta_{Li^+} - L_{e^-,e^-}\nabla\eta_{e^-} \tag{32}$$

where the L's are again Onsager transport coefficients and now form a matrix. This matrix is symmetric when the Onsager reciprocity relations hold, i.e., $L_{Li^+,e^-} = L_{e^-,Li^+}$. Off-diagonal transport coefficients are generally much smaller than the diagonal coefficients[56] and are commonly neglected.

Transport of Li^+ ions and electrons in solids where both species have comparable mobility is highly coupled. For instance, if Li^+ ions get ahead of their charge compensating electrons, an electrostatic potential gradient, $\nabla\phi$, emerges that exerts a driving force to pull the lagging electrons along. The above flux expression for Li^+ and electrons can be converted into an effective flux expression for Li in circumstances where Li transport through the electrode does not result in a net accumulation of charge over macroscopic length scales, i.e., $J_{Li} = J_{Li^+} = J_{e^-}$ at each point of the solid. This constraint makes it possible to express the gradient of the electrostatic potential, $\nabla\phi$, in terms of the gradients of chemical potentials when using eq 10 and eq 11, together with eq 31 and eq 32. By then, using

https://dx.doi.org/10.1021/acs.chemrev.9b00601
Chem. Rev. 2020, 120, 6977−7019

the relationship, $\mu_{Li} = \mu_{Li^+} + \mu_{e^-}$, it is possible to rewrite the Li flux expression eq 31 according to

$$J_{Li} = -L\nabla\mu_{Li} \tag{33}$$

where

$$L = \frac{L_{Li^+,Li^+}L_{e^-,e^-} - L^2_{Li^+,e^-}}{L_{Li^+,Li^+} + L_{e^-,e^-} - 2L_{Li^+,e^-}} \tag{34}$$

The resultant Onsager transport coefficient, L, depends on both the Li^+ and electron transport coefficients as well as the coupling transport coefficient. If the electrode has a very high electron mobility such that $L_{e^-,e^-} \gg L_{Li^+,Li^+}$ and L_{Li^+,e^-}, the effective transport coefficient L reduces to L_{Li^+,Li^+} and depends only on the mobility of Li ions.

A situation where ions and electrons have comparable mobilities is in solids where electrons localize to form polaronic states. This can occur in crystal structures that have localized orbitals, e.g., the Fe d orbitals in $LiFePO_4$, to accommodate an electron or hole. This localized electron/hole then causes neighboring atoms to move from their equilibrium positions, and the resulting quasiparticle that contains the localized electron/hole with the lattice distortion is then referred to as a polaron. Polarons migrate through the crystal stochastically in a manner similar to ionic hops but with hop frequencies that are more appropriately modeled with Marcus theory.[60,61] The polaron and Li^+−polaron coupling Onsager coefficients can also be calculated with Kubo−Green expressions similar to eq 21.[45,46]

2.2.4. Ion Transport in Electronically Insulating Phases. In the previous two sections, we considered Li transport through solid electrode phases that are metallic or have comparable electron/ion mobility. The other extreme occurs in solids that are electronically insulating, a notable example being superionic conductor solid electrolytes. Many solid electrolytes do not contain a redox-active element, and hence, cannot form localized polaronic states. Further, due to the lack of electron mobility, macroscopic Li concentration gradients cannot form in solid electrolyte materials. The Onsager transport coefficients L_{e^-,Li^+} and L_{e^-,e^-} in the flux expression eq 32, which relates the electron flux, J_e, to the electrochemical potential gradients, $\nabla\eta_{Li^+}$ and $\nabla\eta_{e^-}$, are then very small and negligible, especially compared to L_{Li^+,Li^+}. Furthermore, when the Onsager reciprocity relation holds, $L_{e^-,Li^+} = L_{Li^+,e^-}$, it is possible to neglect the effect of $\nabla\eta_{e^-}$ on J_{Li^+}, such that the Li flux expression, eq 31, reduces to

$$J_{Li^+} = -L_{Li^+,Li^+}\nabla\eta_{Li^+} = -L_{Li^+,Li^+}(\nabla\mu_{Li^+} + e\nabla\phi) \tag{35}$$

where we have used eq 10 to express the electrochemical potential of Li^+ in terms of its chemical potential and the electrostatic potential ϕ. As before, L_{Li^+,Li^+} can be related to fluctuations that occur at equilibrium using the Kubo−Green expression of eq 21.

In the study of solid electrolytes, it is common to express ionic motion in terms of a charge flux, J_+, instead of an ion flux. The two are related according to $J_+ = eJ_{Li^+}$. As with an electrical current, the ion charge flux can be related to a gradient in the ion electrochemical potential, η_{Li^+}/e, by an ionic conductivity, σ, according to

$$J_+ = -\sigma\nabla(\eta_{Li^+}/e) \tag{36}$$

A comparison of this flux expression to eq 35 (using eqs 25 and 29) yields a useful relationship between the ionic conductivity, σ, and the tracer and jump diffusion coefficients

$$\sigma = e^2L_{Li^+,Li^+} = e^2C\frac{D_J}{k_BT} = \frac{e^2C}{H_R}\frac{D^*}{k_BT} \tag{37}$$

where $C = x/\Omega$ is the number of mobile Li ions per unit volume. The ionic conductivity, σ, is a quantity that is more readily measured experimentally, while the jump and tracer diffusion coefficients, D_J and D^*, are quantities that are more easily calculated with kinetic Monte Carlo or molecular dynamics simulations, as will be described in subsequent sections.

2.3. Phase Transformations in Electrodes

Many electrode materials become susceptible to phase transformations due to the large variation in their Li concentration during a charge and discharge cycle. It is possible to distinguish between different categories of phase transformations. Some are relatively facile, while many others involve dramatic crystallographic changes that can lead to degradation of the electrode particles over the course of several charge and discharge cycles. We review the phenomenological theories that exist to describe each type of phase transformation and point out areas where new phenomenological descriptions are necessary.

2.3.1. Topotactic Phase Transitions. The simplest solid-state phase transformations are two-phase reactions that preserve the host crystal structure upon Li insertion or removal. Examples of electrode chemistries that undergo such a phase transformation include spinel $Li_7Ti_5O_{12}$ and olivine $LiFePO_4$. Spinel $Li_7Ti_5O_{12}$ transforms to $Li_4Ti_5O_{12}$ during Li extraction without undergoing any crystallographic change to the spinel host.[62] Furthermore, it has the unique property that its lattice parameters change negligibly during the two-phase reaction in spite of the large change in Li concentration. The kinetics of this two-phase reaction can be described with the Cahn−Hilliard theory of spinodal decomposition.[63−65] As Li is removed from $Li_7Ti_5O_{12}$ particles, a two-phase coexistence emerges between $Li_7Ti_5O_{12}$ and $Li_4Ti_5O_{12}$ within each particle. Because the coexisting phases only differ by their Li concentrations, the interfaces that separate them within a particular particle will be diffuse as schematically illustrated in Figure 7. The free energy of such a two-phase coexistence can be expressed as a volume integral of the homogeneous free energy and a term that accounts for the free energy penalty of concentration gradients that exist at diffuse interfaces according to[66,67]

$$G = \int [g(x) + K(\nabla x)^2]\frac{d\vec{r}}{\Omega} \tag{38}$$

Here, $g(x)$ is the Gibbs free energy of a homogeneous phase having a concentration x, K is the gradient energy coefficient that determines the contribution to the free energy due to concentration gradients ∇x and Ω refers to the volume per interstitial Li site. The concentration x appearing in eq 38 is itself a function of position $\vec{r}$.

The importance of eq 38 emerges when deriving an expression for the Li chemical potential of an inhomogeneous electrode particle consisting of coexisting phases separated by diffuse interfaces. As before, the Li flux is still related to the gradient in chemical potential according to eq 20. However, in the presence of steep concentration gradients at the diffuse interfaces separating coexisting phases, the chemical potential is no longer simply the slope of the homogeneous free energy with

https://dx.doi.org/10.1021/acs.chemrev.9b00601
Chem. Rev. 2020, 120, 6977−7019

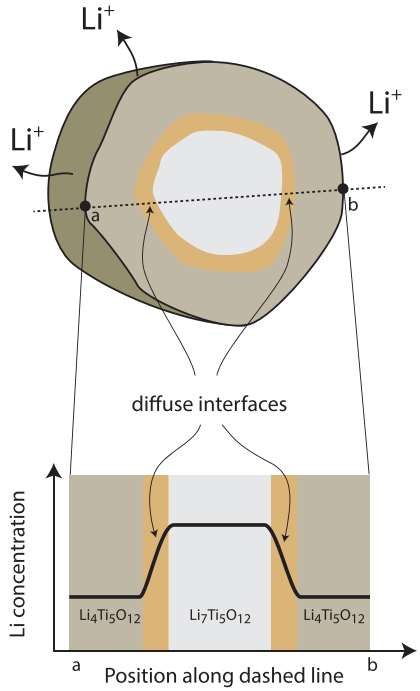

Figure 7. Schematic illustration of a particle consisting of a two phase mixture of $Li_7Ti_5O_{12}$ and $Li_4Ti_5O_{12}$ as it is being delithiated. Also shown is a schematic of the concentration profile along the dashed line passing through the interior of the particle. Because $Li_7Ti_5O_{12}$ and $Li_4Ti_5O_{12}$ share the same spinel crystal structure, the host remains continuous across the interface separating the two phases allowing for a diffuse interface characterized by a smooth variation of the Li concentration.

respect to x but also depends on the curvature of the concentration profile $x(\vec{r})$ according to[65]

$$\mu_{Li} = \frac{\partial g}{\partial x} - 2K\nabla^2 x \tag{39}$$

By inserting this form of the chemical potential into the flux expression eq 20 and substituting the resulting expression into the mass conservation law yields a differential equation that describes the evolution of a two-phase mixture in which the coexisting phases are separated by diffuse interfaces[65]

$$\frac{\partial C}{\partial t} = -\nabla J_{Li} = \nabla(D\nabla C - 2\Omega L\nabla(K\nabla^2 C)) \tag{40}$$

where as before, C is the number of Li per unit volume (i.e., $C = x/\Omega$). This partial differential equation is referred to as the Cahn−Hilliard equation and can be solved numerically provided suitable boundary conditions on the electrode particle surfaces are accounted for. The diffusion coefficient D is related to the Onsager transport coefficient L according to eq 24. The volume per interstitial site Ω is assumed to be independent of concentration, which is valid for an electrode chemistry such as $Li_7Ti_5O_{12}$.[62]

The two-phase reaction between spinel $Li_7Ti_5O_{12}$ and $Li_4Ti_5O_{12}$ has been modeled with a phase field approach.[68] However, evidence from first-principles calculations suggests that Li insertion and removal may not proceed as a simple two-phase reaction at macroscopic length scales but instead as a coexistence at the nanoscale.[69]

The effect of strain during a two-phase reaction is often very important. If the coexisting phases have different lattice parameters, they will need to be strained to remain coherent.[70,71] The resulting strain energy can be responsible for unexpected pattern formation during two-phase coexistence. This became especially evident in early experimental reports of peculiar two-phase coexistence patterns in Li_xFePO_4.[72] The olivine form of Li_xFePO_4 transforms from a Li lean α-Li_xFePO_4 phase to a Li rich β-Li_xFePO_4 without any crystallographic change of the $FePO_4$ host.[20] However, the host undergoes significant changes in lattice parameters, which leads to large strain energy penalties when the two phases coexist within the same particle. Strain energy contributions can be accounted for by modifying the starting free energy expression, eq 38, according to[73]

$$G = \int [f(x, \vec{e}) + K(\nabla x)^2]\frac{d\vec{r}}{\Omega} \tag{41}$$

where the homogeneous Gibbs free energy g is replaced by the homogeneous Helmholtz free energy, f, which is an explicit function of the six independent components of the strain tensor, $\vec{e} = (e_{xx}, e_{yy}, e_{zz}, e_{yz}, e_{xz}, e_{xy})$.[32,74] The dependence of f on $\vec{e}$ is quadratic for small strains, where linear elasticity holds.[32,75] The total free energy, eq 41, can be variationally minimized with respect to the displacement field for a fixed concentration profile $x(\vec{r})$ (subject to constant pressure boundary conditions) to determine the equilibrium strains $\vec{e}$.[65,75] The inclusion of an explicit dependence on strain in the free energy ensures that the Li chemical potential is also a function of strain in addition to concentration and temperature, thereby allowing for a natural coupling between chemistry and mechanics. It is in this manner that strain energy affects pattern formation during two-phase coexistence because Li diffusion down a chemical potential gradient will choose a path that simultaneously minimizes the chemical free energy and the strain energy.

The role of strain energy in selecting out a particular two-phase coexistence pattern is especially stark in Li_xFePO_4.[59,71,72,76−78] The crystallography of the Li_xFePO_4 host results in highly anisotropic one-dimensional Li diffusion along the b lattice vector of its orthorhombic cell.[79,80] Large particles of Li_xFePO_4 often adopt a plate-like shape as illustrated in Figure 8, where the large faces are perpendicular to the diffusion direction along the b lattice vector of the crystal.[72] Deintercalation of Li is expected to lead to a depletion of Li at the surface, which due to the miscibility gap in the Li_xFePO_4

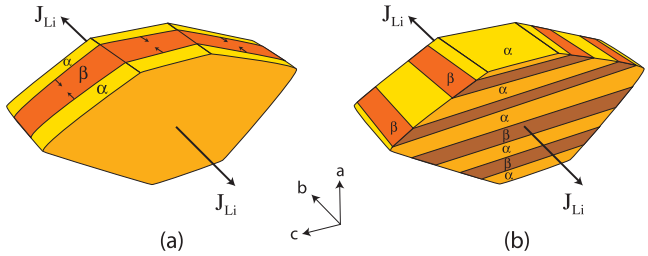

Figure 8. (a) Schematic illustration of a large Li_xFePO_4 electrode particle during deintercalation. Li diffusion in Li_xFePO_4 occurs along one-dimensional tunnels parallel to the b unit cell direction. Large electrode particles adopt a plate-like shape with the large surface perpendicular to the crystallographic Li diffusion direction. In the absence of strain energy penalties, the two-phase reaction between Li-depleted α-Li_xFePO_4, and Li-rich β-Li_xFePO_4 should occur with a diffuse interface perpendicular to the b axis. (b) Because of large changes in the lattice parameters between α and β, large misfit strains emerge that result in more complex two-phase coexistence patterns to minimize strain energy.

https://dx.doi.org/10.1021/acs.chemrev.9b00601
Chem. Rev. 2020, 120, 6977−7019

system should lead to a transformation to the Li-poor form of Li_xFePO_4 at the surface.[81] The Li-depleted α Li_xFePO_4 should then continue to extend into the particle through a diffusional growth mechanism as illustrated in Figure 8a. TEM observations by Chen et al.,[72] however, showed that Li removal leads to a lamellar mixture of Li-rich β and Li-poor α forms of Li_xFePO_4 as schematically illustrated in Figure 8b. This peculiar two-phase microstructure in large Li_xFePO_4 particles cannot be predicted with a simple application of the Cahn−Hilliard model (without the inclusion of strain effects)[82,83] and instead emerges from a complex interplay between strain energy reduction, interfacial energy minimization, and optimal transport pathways that are coupled to spinodal instabilities,[59,77,84,85] as was demonstrated by continuum simulations of elasticity and Li transport.[78]

Even more complex chemomechanical couplings occur in intercalation compounds such as spinel $Li_xMn_2O_4$, which are susceptible to very strong Jahn−Teller instabilities at high Li concentrations. Li insertion into cubic $LiMn_2O_4$ leads to the formation of a tetragonally distorted $Li_2Mn_2O_4$ phase through a two-phase reaction.[25] The change in symmetry occurs due to a cooperative Jahn−Teller distortion of the MnO_6 octahedra without otherwise modifying the topology of the original spinel host of $LiMn_2O_4$. The host crystal structure of $Li_2Mn_2O_4$ thereby undergoes a large tetragonal strain relative to the starting cubic $LiMn_2O_4$ phase. While having many similarities to the topotactic two-phase reactions of $Li_7Ti_5O_{12}$ and Li_xFePO_4, the Jahn−Teller instability in Li rich $Li_2Mn_2O_4$ requires an extension of the Cahn−Hilliard theory to allow for the possibility of chemomechanical spinodal decomposition.[86]

2.3.2. Stacking Sequence Change Phase Transformations. Many electrode materials used in commercial Li-ion batteries, including Li_xCoO_2, $Li_x(Ni_{1-y-z}Co_yAl_z)O_2$ (NCA), $Li_x(Ni_{1-y-z}Mn_yCo_z)O_2$ (NMC), and graphite, have a layered crystal structure.[17,87] Li_xCoO_2, for example, is made of two-dimensional CoO_2 slabs, while graphite is a stacking of graphene sheets (carbon forming a honeycomb network). A large fraction of promising electrode chemistries for Na-ion and K-ion batteries also adopt a layered crystal structure.[88]

Layered intercalation compounds often undergo phase transformations in which the preferred stacking sequence of the two-dimensional building blocks changes with the concentration of the intercalating species. For example, while the graphene sheets of graphite adopt an ABAB stacking sequence in the absence of Li, they change their relative alignment to an AA stacking sequence in LiC_6, the fully intercalated compound. Similarly, the preferred stacking sequence of the CoO_2 slabs of Li_xCoO_2 changes at low Li concentration. The oxygen ions of Li_xCoO_2 form close-packed two-dimensional layers that stack according to an ABCABC sequence with Co and Li ions filling alternating layers of interstitial sites within the oxygen sublattice. Upon complete removal of the Li ions from Li_xCoO_2, the CoO_2 slabs glide relative to each other to produce a new layered crystal in which the close-packed oxygen layers adopt an ABAB stacking sequence.[23] Stacking sequence changes are especially prevalent in layered intercalation compounds of Na-ion and K-ion batteries and pose a major impediment to achieving high cycle lifetimes.[88]

While no direct experimental observations of these transformations have been made, a mechanism based on the migration of partial dislocations has been proposed by Gabrisch et al.[89] The dislocation structure in Li_xCoO_2, for example, should be very similar to that of fcc metals because the oxygen sublattice of $LiCoO_2$ is that of a rhombohedrally distorted fcc lattice. As argued by Gabrisch, the transition from an ABCABC stacking sequence of close-packed oxygen planes in $LiCoO_2$ to an ABAB stacking sequence in CoO_2 can be realized by the migration of Shockley partial dislocations.[89] Figure 9, for example, illustrates how an array of partial dislocations can transform a Na_xCoO_2 particle starting with the ABCABC stacking sequence of close-packed oxygen planes of O3 to an ABBCCA stacking sequence of P3.[90] Stacking sequence phase transformations can lead to surface roughening that can in turn damage coatings or SEI layers.[91] A continuum/mesoscale model of stacking sequence change phase transformations has yet to be developed. Such a theory must account for the chemomechanical coupling between chemical driving forces set up by diffusion and the long-range elastic interactions that emerge when partial dislocations accumulate at the interface.

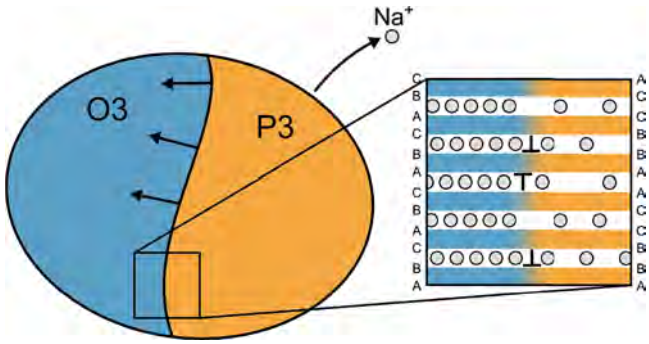

Figure 9. Schematic illustration of a particle consisting of a two phase mixture of O3 and P3. A possible mechanism to accommodate the coherent two-phase coexistence of phases having a different stacking sequence of close-packed oxygen planes is with a periodic array of partial dislocations (denoted by "T"s and upside down "T"s). The stacking sequences on both sides of the interface are shown in the inset. Adapted from ref 90. Copyright 2019 the Royal Society of Chemistry.

2.3.3. Reconstructive Phase Transformations. While most electrodes for alkali-ion batteries are intercalation compounds that host guest cations in interstitial sites of their crystal, there are several examples in which the insertion mechanism proceeds according to an alloying or conversion reaction. Silicon, tin, and antimony-based anodes,[54,55,92] for example, rely on an alloying reaction, while conversion reactions have received attention due to their promise of very high capacities.

In general, the phases that emerge during an alloying or conversion reaction upon Li insertion have little or no crystallographic relationship with the starting phase. Reconstructive reactions occur with a nucleation and growth mechanism with sharp interfaces separating the growing phase from the consumed starting phase. Because of the reconstructive nature of the phase transformation, the interfaces separating the growing and shrinking phases are incoherent or at best semicoherent. They generally also result in drastic changes in the micro- and nanostructure of the starting electrode, which is exacerbated with every charge/discharge cycle. The starting electrode morphologies are highly susceptible to aggressive coarsening reactions that undo any initial optimizations through nanostructuring. Approaches to model alloying and conversion reactions at the meso and continuum scale generally rely on a phase field[29,93] approach or a level-set approach.[94] A phase field approach approximates the interfaces as diffuse and is generally

https://dx.doi.org/10.1021/acs.chemrev.9b00601
Chem. Rev. 2020, 120, 6977−7019

straightforward to implement from a numerical point of view. The input parameters to a phase field model (free energies and mobilities) when applied to a reconstructive phase transformation, however, are only tenuously related to quantities that can be predicted at the atomic scale. A level-set approach more rigorously treats the interfaces as sharp transitions between coexisting phases and has a clearer connection to lower length scale models. Phase field models have also been developed to model fracture processes in electrode materials.[95−97]

3. COMPUTATIONAL TECHNIQUES

In section 2, we have presented a phenomenological description of important thermodynamic and kinetic properties associated with electrodes, electrolytes, and electrode/electrolyte interfaces. The macroscopic framework elaborated on above is rigorous but requires experimental input to determine free energy functions and kinetic rate coefficients. An alternative approach is to start from fundamental laws of physics and calculate the thermodynamic and kinetic ingredients to the phenomenological descriptions of batteries. First-principles approaches have proven very successful in predicting and elucidating qualitative trends and behavior and in some cases have even allowed the prediction of properties to a high degree of quantitative accuracy.

The many-body Schrödinger equation from quantum mechanics is the formal starting point for such an endeavor. In principle, its solution yields a spectrum of allowed energy levels and the associated electronic wave functions of a collection of atoms, and by extension, its basic properties such as the equilibrium dimensions (e.g., lattice parameters of a crystal) and atomic positions, the total energy and the electronic structure. In practice, the many-body Schrodinger equation of realistic solids cannot be solved exactly and approximate approaches must be used.

3.1. First-Principles Electronic Structure

3.1.1. Density Functional Theory. Density functional theory (DFT)[5,6] is by far the most common approach used in approximating solutions to the many-body Schrödinger equation today. As such, there are a wide array of excellent textbooks[98] and reviews of the technique, and interested readers are referred to those for a more detailed exposition. Here, we will only provide a brief summary of the formalism and focus instead on the key challenges in the application of DFT to battery properties and how these challenges have been mitigated.

DFT has its origins in the two Hohenberg−Kohn theorems.[5] The first Hohenberg−Kohn theorem states that the ground-state properties of a many-electron system are uniquely determined by its electron density that depends on only three spatial coordinates. The second Hohenberg−Kohn theorem defines an energy functional $\hat{E}$ for the system, which is minimized for the ground state electron density $n(\vec{r})$, as follows:

$$\ddot{E}[n(\vec{r})] = \hat{T}[n(\vec{r})] + \hat{V}[n(\vec{r})] + \hat{r}[n(\vec{r})] \tag{42}$$

where $\hat{T}$, $\hat{V}$, and $\hat{U}$ are the kinetic energy, external potential (typically the potential exerted by the nuclei for a system of atoms), and electron−electron Coulomb and exchange interaction functionals, respectively. In the Kohn−Sham variant of DFT[6] (KS-DFT), this many-body problem is further mapped to a more tractable problem of noninteracting electrons moving in an effective potential $V_s(\vec{r})$, given as follows:

$$V_s(\vec{r}) = V(\vec{r}) + \int \frac{e^2 n_s(\vec{r})}{|\vec{r} - \vec{r}'|} + V_{xc}[n_s(\vec{r})] \tag{43}$$

where $V(\vec{r})$ is the external potential, the second term denotes the electron−electron repulsion, and V_{xc} is known as the exchange-correlation potential. $n_s(\vec{r})$ is the charge density of the noninteracting system of electrons.

Approximating the exchange-correlation functional V_{xc} is the key problem within KS-DFT. In the simplest local density approximation (LDA), V_{xc} is based on the exact exchange energy and parametrized correlation energy for a uniform electron gas. By far the most common exchange-correlation functionals in use today are based on the generalized gradient approximation (GGA), which incorporates the gradient of the density to account for the nonhomogeneity of the true electron density.[7] While semilocal LDA and GGA functionals have been remarkably successful in predicting many materials properties, a well-known limitation is that they significantly underestimate redox potentials due to the incomplete cancellation of electron self-interaction errors.[99] Hence, accurate calculations of the voltages of transition metal oxide electrodes are usually performed using the Hubbard U extension to DFT, where the U parameter is determined either self-consistently or by fitting to experimental oxidation energies.[100] Alternatively, accurate redox potentials can also be obtained without adjustable parameters, albeit at much higher computational cost, using hybrid functionals (e.g., the screened Heyd−Scuseria−Erzernof or HSE functional[101,102]) that incorporate a fraction of exact Hartree−Fock exchange, which cancels the electron self-interaction by design.[103] Functional development remains an active area of research and there exist a whole spectrum of functionals and approaches beyond semilocal LDA and GGA aimed at obtaining more accurate geometries, energies,[104,105] electronic structure,[106] modeling of van der Waals interactions,[107,108] etc.

3.1.2. From DFT to Approximate Battery Properties. It is already possible to approximate several important macroscopic battery properties with reasonable accuracy starting with the basic outputs from a DFT structural relaxation and energy calculation. For instance, the *average* voltage (versus a metallic Li anode) of a cathode Li_nX when charged to $Li_{n-x}X$ can be related to the change in the Gibbs free energy, which can in turn be approximated by the change in the 0K DFT energy, as follows:[109]

$$V = -\frac{G[\mathrm{Li}_n\mathrm{X}] - G[\mathrm{Li}_{n-x}\mathrm{X}] - xG[\mathrm{Li}]}{xe} \approx -\frac{E_{\mathrm{DFT}}[\mathrm{Li}_n\mathrm{X}] - E_{\mathrm{DFT}}[\mathrm{Li}_{n-x}\mathrm{X}] - xE_{\mathrm{DFT}}[\mathrm{Li}]}{xe} \tag{44}$$

where x is the number of Li transferred per formula unit during the charge process, G and E_{DFT} refer to the Gibbs free energy and the computed DFT energy, respectively, and e is the electron charge. This expression emerges when integrating the Nernst eq (eq 7) over a Li composition interval x. It is a good approximation for the voltage of an intercalation compound that undergoes a two-phase reaction, such as $LiFePO_4$, assuming that all intermediate stable phases are correctly identified with DFT. The approximation, however, neglects all finite-temperature effects and is therefore unable to predict the voltage profile of intercalation compounds that operate via a solid solution mechanism.

https://dx.doi.org/10.1021/acs.chemrev.9b00601
Chem. Rev. 2020, 120, 6977−7019

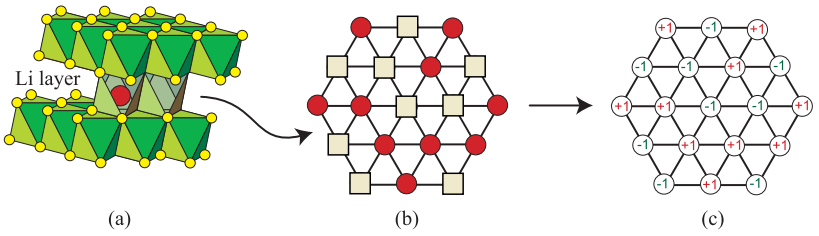

Figure 10. Disorder among Li ions and vacancies within an intercalation compound can be represented by assigning occupation variables assigned to each interstitial site. (a) The Li ions of a layered intercalation compound such as the O3 form of Li_xCoO_2 reside in octahedral interstitial sites that form two-dimensional triangular lattices. (b) The removal of Li typically results in Li vacancy disorder (red represents Li ions and green represents vacancies). (c) A particular ordering can be mapped onto an array of +1's (for Li occupancy) and −1's (vacancy occupancy).

Other properties that can be predicted with simple DFT calculations and crystallographic considerations include the theoretical specific capacity and volumetric capacity. The theoretical specific capacity and volumetric capacity are simply given by the number of Li that can be extracted per formula unit divided by the total molecular weight and volume (which is sometimes obtained via a DFT relaxation) per formula unit, respectively. Multiplying the average voltage by the theoretical specific capacity and volumetric capacity then yields the theoretical specific energy and energy density, respectively.

3.2. Statistical Mechanics

3.2.1. Linking Thermodynamics to Electronic Structure. Statistical mechanics makes it possible to connect the temperature-dependent macroscopic properties of a battery material to its underlying electronic structure. The key equation is the partition function, which at constant temperature and Li concentration takes the form[110]

$$Z = \sum_s \exp\left(\frac{-E_s}{k_B T}\right) \tag{45}$$

The sum extends over all atomic and electronic excitations within the solid, and E_s corresponds to the energy of excitation s, which in principle could be calculated with DFT.

It is possible to distinguish between three classes of excitations in intercalation compounds: (i) electronic excitations, including for example the excitation of a valence band electron to a conduction band, (ii) vibrational excitations due to thermal atomic motions around their ideal crystalline sites, and (iii) configurational degrees of freedom associated with all possible ways of distributing Li ions and vacancies over the interstitial sites of the intercalation host. While electronic and vibrational excitations affect thermodynamic potentials quantitatively, by far the most important contribution to the thermodynamic properties of an intercalation compound are excitations that arise from configurational degrees of freedom. Configurational excitations are not necessarily restricted to the different ways of distributing Li-ions and vacancies over the interstitial sites of a host but can also emerge from the different ways of distributing various localized oxidation states, if the compound exhibits localized electronic states. An example is the configurational entropy arising from all possible ways of distributing +2 and +3 oxidation states over the Fe sites of the olivine Li_xFePO_4 host.[111]

Formally, the Helmholtz free energy is linked to the partition function according to

$$F = k_B T \ln Z \tag{46}$$

All other thermodynamic properties can then be extracted by applying appropriate derivatives to the free energy with respect to experimentally controlled variables.

3.2.2. Effective Hamiltonians: The Cluster Expansion. Well-established techniques exist to calculate the contribution of electronic and vibrational excitations to the thermodynamic properties of solids and are treated in most standard solid-state physics and statistical mechanics textbooks.[112,113] A rigorous treatment of configurational degrees of freedom is less common and will be briefly reviewed here. It relies on a mathematical formalism that allows for an unambiguous characterization of configurational degrees of freedom through the introduction of occupation variables assigned to each crystallographic site that can be populated by more than one atomic specie (e.g., Li and vacancies).[46,114,115] The sublattices of interstitial sites of an intercalation host generally exhibit different degrees of Li vacancy disorder as a function of Li concentration. Figure 10 illustrates a snapshot of a particular Li vacancy arrangement within a Li layer of a layered intercalation compound. By assigning an occupation variable σ_i to each site i that is +1 if occupied by Li and −1 if vacant, it becomes possible to represent the state of configurational disorder of Figure 10b by an array of +1's and −1's as illustrated in Figure 10c. In effect, any particular Li vacancy configuration of the M interstitial sites of the host can formally be represented by a vector of occupation variables $\vec{\sigma} = (\sigma_1, ..., \sigma_i, ..., \sigma_M)$. There are exactly 2^M ways to arrange Li ions and vacancies over the M interstitial sites of the host.

Unique mathematical properties emerge when considering polynomials of occupation variables belonging to clusters of sites.[114,116] For example, the polynomial $\Phi_\alpha = \sigma_i\sigma_j$ is made up of a product of occupation variables belonging to a nearest neighbor cluster, α, of sites as illustrated in Figure 11. Similar polynomials can be formed for any cluster of sites of arbitrary size. $\Phi_\beta = \sigma_k\sigma_l$ corresponds to a cluster function for a particular second nearest neighbor cluster, β, while $\Phi_\gamma = \sigma_m\sigma_n\sigma_o$ is a cluster function for a cluster of three sites, γ, as illustrated in Figure 11. There are exactly 2^M such polynomial cluster functions for a crystal having M interstitial sites. Sanchez et al.[114,116] were able to show that the 2^M cluster functions form a complete and orthonormal basis over the discrete multivariable space of M occupation variables. Any property of the crystal that depends on how the Li ions and vacancies are arranged over the interstitial sites of the crystal can, therefore, be expressed as an expansion of these basis functions. For example, the energy of the crystal (neglecting vibrational and electronic excitations) will depend on how Li ions are distributed over the interstitial sites. This dependence can be expressed as a series expansion of the polynomial cluster functions according to[114]

https://dx.doi.org/10.1021/acs.chemrev.9b00601
Chem. Rev. 2020, 120, 6977−7019

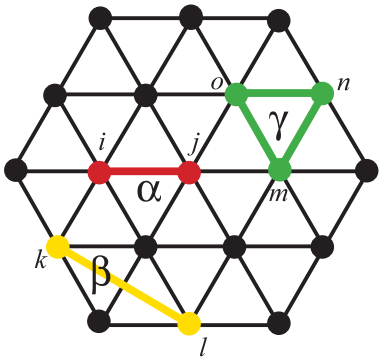

Figure 11. Basis functions can be constructed as the product of occupation variables belonging to different clusters of sites, such as a nearest-neighbor pair cluster (labeled α), a second nearest neighbor (β), and a triplet (γ). While only three clusters are shown, a total of 2^M clusters of sites and corresponding cluster basis functions exist for a crystal having M sites.

$$E(\vec{\sigma}) = V_o + \sum_{\alpha} V_\alpha \Phi_\alpha(\vec{\sigma}) \tag{47}$$

where V_o and V_α are expansion coefficients whose values are determined by the crystallography and chemistry of the intercalation compound. The sum extends over all 2^M polynomial cluster functions Φ_α, where α is a summation index over all possible clusters of interstitial sites. The above series expansion can often be truncated above a maximal sized cluster while still predicting the configurational energy with an accuracy close to that of first-principles electronic structure methods. A common approach to determining the expansion coefficients, V_o and V_α, is through an inversion method, whereby a truncated cluster expansion is made to reproduce first-principles energies of a subset of the 2^M possible Li vacancy configurations. This is typically done with a least-squares procedure in combination with one of several schemes to determine the optimal truncation of the cluster expansion.[46,117−120] A truncated cluster expansion can be rapidly evaluated, making it ideal to extrapolate computationally demanding first-principles energy calculations performed for a few Li vacancy configurations to the energy of arbitrary Li vacancy configurations.

3.2.3. Equilibrium Monte Carlo Simulations. Although all thermodynamic properties of a system can formally be derived from the partition function Z, eq 45, the partition function is not a quantity that can be explicitly evaluated through a direct summation of microstates for systems of interacting particles. Rather, numerical sampling methods such as Monte Carlo simulations are necessary to evaluate relevant thermodynamic averages. A common Monte Carlo approach relies on importance sampling techniques, whereby a subset of all possible configurations are sampled with a frequency given by the equilibrium probability distribution function of statistical mechanics.

For a Li intercalation compound, it is often most convenient to impose a constant Li chemical potential as a thermodynamic boundary condition. This corresponds to the grand canonical ensemble. By imposing a fixed Li chemical potential, μ_{Li} (while keeping the concentration of the host atoms fixed), there is no constraint on the number of Li in each microstate and the number of Li will therefore fluctuate from one microstate to the next. When only considering configurational degrees of freedom, the partition function for the intercalation compound at fixed T, μ_{Li}, and number of host atoms, then takes the form

$$Z = \sum_{\vec{\sigma}} \exp\left(-\frac{E(\vec{\sigma}) - \mu_{Li} N_{Li}(\vec{\sigma})}{k_B T}\right) \tag{48}$$

A Monte Carlo simulation acts on an explicit array of occupation variables $\vec{\sigma}$, corresponding to a finite sized crystal having $L_1 \times L_2 \times L_3$ unit cells with periodic boundary conditions often being imposed. The metropolis Monte Carlo algorithm samples configurations $\vec{\sigma}$ with a frequency given by the probability distribution of statistical mechanics, which in the grand canonical ensemble is given by

$$P(\vec{\sigma}) = \frac{1}{Z} \exp\left(-\frac{E(\vec{\sigma}) - \mu_{Li} N_{Li}(\vec{\sigma})}{k_B T}\right) \tag{49}$$

This approach allows a numerical evaluation of thermodynamic quantities such as the average number of Li ions

$$\langle N_{Li} \rangle = \sum_{\vec{\sigma}} P(\vec{\sigma}) N_{Li}(\vec{\sigma}) \tag{50}$$

and the average grand canonical energy (defined as $\Lambda = E - \mu_{Li} N_{Li}$)

$$\langle \Lambda \rangle = \sum_{\vec{\sigma}} P(\vec{\sigma}) \Omega(\vec{\sigma}) \tag{51}$$

both at constant Li chemical potential μ_{Li} and temperature T. Because the Monte Carlo algorithm samples microstates with the probability distribution $P(\vec{\sigma})$, a direct averaging is performed during the simulation according to

$$\langle A \rangle = \frac{1}{N_{samples}} \sum_{\vec{\sigma}} A(\vec{\sigma}) \tag{52}$$

where A is a quantity such as N_{Li} or Ω and where the sum extends over a finite number of sampled microstates. Details about algorithmic aspects of Monte Carlo simulations can be found elsewhere.[121]

Monte Carlo simulations enable the calculation of equilibrium relations between thermodynamic quantities. For example, a relationship can be calculated between the Li chemical potential, μ_{Li}, and the Li concentration within an intercalation host at a particular temperature, T, by calculating $\langle N_{Li} \rangle$ at different μ_{Li} with grand canonical Monte Carlo simulations. The resulting relationship can then be substituted into the Nernst eq 7 to obtain a calculated voltage profile at finite temperature. It can also be used to calculate the Gibbs free energy[122−124] by, for example, numerically integrating eq 4 according to

$$G(\langle N_{Li} \rangle, T) = G(\langle N_{Li}^o \rangle, T) + \int_{N_{Li}^o}^{N_{Li}} \mu_{Li}\, d\langle N_{Li} \rangle \tag{53}$$

where $G(\langle N_{Li}^o \rangle, T)$ is the free energy in a particular reference state. Commonly chosen reference states are dilute limits, such as the fully deintercalated compound or the fully intercalated compound, as these states have negligible configurational entropy. The Gibbs free energy $G(\langle N_{Li}^o \rangle, T)$ can then be approximated by the average energy of the compound (possibly augmented with an ideal solution entropy term, which becomes exact in the dilute limit). Normalization of the Monte Carlo Gibbs free energy by the number of interstitial sites within the Monte Carlo simulation cell, M, then yields the free energy $g = G/M$ as a function of the Li concentration $x = \langle N_{Li} \rangle / M$.

https://dx.doi.org/10.1021/acs.chemrev.9b00601
Chem. Rev. 2020, 120, 6977−7019

In summary, the approach to calculating finite-temperature thermodynamic properties of intercalation compounds due to configurational degrees of freedom has three distinct steps. First, the energies of several hundred Li vacancy arrangements within the intercalation compound are calculated from first principles. These energies are then used to fit the expansion coefficients of a truncated cluster expansion. Finally, the truncated cluster expansion is implemented in Monte Carlo simulations with which a variety of thermodynamic quantities are calculated.

3.3. Modeling Ionic Mobility

In this section, we review the common computational approaches for calculating properties related to ionic mobility in batteries. It should be noted that while all the techniques discussed are generally applicable, practical considerations substantially influence the classes of materials in which each technique has been applied. Some of these practical considerations will be alluded to below, but a more detailed discussion will be given in section 4.

3.3.1. Nudged Elastic Band. The migration barriers, ΔE_b, for atomic hops that can be described with transition state theory (eq 22) play a key role in determining the rate with which cations diffuse within a solid. ΔE_b for a particular hop is defined as the barrier along the minimum energy path (MEP) connecting the end states of the hop. Both the MEP and ΔE_b can be obtained with the nudged elastic band (NEB) method.[125,126]

In the NEB approach, a number of intermediate "images" is first constructed along an initial guess for the MEP for a specific atomic configuration and diffusion event. A constrained optimization is then carried out to find the lowest possible energy for the images while maintaining spacing between neighboring images. This is achieved by adding "spring" forces along the band between images and projecting out the component of the force due to the potential perpendicular to the band. The energy difference between the highest and lowest energy points along the MEP determines the effective barrier ΔE_b for the diffusion event.

The reaction coordinate along the MEP is defined by the entire set of $3N$ atomic coordinates for a system of N atoms. The NEB method is, therefore, generally applicable to any diffusion event defined by the $3N$ atomic coordinates, be it a single ion hop between adjacent sites or coordinated multi-ion motion. In practice, however, the requirement to provide a reasonable initial guess for the MEP means that the NEB method is most commonly applied to the former scenario. The NEB method can be applied at dilute concentrations to calculate ΔE_b for an isolated cation performing a hop in an otherwise empty host crystal or for a cation hopping into an isolated vacancy. These relatively straightforward calculations provide a useful assessment of whether ions are sufficiently mobile within that particular lattice framework. The NEB method is also frequently used to compute environment-dependent migration barriers at nondilute concentrations, which are the key inputs to kinetic Monte Carlo simulations.

3.3.2. Kinetic Monte Carlo. Diffusion in most intercalation compounds is the result of a large number of stochastic atomic hops. Individual hop events occur with frequencies that can be estimated with transition state theory according to eq 22. The Li ions of intercalation compounds are generally present at nondilute concentrations, exhibiting varying degrees of short and long-range order as a function of temperature and overall composition. This complicates the calculation of transport coefficients because the migration barriers, ΔE_b, and the vibrational prefactors, ν^*, appearing in the expression for the hop frequency will both be a function of the local degree of ordering among the Li-ions and vacancies. Figure 12, for example, illustrates a typical snapshot of a local Li vacancy configuration over the octahedral sites of a layered intercalation compound. The Li ion performing the hop labeled 1 is completely surrounded by vacancies, while the Li ions performing the hops labeled 2 and 3 are surrounded by only one and three vacancies, respectively. Each of the three hops of Figure 12 will have a different migration barrier and vibrational prefactor due to differences in the local surroundings. An additional complexity that arises at nondilute concentrations is that the end states of a hop are rarely equivalent by symmetry and therefore have different energies. A consequence of this broken symmetry is that the migration barrier for a forward hop will differ from that of a backward hop. Hence, the migration barrier not only depends on the local degree of ordering but also on the direction of the hop, as schematically illustrated in Figure 13a,b.

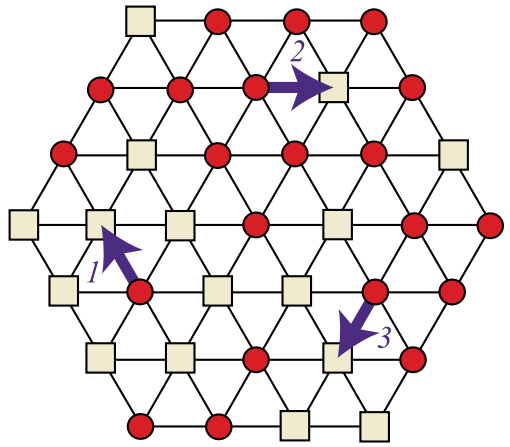

Figure 12. Intercalation compounds are often nondilute and exhibit wide variations in the degree of Li vacancy ordering. The migration barriers of hops in the presence of disorder can depend strongly on the local arrangement of Li ions and vacancies. Hop 1 occurs in a local environment having a high concentration of vacancies, while hop 2 occurs in an environment that is very Li rich. Hop 3 occurs in an environment that has an almost equal number of Li and vacancies.

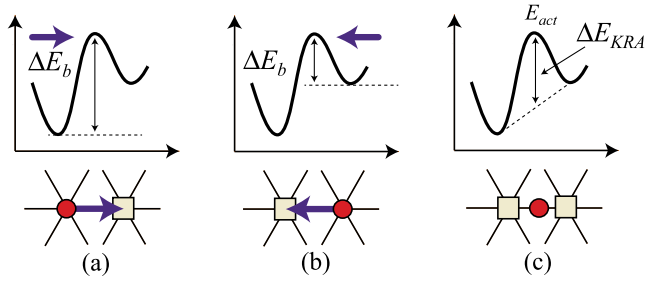

Figure 13. End states of hops in nondilute intercalation compounds are rarely symmetrically equivalent. The energies of the end states of a hop are then different such that the migration barrier for a forward hop (a) differs from that of a reverse hop (b). The kinetically resolved activation barrier, ΔE_{KRA}, is a measure of the kinetic barrier that is independent of the direction of the hop (c).

https://dx.doi.org/10.1021/acs.chemrev.9b00601
Chem. Rev. 2020, 120, 6977−7019

An unambiguous measure of the migration barrier for a particular hop environment can be obtained by averaging over the forward and backward hop barriers. This quantity, referred to as a kinetically resolved activation (KRA) barrier,[51] is independent of the hop direction and only depends on the local degree of ordering, denoted by $\vec{\sigma}_H$, which collects all occupation variables associated with Li sites of the host minus the sites directly involved in the hop H. The KRA barrier, ΔE_{KRA}, can be written in terms of the energies of the activated state, $E_{\mathrm{act}}(\vec{\sigma}_H)$, and the end states according to[46,51]

$$\Delta E_{\mathrm{KRA}}(\vec{\sigma}_H) = E_{\mathrm{act}}(\vec{\sigma}_H) - \frac{1}{2}(E(\vec{\sigma}_{\mathrm{initial}}) + E(\vec{\sigma}_{\mathrm{final}})) \tag{54}$$

The dependence of the end state energies, $E(\vec{\sigma}_{\mathrm{initial}})$ and $E(\vec{\sigma}_{\mathrm{final}})$, on the arrangement of Li ions and vacancies within the host can be described with a cluster expansion as described in section 3.2.2. Similarly, it is possible to describe the dependence of ΔE_{KRA} on the Li vacancy ordering surrounding the hop, $\vec{\sigma}_H$, with a local cluster expansion[46,51]

$$\Delta E_{\mathrm{KRA}}(\vec{\sigma}_H) = K_{\mathrm{o}} + \sum_{\alpha} K_\alpha \Phi_\alpha(\vec{\sigma}_H) \tag{55}$$

where the basis functions $\Phi_\alpha(\vec{\sigma})$ have a similar functional dependence on the occupation variables, σ_i, as in the cluster expansion of the energy (section 3.2.2). The expansion coefficients, K_α, are adjustable parameters that can be trained to a large database of KRA barriers for different local environments as calculated from first principles.

When the energies of the end states of a hop, $E(\vec{\sigma}_{\mathrm{initial}})$ and $E(\vec{\sigma}_{\mathrm{final}})$, and the energy of the KRA barrier, $\Delta E_{\mathrm{KRA}}(\vec{\sigma}_H)$, are known, it is possible to recover the migration barrier according to

$$\Delta E_b = \Delta E_{\mathrm{KRA}}(\vec{\sigma}_H) + \frac{1}{2}[E(\vec{\sigma}_{\mathrm{final}}) - E(\vec{\sigma}_{\mathrm{initial}})] \tag{56}$$

All terms on the right can be parametrized with a cluster expansion, making it possible to evaluate the migration barrier of a hop for any surrounding Li vacancy arrangement. The configuration dependence of the vibrational prefactor, ν^*, can be represented in a similar manner.[46] The ability to calculate the migration barriers and vibrational prefactors in any ordered or disordered state using cluster expansion Hamiltonians is especially convenient in kinetic Monte Carlo simulations, which sample the Li trajectories, ΔR_i, needed to calculate transport coefficients such as L (eq 21).

A kinetic Monte Carlo simulation, as applied to an intercalation compound, evolves a microstate $\vec{\sigma}$ by stochastically sampling hop events. There are two steps in a kinetic Monte Carlo simulation that are repeated over and over again until a sufficient number of hops have been performed.[127,128] In the first step, starting from a Li vacancy ordering $\vec{\sigma}$, a hop, H, is selected with a probability that is proportional to its hop frequency, Γ_H. This is done by calculating the hop frequencies, Γ_h, of all possible hop events, $h = 1, ..., N_{\mathrm{hops}}$, in Li vacancy ordering $\vec{\sigma}$. A random number $\zeta \in (0, 1)$ is then chosen and used to identify a hop using the inequality

$$\sum_{h=1}^{H-1} \Gamma_h < W\zeta \le \sum_{h=1}^{H} \Gamma_h \tag{57}$$

where $W = \sum_{h=1}^{N_{\mathrm{hops}}} \Gamma_h$ is the sum of hop frequencies for all possible hops in microstate $\vec{\sigma}$. The larger the hop frequency Γ_H, the more likely hop H will be selected. Once a hop H has been selected, a new Li vacancy configurations $\vec{\sigma}'$ is generated whereby the Li and vacancy belonging to the hop H in $\vec{\sigma}$ have been exchanged. The second step of a kinetic Monte Carlo simulation is then to update the physical time. This is done by selecting another random number $\lambda \in (0, 1)$ and estimating the waiting time for the hop to occur by

$$\Delta t = -\frac{1}{W}\ln(\lambda) \tag{58}$$

This expression is derived from a Poisson distribution of rare events.[127,128] The two steps are repeated until sufficiently long trajectories have been sampled. The sampled trajectories can then be used to calculate the various transport and diffusion coefficients of section 2.2.2.

3.3.3. Molecular Dynamics. Molecular dynamics (MD) is a simulation approach to probe the dynamic evolution of a system of atoms. The key input to MD simulations is the description for the interactions between atoms, i.e., the potential energy surface or PES. In ab initio MD (AIMD), the PES is obtained by solving the Schrödinger equation, within either the Born−Oppenheimer[129] or Car−Parrinello[130] approaches. In classical MD, these interactions are modeled using parametrized interatomic potentials (IAPs). Traditionally, these IAPs are based on mathematical functions parametrized to experiments or ab initio calculations.[131−133] The main trade-off between ab initio and classical MD is between computational cost, accuracy, and transferability. The former is highly accurate and generally applicable across the periodic table, but its computational expense and poor scalability ($>O(N^3)$) limit typical simulations to relatively small system sizes (<1000 atoms) and short time scales (~100 ps). The latter, on the other hand, have been applied to large system sizes (up to millions of atoms) and long time scales (>1 ns), but developing a sufficiently accurate IAP for a specific chemistry of interest is challenging.

More recently, machine learning (ML) of the relationship between PES and local environment descriptors have emerged as a promising alternative providing a general IAP development approach.[134−144] In a typical ML-IAP fitting workflow, a sufficiently large data set of representative structures is first sampled, for example, by extracting snapshots from AIMD simulations or carefully chosen displacements from equilibrium structures, and their energies and forces are computed using DFT computations. The sampled structures are then expressed in terms of atomic local environment descriptors that satisfy rigorous invariances with respect to translation, rotation, and permutation of similar species, such as symmetry functions, moment tensors, bispectrum, and smooth overlap of atomic positions. Finally, a machine learning model, e.g., linear regression,[136,141] Gaussian process regression[137] or neural network,[134] is then applied to learn the PES as a function of the local environment descriptors. Such ML-IAPs have been demonstrated to yield near-DFT accuracy in energies and forces, generally outperforming classical IAPs, across diverse chemistries.[145]

The key output from MD simulations is the trajectories of the atoms with time, from which properties such as the mobile ion diffusivity, conductivity, and other material properties can be obtained. For example, the jump diffusivity D_J (eq 27) can be obtained from the slope of the plot of the mean square displacement (MSD) of the center of mass of the mobile ions with respect to time, while the tracer diffusivity D^* (eq 28) can be obtained from the slope of the plot of the averaged MSD of individual mobile ions with respect to time (Figure 14a). The

https://dx.doi.org/10.1021/acs.chemrev.9b00601
Chem. Rev. 2020, 120, 6977−7019

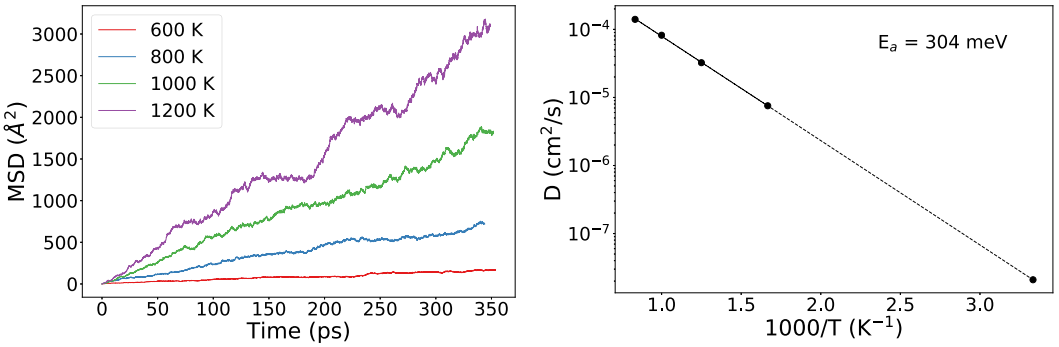

Figure 14. An example of (a) a mean square displacement (MSD) vs time and (b) Arrhenius plot of diffusivities from MD simulations performed at elevated temperatures.

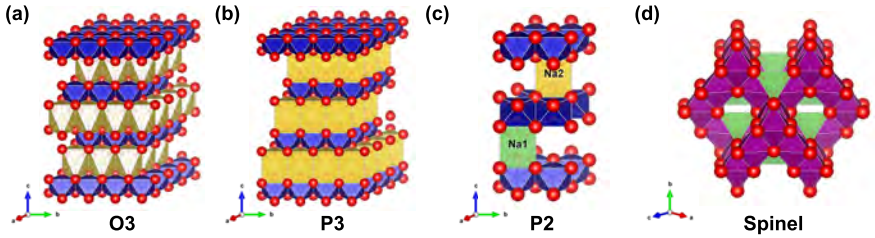

Figure 15. Structures for layered A_xMO_2 in (a) O3, (b) P3, (c) P2 stackings, and (d) spinel $A_xM_2O_4$. In the notation for layered structures proposed by Delmas, the letter indicates the coordination of the alkali ion (O, octahedral; P, prismatic) and the numeral indicates the number of layers per repeating unit. Red atoms are oxygen, blue/magenta atoms are transition metals (M), and yellow/green atoms are alkali.

conductivity of the mobile ion and the Haven ratio can then be obtained via eqs 37 and 29, respectively. It should be noted that the slow convergence of the MSD of the center of mass of the mobile ions means that calculations of D_J is usually obtained via classical MD simulations (or alternatively, kinetic Monte Carlo), while D^* is more accessible via AIMD simulations, at least for relatively fast ion conductors. Further, by performing MD simulations at multiple temperatures, an Arrhenius plot (Figure 14b) of $\log(D)$ versus $1/T$ can be constructed, from which the activation barrier ΔE_b for diffusion can be obtained and diffusivities and conductivities at other temperatures can be extrapolated. We can also simulate site occupancies from MD trajectories at finite temperature. For instance, Li occupancy at different Wyckoff positions can be investigated through Li ion distribution analysis and Li−Li radial distribution function (RDF) analysis. MD simulations, especially AIMD where bond formation and breaking can be reliably described, have also been used to model interfacial reactions.[146−149]

4. APPLICATIONS

In this section, we review applications of first-principles studies to elucidate the properties of various components of the rechargeable battery. We will note once again that due to the extensive body of computational studies on battery materials, we will focus on works where DFT computations have been used within a framework of other computational techniques and analysis. The vast majority of works in the literature that apply standard DFT calculations to compute battery voltages and migration barriers are not within the scope of this review. Also excluded are most works applying DFT computations in high-throughput screening for novel battery materials discovery. By its very nature, high-throughput screening typically utilizes relatively cheap, standard DFT computations.[150−156]

4.1. Electrodes

4.1.1. Transition Metal Oxides/Sulfides. Most transition metal oxides and sulfides that serve as electrodes in alkali-ion batteries adopt either a layered crystal structure or one that is derived from spinel (Figure 15). $LiCoO_2$, for example, forms the layered O3 crystal structure (using the notation of Delmas[26]), which consists of close-packed CoO_2 slabs that are interleaved by Li ions. The vacancies created within the Li layers upon Li extraction tend to remain disordered at most Li concentrations, thereby forming a solid solution with significant configurational entropy. Interactions among Li-ions can, however, lead to Li vacancy ordered phases at stoichiometric compositions.[17] Predicting these phenomena at finite temperature requires a statistical mechanics approach as described in section 3.2.1.

Early applications of first-principles statistical mechanics approaches to study the thermodynamic and kinetic properties of intercalation compounds focused on Li_xCoO_2.[51,157,158] A notable result of these studies was the predicted stability of a staged phase at low Li concentrations, referred to as H1−3.[27] The prediction of H1−3 predated experimental characterization of the phase, which required advances in in-situ experimental techniques to observe phase evolution in Li_xCoO_2 at high states of charge.[28] First-principles statistical mechanics approaches have since been applied to a wide variety of other transition metal oxides and sulfides. These include O3 Li_xNiO_2[159] and $Li_x(Ni_{0.5}Mn_{0.5})O_2$,[160] O2 Li_xCoO_2,[161] O1 and spinel forms of Li_xTiS_2,[48,162] spinel $Li_xTi_2O_4$,[163,164] and $Li_x(Mn_yNi_{1-y})_2O_4$[165,166] as well as Li_xTiO_2 in more complex crystal structures such as bronze B and anatase.[123,167] Similar investigations have been performed on Na, K, and Mg containing transition metal oxides such as O2/P2−Na_xCoO_2,[168,169] O3/P3−Na_xCoO_2,[170] O3/P3−K_xCoO_2,[171] Mg_xTiS_2,[172] and spinel $Mg_xCr_2O_4$.[173] The approach has become

https://dx.doi.org/10.1021/acs.chemrev.9b00601
Chem. Rev. 2020, 120, 6977−7019

increasingly automated, enabling high-throughput studies of multiple electrode chemistries simultaneously, as was done in a recent investigation of the dependence of the voltage profile of the spinel crystal structure on host and guest ion chemistry.[174]

While the transition metal sulfide electrodes of the first Li-ion batteries of the 1970s[1] are no longer competitive due to their low average voltage, they do serve as useful model systems to obtain a deeper understanding of intercalation thermodynamics and kinetics. Transition metal sulfides such as TiS_2 have itinerant valence electrons and therefore do not exhibit the additional complexities that arise from localized electronic states, such as charge ordering, Jahn−Teller distortions, and complex magnetic orderings,[180] which are common to many transition metal oxides. Common approximations to DFT (i.e., LDA and GGA) also tend to be more reliable for compounds with itinerant valence electrons. Figure 16 compares the calculated voltage

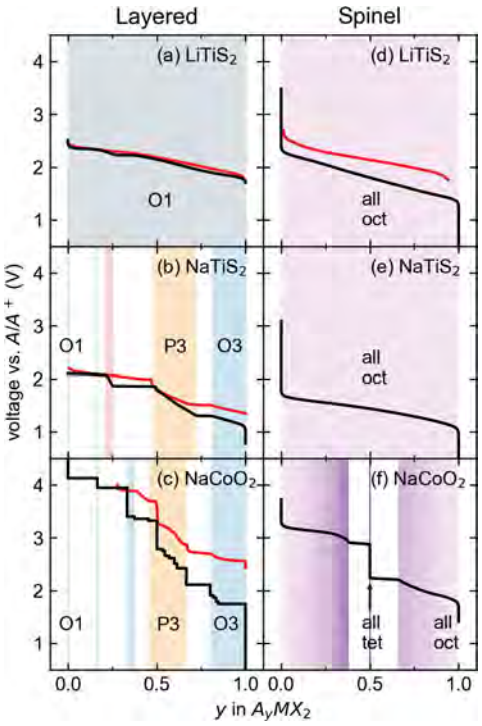

Figure 16. A comparison of calculated voltage profiles for (a−c) layered[48,170,175] and (b−d) spinel[174] A_xTiS_2 (A = Li, Na) and Na_xCoO_2. Experimentally measured voltage curves (Li_xTiS_2,[176] Na_xTiS_2,[177] Na_xCoO_2,[178] Li_xTiS_2[179]) are shown in red. Adapted from ref 90. Copyright 2019 Royal Society of Chemistry.

curves for layered and spinel forms of TiS_2 when intercalated by Li and Na. Parts a, b, and d of Figure 16 compare calculated voltage curves to experimentally measured voltage curves (shown in red).[90] In all cases, the qualitative agreement between calculated and experimental voltage curves is very good. Even the quantitative agreement is good. For comparison, Figure 16c shows the experimental and calculated voltage curves for Na_xCoO_2, the latter calculated with DFT without a Hubbard U correction.[170] Although the shapes of the two curves are very similar, there is, nevertheless, a systematic under prediction. This illustrates a well-known shortcoming of DFT calculations that neglect a Hubbard U correction when applied to transition metal oxides. Generally, a Hubbard U correction to DFT or a hybrid functional approach is necessary to accurately predict voltage curves, phase stability, and ordering tendencies in transition metal oxides.[99,103] There are exceptions, though, with A_xCoO_2 (A being Li or Na) being one of them. The use of a Hubbard U correction tends to decrease the qualitative accuracy of phase stability and voltage profile predictions for A_xCoO_2.[169] For example, Li_xCoO_2 undergoes a metal−insulator transition upon the removal of Li, becoming a metallic phase for $x < 0.75$, where electrons are delocalized and itinerant. Delocalized states are not well described with a Hubbard U correction.

A closer inspection of the predicted electrochemical and structural properties of Na_xTiS_2 reveal much about the physics of layered Na intercalation compounds in general (Figure 17).[175] Consistent with experimental observations, Figure 17

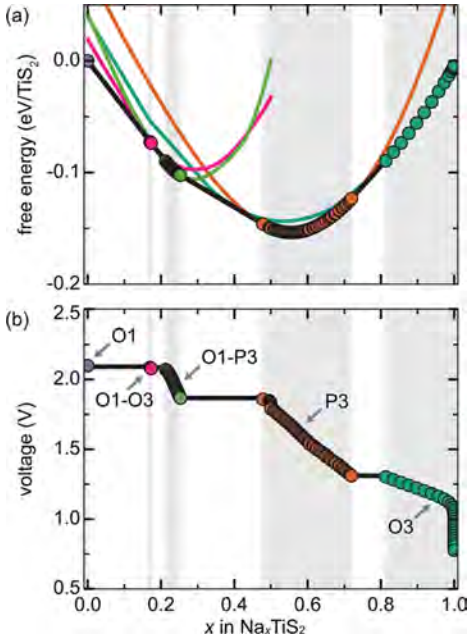

Figure 17. Calculated free energy curves (a) for different host structures and the resultant voltage profile (b) for Na_xTiS_2. Na_xTiS_2 undergoes a series of structural phase transformations involving the gliding of TiS_2 slabs relative to each other. Na_xTiS_2 prefers the O3 host at high Na concentrations but transforms to the P3 host and staged O1−P3 hosts at intermediate and low Na concentrations. Adapted from ref 175. Copyright 2016 American Chemical Society.

shows that Na_xTiS_2 is predicted to undergo a series of stacking sequence changes as a function of Na concentration, transforming from an O3 stacking at high concentrations to a P3 structure upon the partial removal of Na. At even lower Na concentrations, hybrid host structures such as O1−P3 and O1−O3 become favored. The hybrid O1−P3 and O1−O3 phases are staged with Na partially occupying alternating layers that have local P3 or O3 stacking, while the remaining layers having local O1 stacking are empty. Each host structure is described with a separate free energy curve in Figure 17a as they each have a distinct symmetry. A separate cluster expansion was constructed for each host structure, which was then subjected to Monte Carlo simulations to generate the data necessary to calculate a free energy curve using free energy integration techniques[175] as described in section 3.2.1. The transformation from O3 to P3 is observed experimentally, and while there is no direct structural evidence for the O1−P3 host at high states of charge (low Na concentrations), there is evidence for staging.[181,182]

The P3 host of Na_xTiS_2, which is stable at intermediate Na concentrations, consists of a TiS_2 stacking sequence that

https://dx.doi.org/10.1021/acs.chemrev.9b00601
Chem. Rev. 2020, 120, 6977−7019

produces trigonal prismatic sites within the intercalation layers (Figure 15b). While the octahedrally coordinated Na sites of the O3 structure (Figure 15a) form triangular lattices as illustrated in Figure 18a, the trigonal prismatic Na sites of P3 form a honeycomb network with twice as many sites per TiS_2 formula unit (Figure 18b). P3 only appears when intercalating large guest cations such as Na and is stabilized relative to O3 at intermediate concentrations because the additional sites of a honeycomb network allow for a larger separation between neighboring Na ions.[183] This is illustrated in parts a and b of Figure 18, which show common low energy orderings on the triangular lattice of O3 and the honeycomb network of P3 at $x = {}^1/_2$.[90,175,183]

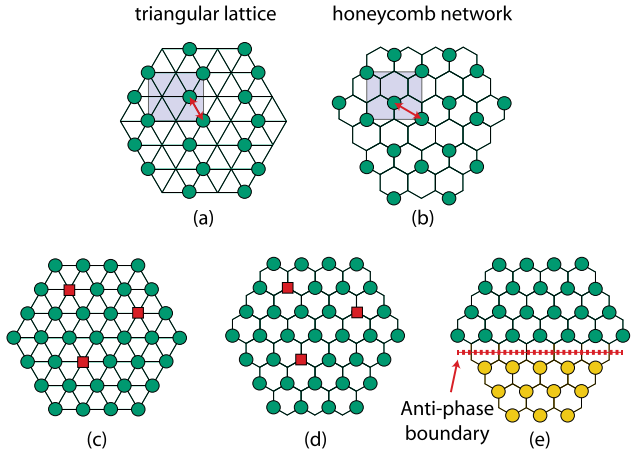

Figure 18. Guest ion octahedral sites of the O3 and O1 hosts form two-dimensional triangular lattices, while those of the prismatic sites of P3 form honeycomb networks. (a) Nearest neighbor interactions (red arrow) at $x = {}^1/_2$ are unavoidable on the triangular lattice. (b) The additional sites offered by the honeycomb network allow cations to separate more uniformly with an increased distance between neighboring cations at $x = {}^1/_2$. (c) Vacancies tend to distribute uniformly over the sites of a triangular lattice. (d) Vacancies could also distribute uniformly over the sites of a honeycomb network, however, it is more favorable for vacancies to coalesce at anti phase boundaries (e) on a honeycomb network.[90,175]

The honeycomb network of Na sites in P3 leads to interesting ordering phenomena that are absent within the O3 host structure.[170,175] The vacancies on the triangular lattices of O3 tend to distribute uniformly as illustrated in Figure 18c. A similar distribution is possible on a honeycomb network as illustrated in Figure 18d, however, the extra flexibility offered by the additional sites on a honeycomb network allows for other ways of distributing vacancies that are energetically more favorable. Instead of distributing uniformly, the vacancies can coalesce at antiphase boundaries (APBs) between two perfectly ordered domains that differ only by the sublattice that is occupied, as illustrated in Figure 18e.[175] The tendency of vacancies to coalesce at APBs leads to very different types of Na disorder than is present in O3 as illustrated by the Monte Carlo snap shots of a particular Na-layer of P3 Na_xTiS_2 (Figure 19).[175] A decrease in the Na concentration is accommodated by an increase in the total antiphase boundary length. At high Na concentrations, the total APB-length remains small and the Na ions organize into large perfectly ordered domains. The domains adopt a triangular shape because there are three symmetrically equivalent orientations of the preferred APB of Figure 18e. Figure 19 shows that as the Na concentration decreases, the accompanying increase in total APB length results in a reduction of the domain size and a general increase in the degree of disorder.

The higher degree of covalency in sulfides leads to weaker in-plane electrostatic interactions between the Na ions and hence to less strong ordering tendencies than is present in the more ionic oxides.[183] This becomes evident when comparing the ordering preferences and voltage profile of Na_xTiS_2 to that of Na_xCoO_2. The more ionic Na_xCoO_2 has very strong ordering preferences as is revealed by the large voltage step at $x = {}^1/_2$ in Figure 16c. The step at $x = {}^1/_2$ is due to the stability of the ordered phase of Figure 18b, in which the Na ions spread as far apart from each other as possible. The preference for this particular ordering is so strong in Na_xCoO_2 that the compound tries to maintain the same ordering locally, even at concentrations that deviate from $x = {}^1/_2$. As in Na_xTiS_2, this is again predicted to occur with antiphase boundaries.[170] However, the APBs do not separate domains with $x = 1$ as illustrated in Figure 20a. Instead they separate perfectly ordered domains having the $x = {}^1/_2$ ordering as illustrated in Figure 20b,c.[90,170] The predictions that antiphase boundaries such as those of Figure 20 accommodate off-stoichiometry in P3 host structures have yet to be confirmed experimentally. However,

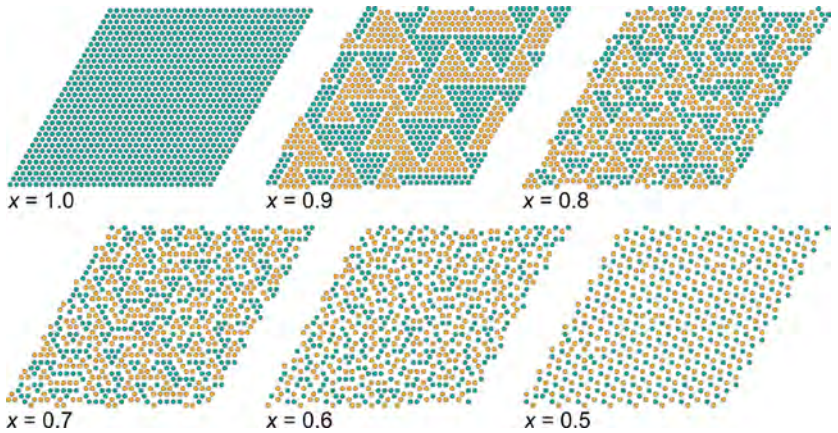

Figure 19. Snapshots of one Na layer from grand canonical Monte Carlo simulations for P3 Na_xTiS_2 at 300 K. The two different sets of sites on the honeycomb lattice are marked in green and yellow. As is revealed by the free energy curves of Figure 17a, the P3 host is metastable above $x = 0.7$. Adapted from ref 175. Copyright 2016 American Chemical Society.

https://dx.doi.org/10.1021/acs.chemrev.9b00601
Chem. Rev. 2020, 120, 6977−7019

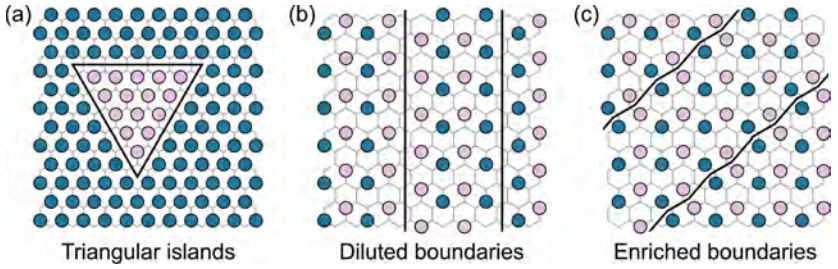

Figure 20. First-principles calculations for Na_xTiS_2 and Na_xCoO_2 predict that vacancies and off-stoichiometry can be accommodated on the honeycomb network of prismatic sites of P3 with antiphase boundaries, which separate two different translational variants of a particular ordered phase. (a) At high Na concentrations, vacancies coalesce at antiphase boundaries separating perfectly ordered $x = 1$ domains. (b,c) Close to $x = {}^1/_2$, antiphase boundaries separate domains having a stable $x = {}^1/_2$ ordering. Adapted from ref 90. Copyright 2019 the Royal Society of Chemistry.

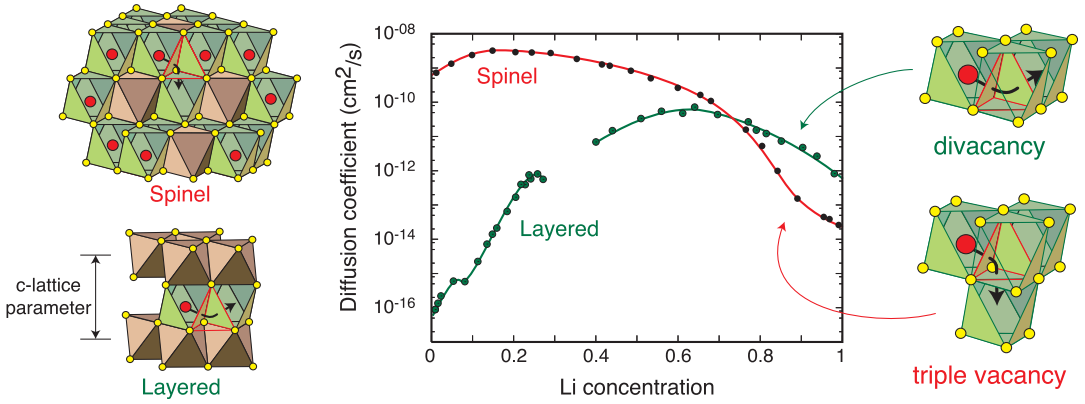

Figure 21. Chemical diffusion coefficient of Li in an intercalation compound often has a strong dependence on Li concentration and crystal structure. Adapted from ref 189. Copyright 2013 American Chemical Society.

the predicted stability of antiphase boundaries leads to a large family of complex ordered phases in Na_xCoO_2 that are responsible for the small steps in the calculated voltage profile that are also evident in the experimental voltage profile.[90,170]

Many important electrode chemistries for Na-ion batteries adopt the P2 crystal structure (Figure 15c), which, similar to P3, also has trigonal prismatic sites that can be occupied by Na between transition metal oxide sheets. A notable difference between P2 and P3, though, is that the two trigonal prismatic sites of P2 per formula unit are not equivalent by symmetry. The Na1 site of Figure 15c shares faces with transition metal cations above and below, while the Na2 sites do not share faces with transition metal cations. Although the nonface-sharing Na2 sites are energetically preferred, strong in-plane electrostatic repulsions still lead to occupancy of the face sharing Na1 sites. This competition results in complex ordering patterns that have proven challenging to model and characterize experimentally[168,169,184]

Most experimental studies of cathode materials focus on multitransition metal (TM) systems because transition metal mixing tends to suppress alkali-ion ordering at stoichiometric compositions.[185,186] Alkali vacancy ordering often leads to a significant reduction in the diffusion coefficient[51] and is therefore undesirable. In spite of its importance, detailed computational studies of mixed-TM oxides remain rare due to the complexity of coupling alkali vacancy disorder with binary or ternary transition metal disorder. Additional complexities arise with transition metals such as Fe, Ni, and Mn, which tend to exhibit localized oxidation states that can change with the alkali concentration. The many possible ways of arranging different oxidation states over transition metal sites constitutes an additional source of configurational entropy. A study by Zheng et al.[187] demonstrated that Co/Mn mixing in P2 $Na_xCo_{1-y}Mn_yO_2$ decreases the tendency for Na ordering. They also showed that different transition metals can substantially modify the site energy of the face-shared Na site of P2 and by combining AIMD simulations, NEB calculations, and percolation theory, established theoretical limits for the mixing of various TM in P2 Na_xCoO_2. Kubota et al.[178] studied Fe/Co ordering in O3 $NaFe_{1/2}Co_{1/2}O_2$ with Monte Carlo simulations and found no evidence for Fe/Co ordering at 300 K, consistent with neutron diffraction data.[188] Lee and Persson[165] studied the effect of transition metal disorder on the electrochemical properties of high voltage spinel $Li_xNi_{0.5}Mn_{1.5}O_4$ with a coupled cluster expansion and Monte Carlo simulations. This study demonstrated a strong coupling between Li vacancy ordering tendencies and the degree of transition metal ordering. A similar study was performed by Hao et al. for $Li_x(Mn_yNi_{1-y})_2O_4$.[166]

First-principles statistical mechanics approaches have also been applied to study ion transport in transition metal oxides and sulfides. The combination of first-principles cluster expansion Hamiltonians with kinetic Monte Carlo simulations have revealed that the Li diffusion coefficients of transition metal oxides and sulfides are very sensitive to the Li concentration and the degree of cation ordering.[48,51,162,164,189] Figure 21, for example, shows the calculated chemical diffusion coefficients of the layered and spinel forms of Li_xTiS_2 as a function of Li concentration.[48,162,189] Not only do the calculated diffusion coefficients vary by several orders of magnitude with concentration, but their qualitative shapes are very different, showing that crystal structure plays a crucial role in determining

https://dx.doi.org/10.1021/acs.chemrev.9b00601
Chem. Rev. 2020, 120, 6977−7019

the concentration dependence of diffusion coefficients of intercalation compounds. The concentration dependence of the Li diffusion coefficient for the layered form of Li_xTiS_2 is typical of that of layered compounds in general.[17,51] The spinel form of Li_xTiS_2 is a useful model system with which to understand diffusion in three-dimensional close-packed anion systems, such as disordered rock salts. This is because the transition metal arrangement in spinel leads to a three-dimensional network of octahedral sites that are preferentially occupied by Li in Li_xTiS_2.[162]

The strong dependence of Li diffusion coefficients on composition and cation arrangement in transition metal oxides and sulfides arises from crystallographic constraints imposed by the close-packed nature of their anion sublattices.[189] Cation hops between neighboring octahedral sites of a close-packed anion sublattice pass through an intermediate tetrahedral site, as these paths are sterically less constricted than a more direct path.[51] An important topological feature of the intermediate tetrahedral sites is that they are coordinated by more than just the end states of the hop. This property makes the overall migration barrier of the hop very sensitive to the occupancy of the neighboring sites that do not participate in the hop. The relationship of the intermediate tetrahedral sites to neighboring octahedral sites is schematically illustrated for the layered O3 host and for a spinel host in Figure 22. The most favorable hop

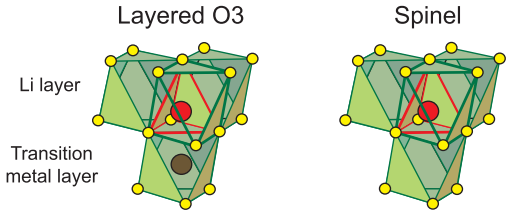

Figure 22. Li hops between octahedral sites of host structures that have a close-packed anion sublattice often pass through an intermediate tetrahedral site. The tetrahedral sites share faces with four nearest neighbor octahedral sites. In the layered O3 crystal structure, one of these octahedral sites is occupied by a transition metal.

environments for hops between octahedral sites that pass through a tetrahedral site are those consisting of vacancy clusters. In the layered compounds, such as Li_xCoO_2 and Li_xTiS_2, hops are predominantly mediated by divacancies,[48,51,189] while in three-dimensional crystals such as spinel Li_xTiS_2 (where Li occupies octahedral sites), diffusion is mediated by triple vacancies.[162,164]

The reason that vacancy clusters mediate Li diffusion in close-packed anion sublattices becomes clear upon inspection of Figure 23, which shows calculated migration barriers as a function of the vacancy cluster size in spinel Li_xTiS_2.[162] The tetrahedral sites of spinel are coordinated by four octahedral sites that could be occupied by Li. A migrating Li ion hops into a triple vacancy if three of the adjacent octahedral sites are vacant (Figure 23a). When the migrating Li passes through the intermediate tetrahedral site, it will be surrounded by four empty octahedral sites, a configuration that is low in energy as there are no replusive interactions with neighboring Li ions. In contrast, when a Li ion hops into a divacancy, as in Figure 23b, it will experience increased electrostatic repulsion when it passes through the tetrahedral site due to the presence of a neighboring Li ion in an adjacent octahedral site. The barrier for such a hop is higher than for a triple vacancy hop. The barrier becomes even

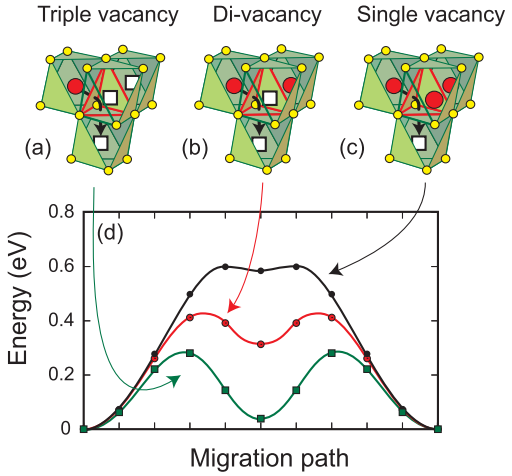

Figure 23. Migration barrier along hops connecting two octahedral sites in spinel Li_xTiS_2 are very sensitive to the number of vacancies neighboring the intermediate tetrahedral site. The barriers decrease with the number of vacancies, with hops into a triple vacancy having the lowest barrier. Adapted from ref 162. Copyright 2011 American Physical Society.

higher in a single vacancy hop (Figure 23c) because the migrating Li ion then has two nearest neighbor octahedral Li ions when it occupies the intermediate tetrahedral site.

Kinetic Monte Carlo simulations have shown that the majority of hops in layered and three-dimensional structures such as spinel are mediated by vacancy clusters: divacancies in the layered materials[48,51] and triple vacancies in the spinel.[162] They also showed that diffusion mediated by vacancy clusters is highly correlated, especially at high Li concentrations where the concentration of vacancy clusters is very low. Figure 24, for

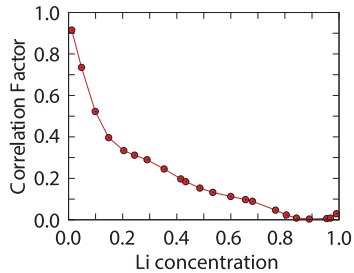

Figure 24. Calculated correlation factor for Li diffusion in spinel Li_xTiS_2. The correlation factor measures the degree with which successive hops are correlated. Uncorrelated hops lead to a correlation factor of 1. Li diffusion in spinel Li_xTiS_2 is mediated by triple vacancies, which lead to highly correlated diffusion at high concentrations where triple vacancies become very dilute. Adapted from ref 162. Copyright 2011 American Physical Society.

example, shows the calculated correlation factor f (eq 30) for spinel Li_xTiS_2, where Li diffusion is predominantly mediated by triple vacancies.[162] The correlation factor is close to 1 at low Li concentrations, where the number of Li ions in the crystal is sufficiently low that each Li essentially performs a random walk without interacting much with other Li ions. The correlation factor decreases, however, with increasing Li concentration, becoming especially low at high Li concentrations, where diffusion is mediated by isolated di- and triple vacancies.[162] The isolated vacancy clusters are very inefficient at mediating long-

https://dx.doi.org/10.1021/acs.chemrev.9b00601
Chem. Rev. 2020, 120, 6977−7019

range Li-ion transport, leading to a Li correlation factor that is more than a factor of 100 less than that of a random walker.

The dependence of Li transport on vacancy clusters is responsible for a drop off in the diffusion coefficient with increasing Li concentrations. In a random solid solution, the divacancy and triple vacancy concentrations decrease as $(1-x)^2$ and $(1-x)^3$, respectively. Hence, the number of diffusion mediating defects diminish rapidly as the Li concentration approaches $x = 1$. In real intercalation compounds, it decreases even more rapidly due to thermodynamic nonidealities arising from vacancy−vacancy repulsions as the vacancy concentration becomes dilute. As is clear from Figure 21, the diffusion coefficient decreases more rapidly in the spinel form of Li_xTiS_2, with its three-dimensional interstitial network and its reliance on triple vacancies, than in the layered form of Li_xTiS_2, where diffusion is mediated by divacancies.

Figure 21 shows that the diffusion coefficients of layered intercalation compounds also decrease as the Li concentration approaches $x = 0$. The decrease again has a crystallographic origin, arising from the contraction of the *c*-lattice parameter at low Li concentrations. A reduction in the distance between transition metal oxide (sulfide) slabs penalizes the activated state (intermediate tetrahedral site) more than the initial states (octahedra) of the hop. This leads to an increase in the migration barriers, ΔE_b, of Li hops at low Li concentrations.[48,51]

Basic insights about diffusion mechanisms that are derived from first-principles statistical mechanics studies can be used to rationally design new electrode materials. This was recently demonstrated by Lee et al.[190] in the development of disordered rock salt cathodes that exhibit exceptionally high rate capabilities. Disordered rock salts are similar to layered O3 and spinel host structures in that they also consist of a close-packed oxygen sublattice, differing only in that the Li and transition metal cations are disordered over the octahedral sites of the oxygen sublattice. Li diffusion in a disordered rock salt is therefore also expected to proceed through intermediate tetrahedral sites.[190,191] As a result, migration barriers will be very sensitive to the occupancy of the octahedral sites that coordinate the tetrahedral site of a hop. Similar to the hop barriers in spinel Li_xTiS_2 (Figure 23),[162,189] a hopping Li ion will experience a low migration barrier when it passes through a tetrahedral site that is coordinated by zero transition metal cations,[191] referred to as 0-TM by Lee et al.[190] as shown in Figure 25b. Any tetrahedral site coordinated by one (1-TM, Figure 25c) or two (2-TM, Figure 25d) transition metal cations will pose a high barrier for Li hops and impede long-range Li diffusion.[191] Cation arrangements that lead to interconnected networks of 0-TM tetrahedral sites are therefore desirable for fast Li diffusion. Lee et al.[190] and Urban et al.[191] showed that it is possible to realize percolating networks of 0-TM tetrahedral sites in disordered rock salts that have an excess of ~10% lithium (Figure 26). This is consistent with the high rates and capacities observed in $Li_{1.211}Mo_{0.467}Cr_{0.3}O_2$ (265.6 mAh g^{-1}).[190] Subsequent work extended these strategies by investigating fluorinated rock salt oxides, utilizing cluster expansions and Monte Carlo simulations to establish that fluorination is only possible in Li-rich regions and that cation disorder may help create such local environments.[192] The work of Kitchaev et al.,[193] which also relied on cluster expansions and Monte Carlo simulations, led to the identification of the optimal disordered rock salt compositions in the Li−Mn−V−O−F space that maximize capacity.

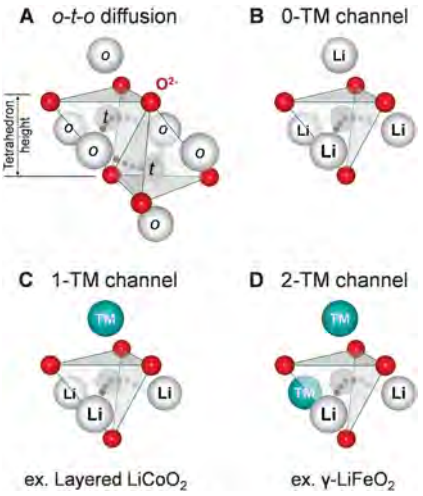

Figure 25. Possible environments for Li hops in rocksalt-like Li-TM oxides. (A) Two tetrahedral paths connect each pair of neighboring octahedral sites. The activated state can share faces with (B) no octahedral transition metals (0-TM channel), (C) one transition metal (1-TM channel), or (D) two transition metals (2-TM channel). Adapted from ref 190. Copyright 2014 American Association for the Advancement of Science.

4.1.2. Polyanion Oxides. While many promising cathodes for Li and Na-ion batteries are transition metal oxides, other more complex polyanionic compounds have also shown promise as electrode materials. A particularly interesting polyanionic compound that has received considerable attention from the research community is Li_xFePO_4[20,59] having the olivine crystal structure. It exhibits a variety of peculiar properties that make it an unlikely candidate for Li-ion batteries, including (i) a crystal structure that only allows for one-dimensional diffusion,[79] (ii) a two-phase reaction that is accompanied by a large change in lattice parameters,[72] and (iii) a low electronic conductivity.[194] In spite of these properties, Li_xFePO_4 has proven to be a remarkable cathode material for high-rate capability Li-ion batteries.[59]

Li_xFePO_4 exhibits localized oxidation states on the Fe sites at intermediate Li concentrations *x*. These states have polaronic character.[194,195] Standard semilocal functionals, such as LDA and GGA, fail to accurately describe the localized electronic states in Li_xFePO_4 and predict that the compound should form a simple solid solution as a function of *x*,[99] a result that is in stark contrast to experimental observations.[59] It is only with a Hubbard U correction that a miscibility gap is predicted at intermediate Li concentrations and that localized Fe^{2+} and Fe^{3+} oxidation states are stabilized.[99] Electron localization in Li_xFePO_4 not only affects the enthalpy of mixing but also plays an important role in determining the entropy of the compound at finite temperature. A statistical mechanics study by Zhou et al.[111] showed that an explicit treatment of the configurational entropy arising from Fe^{2+}-Fe^{3+} disorder at intermediate Li concentrations is essential to reproduce the correct topology of the temperature versus composition phase diagram of Li_xFePO_4. Figure 27[111] compares experimentally measured phase diagrams (Figure 27a) to a phase diagram calculated by accounting for both Li vacancy disorder and localized electronic degrees of freedom (Figure 27b) and a phase diagram calculated by only considered Li vacancy disorder (Figure 27c). The experimentally measured phase diagrams (Figure 27a) show the existence of a monotectoid. The

https://dx.doi.org/10.1021/acs.chemrev.9b00601
Chem. Rev. 2020, 120, 6977−7019

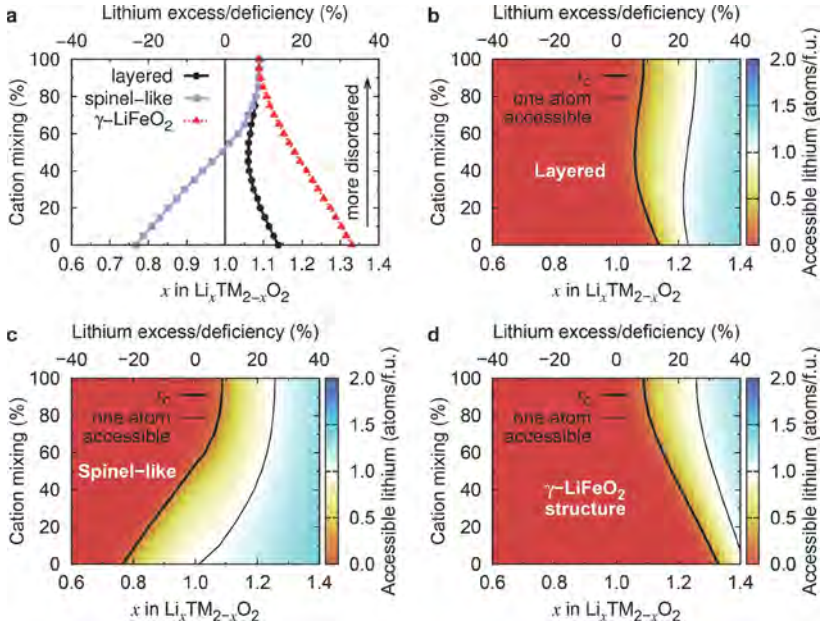

Figure 26. (a) Critical lithium concentrations for 0-TM percolation in different rock salt-type Li-TM oxides. (b–d) Accessible lithium atoms per formula unit as a function of the overall lithium concentration and the degree of cation mixing in (b) layered, (c) spinel-like, and (d) γ-$LiFeO_2$. Thick and thin lines indicate concentrations of 0-TM percolation and one lithium atom becoming accessible, respectively. Adapted from ref 191. Copyright 2014 Wiley-VCH.

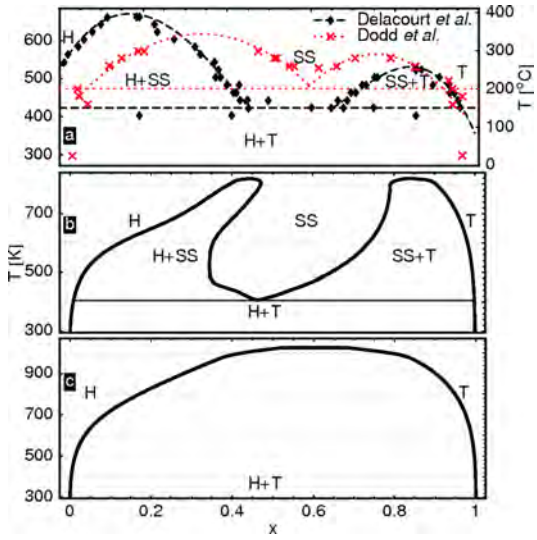

Figure 27. Li_xFePO_4 phase diagram. (a) Experimental phase boundary data from Delacourt et al.[197] and Dodd et al.[198] (b) Calculated phase diagram with both Li and electron degrees of freedom and (c) with Li degrees of freedom only. Adapted from ref 111. Copyright 2006 American Physical Society.

monotectoid is also predicted in the phase diagram of Figure 27b, that was calculated by explicitly treating both Li vacancy and Fe^{2+}–Fe^{3+} configurational disorder with a cluster expansion and Monte Carlo simulations.[111] The monotectoid is absent, however, when the discrete electronic degrees of freedom on the Fe sites are neglected, with a simple miscibility gap emerging for a model that is restricted to only Li vacancy disorder (Figure 27c). Cluster expansion models for Li_xFePO_4 continue to be refined and have led to further insights about the thermodynamic and kinetic properties of this compound.[196]

The voltage curve[20] (Figure 3a) and phase diagram of Li_xFePO_4 (Figure 27a)[197] indicate that Li insertion and removal from the compound should proceed by means of a two-phase reaction at room temperature. A first-principles statistical mechanics study by Malik et al.,[85] however, predicted a very shallow free energy inside the two-phase region, leading the authors to suggest a kinetic pathway of Li insertion and extraction that bypasses a two-phase coexistence and instead proceeds through a solid solution phase. The electrode is then able to avoid a nucleation and growth mechanism, which would be accompanied by large coherency strains.[71,78,199]

Whether two-phase coexistence occurs in particles of Li_xFePO_4 or whether (de)lithiation of Li_xFePO_4 proceeds through a solid solution phase depend sensitively on a variety of factors. Thermodynamic arguments show that a two-phase coexistence can be suppressed if the elastic strain energy and the interfacial energy of a coherent two-phase coexistence exceeds that of the free energy penalty of forming a solid solution. A systematic study by Abdellahi et al.[199] showed how particle size and shape affects the stability of a two-phase coexistence relative to a solid solution. The rate of Li insertion and extraction also plays an important role in determining whether the compound transforms through a two-phase reaction or follows a path through a solid solution. This was systematically investigated with kinetic models by Bai et al.[84] Several in situ experimental studies have provided evidence for the single-phase reaction path.[200]

Other polyanion cathodes, such as Li_2FeSiO_4 and Li_xVOPO_4, have also received much attention due to the promise that they may undergo multielectron redox processes and thereby enable very high capacities. Saracibar et al.[201] and Eames et al.,[202] for example, investigated the relative stability of several Li_2FeSiO_4 polymorphs and found that although all polymorphs are close in energy when completely lithiated, the 3D hosts are more stable than the layered structures upon Li removal. The large changes in relative stability between different polymorphs upon Li removal makes these compounds highly susceptible to degradation processes and irreversible phase transformations

https://dx.doi.org/10.1021/acs.chemrev.9b00601
Chem. Rev. 2020, 120, 6977–7019

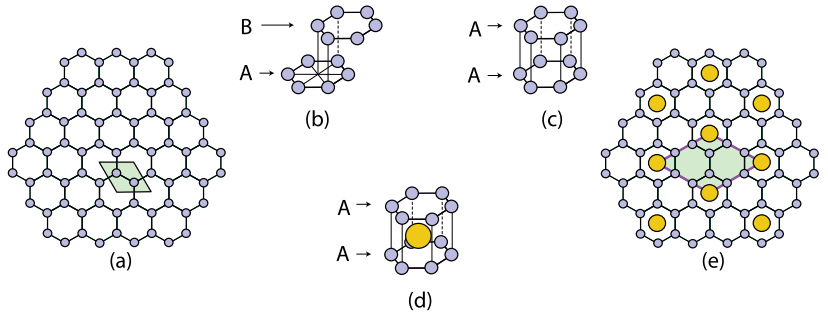

Figure 28. (a) Graphite is made up of two-dimensional graphene sheets. Carbon are the light-blue atoms and reside on a honeycomb net. The aqua-green diamond represents the two-dimensional primitive unit cell of the honeycomb network. The graphene sheets can adopt different stacking sequences. In pure graphite, they adopt an ABAB stacking sequence (b), while when intercalated by Li they adopt an AA stacking sequence (c). (d) Guest ions such as Li (yellow circle) reside above and below the empty hexagons of the honeycomb networks of AA stacked graphene sheets. (e) Strong nearest neighbor Li−Li repulsion leads to a $\sqrt{3}a \times \sqrt{3}a$ supercell ordering between graphene sheets that allows for the highest density of Li while avoiding nearest neighbor Li−Li pairs.

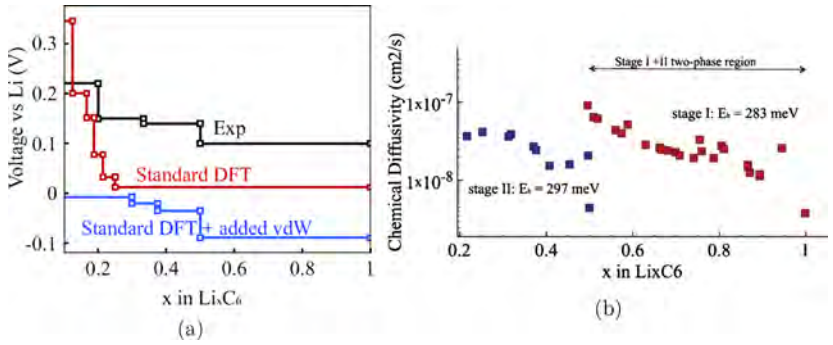

Figure 29. (a) Voltage profile for the Li-graphite system obtained by standard DFT data (red line), DFT data corrected for vdW interactions (blue line),[205] compared to experiments (black curve).[209] (b) Calculated Li chemical diffusivity in stage II (blue squares) and stage I (red circles) phases in the Li−graphite system.

at high states of charge. Similarly, Lin et al.[203,204] carried out in-depth DFT and experimental studies of the polymorphs of A_xVOPO_4, a family of highly promising multielectron polyanion cathodes for both Li-ion and Na-ion battery chemistry. The authors elucidated the intermediate phases in the intercalation of two Li into ε-$VOPO_4$ using both DFT calculations and operando PDF techniques. Furthermore, the authors found that the β and ε polymorphs have more favorable Li diffusion than the $\alpha - I$ polymorph, while the latter was found to have more favorable diffusion for Na due to its layered structure that can accommodate the larger Na ion.

4.1.3. Graphite and Alloy Electrodes. There are only a limited number of transition metal oxides (e.g., TiO_2) that are suitable for the anode of a Li-ion battery because most have voltages (relative to metallic Li) that are too high. Instead, graphite intercalation compounds and elements including Si, Sn, and Sb, which undergo alloying reactions with Li, are more suited for the anodes of Li-ion batteries. All these disparate materials classes have been studied with a wide variety of first-principles modeling tools.

Graphite serves as the anode in the majority of commercial Li-ion batteries. It has a layered crystal structure made of graphene sheets (Figure 28a). Similar to layered transition metal oxides and sulfides, the two-dimensional graphene sheets can adopt different stacking sequences depending on the concentration of the intercalated guest ions. The carbon of a particular graphene sheet occupy sites of a honeycomb network. In pure graphite, the graphene sheets prefer an ABAB stacking sequence whereby a carbon atom of one graphene sheet resides above the center of a hexagon of carbon of an adjacent graphene sheet (Figure 28b). The stacking sequence between adjacent layers changes to an AA sequence, however, upon the insertion of guest cations such as Li or K between the pair of layers (Figure 28c). The guest cations then reside above and below the carbon hexagons of each sheet (Figure 28).

The thermodynamic and kinetic properties of the Li_xC_6 graphite intercalation compound were investigated with first-principles statistical mechanics methods by Persson et al.[205,206] Li intercalation into graphite occurs in stages, where the stage number n corresponds to $n - 1$ empty layers between each Li-filled layer. The graphene sheets adjacent to the filled layers adopt an AA stacking sequence, while those adjacent to empty layers tend to adopt an AB stacking sequence as in pure graphite. The interactions between adjacent graphene sheets across an empty intercalation layer are very weak and are dominated by van der Waals forces. This poses a challenge to conventional DFT approaches as they fail to describe van der Waals interactions. It is, therefore, essential to include van der Waals corrections as part of the DFT calculations. Figure 29a, for example, shows that a better qualitative agreement is obtained (apart from a systematic shift) between calculated and experimentally measured voltage curves when van der Waals corrections are included.[205]

A cluster expansion Hamiltonian constructed for Li_xC_6 based on van der Waals corrected DFT formation energies showed that in-plane Li−Li interactions are quite strong.[205] They are sufficiently strong to prevent nearest-neighbor Li−Li pairs, thereby limiting the maximum Li concentration to LiC_6. At this

https://dx.doi.org/10.1021/acs.chemrev.9b00601
Chem. Rev. 2020, 120, 6977−7019

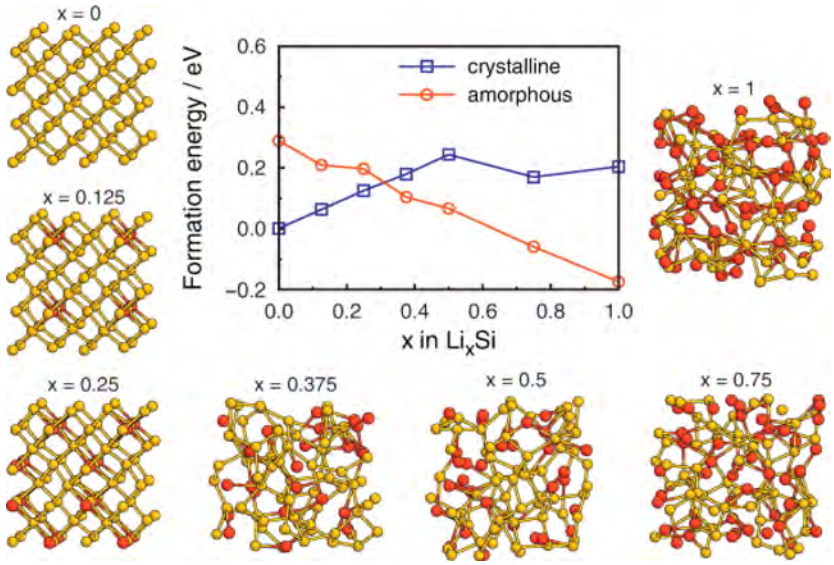

Figure 30. 0 K formation energies of crystalline and amorphous Li_xSi phases and stable structure at each Li concentration. Adapted from ref 218. Copyright 2011 Elsevier Ltd.

composition, the Li ions can order in a $\sqrt{3}a \times \sqrt{3}a$ supercell within the two-dimensional intercalation layers (Figure 28e). This ordering maximizes the Li concentration without introducing nearest neighbor Li−Li pairs. The Li diffusion kinetics within the graphite host structure was also investigated by Persson et al.[205,206] Migration barriers as calculated with the NEB method were combined with a cluster expansion Hamiltonian in kinetic Monte Carlo simulations to predict the Li diffusion coefficient as a function of the Li concentration. The calculated diffusion coefficient shown in Figure 29b ranges around $\sim 10^{-7}$ cm^2 s^{-1} and is in reasonable agreement with careful experimental measurements of 4.4×10^{-6} cm^2 s^{-1}.[206]

The changes in stacking sequence between graphene sheets that occur with variations in the Li concentration of graphite means that Li insertion/removal from the host not only requires diffusion but also the gliding of adjacent graphene sheets relative to each other. These gliding transitions may also be mediated by a dislocation mechanism as proposed for Li_xCoO_2 by Gabrisch et al.[89] and as described in section 2.3. Models based on the phase field approach have been developed to study the kinetics of Li insertion and staging phenomena in graphite intercalation compounds.[207,208] These models, however, do not yet include the chemomechanics accompanying the stacking sequence changes from AA to AB upon deintercalation of a filled layer.

Alloying reactions within anodes are especially challenging to model from first-principles due to the crystallographic complexity of the intermetallic phases that form and the possibility that the anode becomes amorphous upon lithiation.[210] Alloying reactions are often also accompanied by very large volume changes, which pose challenges to meso and continuum scale models. Silicon, for example, is an alternative to graphite as an anode material for Li-ion batteries and offers very high capacities when fully converted to $Li_{15}Si_4$. Other elements such as Sn and Sb can also serve as anodes in Li ion batteries and similar to Si form a rich variety of complex intermetallic compounds when alloyed with Li. In contrast to intercalation processes, the reaction products of an alloying reaction can adopt very different crystal structures from that of the original starting metal. One task, therefore, is to identify the crystal structures of the intermediate intermetallic compounds that are thermodynamically stable when an element such as Si, Sn, or Sb reacts with Li. One approach to predicting the crystal structure of intermetallic compounds is to use the cluster expansion infrastructure to enumerate large numbers of ordered phases obtained by systematically decorating the sites of simple parent crystal structures such as bcc, fcc, and hcp. Such an approach was performed for the Li−Sb system.[211,212] A drawback of the approach is that it is restricted to orderings on a limited set of parent crystal structures. Morris et al.[213−216] used an alternative approach based on the ab initio random structure searching (AIRSS) method to determine stable intermetallic compound crystal structures in the Li−Si, Li−Ge, Li−Sn, Li−Sb, and Li−P binary systems. Because the AIRSS approach is not restricted to a limited set of parent crystal structures it has a higher probability of discovering new and unexpected crystal structures.

The tendency of Si to amorphize and swell by more than a factor of 2 when electrochemically alloyed with Li makes molecular dynamics simulations a more suitable modeling approach than the cluster expansion method to predict the electrochemical and transport properties of Si anodes. Johari et al.,[217] for example, performed AIMD simulations to quantify the mobility of both Li and Si in a lithiated silicon anode. The diffusivity of Li was predicted to be 4 orders of magnitude larger than that of Si in the crystalline phase, with the gap narrowing in the amorphous phase to 2 orders of magnitude. The authors pointed out that the lack of Si mobility is the cause of the large stresses generated during lithiation and that the amorphous phase is helpful for stress relaxation. Jung and Han[218] investigated the lithiation-induced phase transitions by generating the atomic configurations for the amorphous phase from quenching AIMD simulations. It was inferred that amorphization occurs after the Li:Si ratio exceeds 0.3 from formation energy comparisons (Figure 30). This finding is in agreement with a ^7Li NMR study by Key et al.,[219] where new peaks emerge at 105 mV during the first discharge of crystalline Si with respect to Li/Li^+, corresponding to a Li:Si ratio of 0.26. These peaks imply a breaking of the crystalline Si structure. The large variety of local structure within amorphous phases makes the sampling of realistic environments especially challenging. Artrith et al.[220]

https://dx.doi.org/10.1021/acs.chemrev.9b00601
Chem. Rev. 2020, 120, 6977−7019

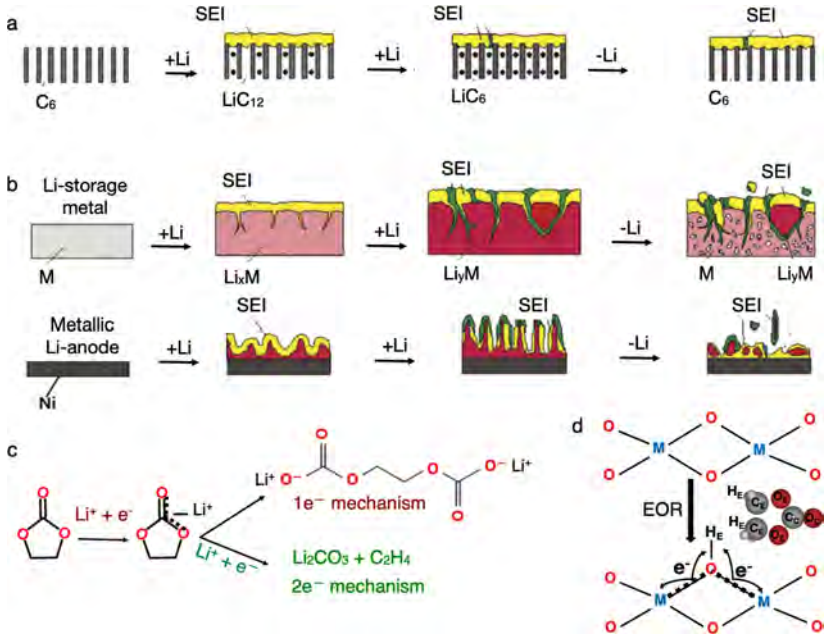

Figure 31. Schematic representation of dissimilarity in the characteristic feature of SEI formation and growth on the surfaces of (a) graphite and (b) metal (Li or Li-alloys). The SEI is stable on graphite electrode, however, after cycling crack appears due to the volume expansion and contraction, SEI mechanical failure is more for Li-storage-metals (such as Si or Sn) as anode compared to graphite due to larger volume change, and metallic lithium leads to new SEI formation in each cycle and surface morphology alters accordingly. Reproduced with permission from ref 232. Copyright 2015 The Electrochemical Society. (c) Schematic representation of two pathways for EC reduction at anode. Reproduced with permisison from ref 147. Copyright 2013 American Chemical Society. (d) Schematic representation of electrolyte reduction reaction (EOR), namely, electrolyte EC oxidation on the Li_xMO_2 (M = Mn, Co) cathode surface, while a proton and two electrons are transferred to the surface. M, O, and H denote metal, oxygen, and hydrogen, respectively. Labeling scheme and color code for ethylene carbonate are carbonyl oxygen, O_C, carbonyl carbon, C_C, ethylene coordinated oxygen, O_E, ethylene carbon, C_E, and ethylene hydrogen, H_E. Reproduced with permission from ref 233. Copyright 2018 American Chemical Society.

has overcome these challenges by introducing an efficient sampling method that combines a genetic algorithm and a coarse machine-learned interatomic potential trained on a smaller DFT data set. The amorphous structures generated with this approach generally have lower energies than heat-quenched MD simulations.

4.2. Electrolytes

The electrolyte is the medium through which ions are transported between the electrodes during battery operation. As such, this medium must have a high ionic conductivity (at least 0.1 mS/cm, with >1 mS/cm desired for high-rate applications) coupled with low electronic conductivity. Furthermore, the electrolyte is subject to both low and high extrema in alkali chemical potential, being in contact with both the cathode and anode at the same time. The nature of the electrified electrode/electrolyte interfaces, i.e., the existence of any reactions, the products formed, and the ionic transport across interface frequently dictate overall battery performance and has been the focus of major studies.[13,34]

By far, the most common type of electrolytes today are solutions of lithium salts (e.g., $LiPF_6$, $LiClO_4$, LiTFSI) in a mixture of liquid solvents such as 1:1 ethylene carbonate (EC):dimethylcarbonate (DMC). These liquid electrolytes generally exhibit high Li^+ conductivities of at least ∼1−10 mS/cm, with good electrochemical stability up to 4.5 V.[34,221,222] Although liquid electrolytes are not stable against reduction close to the Li/Li^+ potential, the formation of a solid−electrolyte interphase (SEI) passivates the anode/electrolyte interface and enables stable cycling (see Figure 31a,b). Nevertheless, there are significant differences in the SEI formation process when varying the anode material from metallic lithium (or lithium storage metal) to graphite/carbon.[223] SEI formation on carbonaceous (graphite) lithium storage materials takes place as a side reaction during the first reduction (charge reaction) or within a few cycles, with the least stable electrolyte components selectively reacting first (see Figure 31a). In contrast, an SEI forms on metallic lithium upon spontaneous decomposition of the electrolyte and the reactivity of the metallic lithium electrode with the electrolyte decreases as the SEI growth increases (see Figure 31b). This is because the number of electrolyte components that are sensitive to reduction when in contact with the lithium electrode is limited. Nevertheless, the surface of metallic lithium forms a new SEI in each cycle, which continues until lithium metal and/or the electrolyte are completely consumed or when the formation of high surface area lithium occurs (such as dendrites).[224] The SEI formation processes and the resulting SEI composition is therefore dependent on whether the anode is metallic lithium or graphite/carbon.[223,225] In contrast to the SEI of a lithium metal anode, which is continuously renewed during each cycle, the surface of charged carbon electrodes remain passivated by the SEI, making graphite/carbon a superior anode material compared to metallic lithium for LIBs.[226,227] Lithium storage metals like silicon or tin exhibit much larger volume changes than carbon during charging/discharging,[228] which is an additional contributing factor to SEI breaking (see Figure 31b).

In the past few years, the discovery of solid superionic conductors with ionic conductivities rivaling those of liquid electrolytes[14,15,229] have fueled intense research into all-solid-state battery (SSB) architectures.[14,230,231] SSBs are potentially safer by eschewing the use of a flammable organic solvent, and are a potential path to higher energy densities by enabling novel

https://dx.doi.org/10.1021/acs.chemrev.9b00601
Chem. Rev. 2020, 120, 6977−7019

electrode combinations (e.g., high voltage cathodes and lithium metal anodes) and architectures (e.g., stacking).

It should be noted that the types of electrolytes span a continuum ranging from liquid to polymers to glassy phases to crystals. Here, we loosely group the electrolytes into two broad classes: "liquid electrolytes", which encompasses both liquid and polymer electrolytes, and "solid electrolytes", which encompasses crystalline ceramics as well as their associated glassy phases. We will review the application of first-principles computational techniques to the study of both classes of electrolytes, including their interfaces with the electrodes.

4.2.1. Liquid Electrolytes. Computational studies of liquid electrolytes have focused on electrochemical stability and the reactions that occur at the electrode/electrolyte interface. The existence of strong ion−solvent interactions means that the electrochemical window of the electrolyte is not simply determined by the highest occupied molecular orbital (HOMO) and lowest unoccupied molecular orbital (LUMO) energy levels for isolated components,[234] although this is a frequently used approximation for high-throughput screening.[152,153] Explicit modeling of the complex salt and solvent mixture in liquid electrolytes requires simulation boxes containing hundreds or even thousands of atoms. Hence, classical MD simulations using atomistic force fields are frequently used to obtain reasonable liquid structures, in combination with first-principles calculations.[235−238]

Most studies have focused primarily on the commonly used EC/DMC solvent with or without $LiPF_6$ salt.[239−242] For example, Leung[147] used AIMD simulations to investigate the initial decomposition process of EC on graphite anodes with different edge terminations, on Li metal, and on spinel manganese oxide surfaces. They proposed two EC-reduction pathways involving one and two electrons. The one-electron mechanism (see Figure 31c) involves electron-induced cleavage of the C−O bond in EC to form EC^- radicals, followed by combination of two EC^- radicals with Li to form the major SEI product dilithium ethylene dicarbonate.[240] This reaction has been confirmed by electron paramagnetic resonance spectroscopy measurements.[243] The two-electron mechanism,[244] on the other hand, leads to the generation of either CO or C_2H_4 gas depending on the particular C−O bond cleaved (see Figure 31c).[147] These conclusions are consistent with the experimentally observed CO evolution.[245] Theoretical studies also suggest that solvent oxidation and electrode degradation are interrelated.[147] When an EC molecule binds to a 5-coordinated surface Mn(III) on the (100) surface of a spinel $Li_xMn_2O_4$ cathode, newly formed 6-coordinated Mn(III) transforms into a Mn(IV) by donating an electron to a subsurface Mn(IV). Consequently, two Mn(III) disproportionating into Mn(II) and Mn(IV) leads to Mn(II) dissolution.[147]

Østergaard et al.[233] employed DFT to investigate the oxidative decomposition of EC on layered Li_xMO_2 cathode surfaces. The motivation was to understand the electrolyte oxidation reaction (EOR) at increasing potentials as well as to rationalize the experimental report[246] that a shift to late 3d transition metal cathodes lowers the onset potential for EOR. Østergaard et al.[233] emphasized that the EOR involves reactions with the oxygen sites, which is consistent with previously reported EOR pathways involving H transfer from EC to surface oxygen of cathodes as the rate-determining step (see Figure 31d).[148,247] Consequently, there is a shift in charge as shown in a Lewis diagram (see Figure 31d). The oxidation leads to a ring opening of EC, oxygen loss from the cathode surface, and finally to CO_2 and CO evolution.[248,249] Decomposition of EC on the surface is also possible after reacting with Li or forming protonated species.[250] Thus, the criteria for a coating material to prevent EOR are low hydrogen affinity of the surface as well as suppressed oxygen release from cathode.[154,251,252]

Ramos-Sanchez et al.[253] applied coarse-grained kinetic Monte Carlo (CG-KMC) methods to understand the mechanisms associated with the early stage formation of SEI during lithium−ion intercalation on a graphite anode. It was found that the reduction of EC limits the SEI film growth rate and that the growth rate is inversely proportional to the film thickness. Although the proposed CG-KMC model is based on only the Li ethylene dicarbonate (Li_2EDC) SEI component, it can be extended for more complicated interfacial reactions involving multiple species comprising the SEI as well.[253,254]

An interesting variant of the classic EC/DMC liquid electrolytes is the recently reported superconcentrated aqueous electrolyte solutions, otherwise known as the "water-in-salt" (WIS) electrolytes.[255,256] By limiting the number of free solvent molecules, such WIS electrolytes mitigate solvent decomposition. For example, it was found that a LiTFSI-$(H_2O)_2$ WIS electrolyte is stable up to ∼3.0 V, well beyond the oxidation potential of water, and DFT calculations suggest that the $Li_2(TFSI)(H_2O)_x$ aggregates become reductively unstable at a much higher potential (2.9 V versus Li) compared to the isolated TFSI anion (1.4 V).[255] In addition, preferential reduction of $TFSI^-$ over water is attributed to the shift of the TFSI conduction band minimum and the water valence band maximum to lower potentials with increasing salt concentration. Consequently, the reduction process generates LiF (from $TFSI^-$), thus forming an anode−electrolyte interphase, which kinetically prevents further reduction of both water and $TFSI^-$. Following a similar concept, Okoshi et al.[257] theoretically investigated the concentration dependence of the structural and dynamical properties of a superconcentrated solution of sodium bis(fluorosulfonyl)amide-dimethoxyethane (NaFSA-DME). Such quantum molecular dynamics simulations with several thousand (or more) atoms for several tens of picoseconds were enabled by the recent development of a divide-and-conquer (DC) density-functional tight-binding (DFTB) method.[257−259] An analysis of the ligand exchange reaction rate revealed that the lifetime of the solution structure is of the order of 60−120 ps in the NaFSA-DME electrolyte solution. Okoshi et al.[257] analyzed the dynamical properties of Na^+ ions and suggested that the ligand exchange reactions are responsible for Na-ion diffusion via an alternative diffusion pathway in superconcentrated conditions, which often leads to a reduction in Na-ion conductivity.

Suo et al.[256] further proposed the introduction of a second lithium salt, lithium trifluoromethanesulfonate (LiOTf), to form a "water-in-bisalt" (WIBS) electrolyte. Quantum chemical calculations indicated that a WIBS electrolyte exhibits a lower reduction potential of LiOTf than that of hydrogen evolution and yields LiF as the reduction product. A combined MD and DFT simulation predicted that the addition of LiOTf to a LiTFSI solution displaced around 0.5 water molecules per Li^+ solvation shell and reduced the fraction of free water molecules from 0.15 to 0.11, thus enhancing the redox stability of electrolyte. The proposed mixed salt system promises the highest voltage (2.1 V) and energy density (100 $Whkg^1$) among all aqueous battery setups to-date.[256]

Room-temperature ionic liquids (RTILs) have also garnered substantial interest as potential electrolytes due to their

https://dx.doi.org/10.1021/acs.chemrev.9b00601
Chem. Rev. 2020, 120, 6977−7019

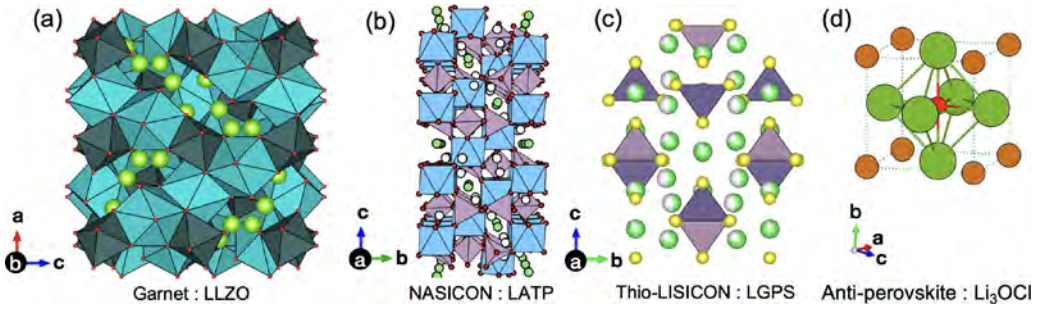

Figure 32. Crystal structures of lithium superionic conductors. (a) Garnet $Li_7La_3Zr_2O_{12}$, (b) NASICON-like $Li_{1.3}Al_{0.3}Ti_{1.7}(PO_4)_3$, (c) thio-LISICON $Li_{10}GeP_2S_{12}$, and (d) antiperovskite Li_3OCl. Color code: lithium, green; partial Li occupancy, mixed green-white; Li vacancy, white circles; oxygen, red; sulfur, yellow; chlorine, orange. Color scheme for polyhedral moieties: LaO_n, cyan; ZrO_6, bottle green; PS_4, violet; GeS_4, blue.

inherently low volatility, low flammability, high thermal stability, and potentially large electrochemical windows, relative to the typically flammable organic solvents such as EC/DMC.[260−263] Ong et al.[264] investigated the electrochemical stability window for RTILs formed from the butyl methyl immidazolum (BMIM) and *N*,*N*-propylmethylpyrrolidinium (P_{13}) cations, and the PF_6, BF_4, and (trifluoromethylsulfonyl)imide (TFSI) anions using a combination of classical MD simulations and DFT calculations. Besides finding that explicit modeling of the RTIL structure yields much better agreement with experimentally measured electrochemical windows compared to simplified gas phase or polarizable continuum model calculations, two key findings are that the TFSI anion is less stable toward reduction compared to the P13 cation,[265] and some cations (e.g., the aromatic BMIM) can also be less stable against oxidation when paired with specific anions (e.g., PF_6).

Several efforts have attempted to identify the complex structure in magnesium−chloride complexes of the electrolytes for magnesium-ion batteries.[266,267] Pour et al.[268] established that the magnesium ion exists as a six coordinated ion in THF, primarily in the form of $MgCl^+$(5THF) monomers or $Mg_2Cl_3^+$(6THF) dimers. In contrast, theoretical investigations by Wan and Prendergast[269] elucidated that the $MgCl^+$ monomer is always coordinated by three THFs, leading to a total Mg coordination of four, which was supported by experimental NMR and XANES results.[270] Subsequently, Canepa et al.[271] combined DFT and classical MD calculations and benchmarked the modeling strategy using previous experimental/theoretical results on several magnesium−chloride complexes in different THF environments. It was shown that the most stable magnesium aluminum chloride complexes (MACCs), $MgCl^+$(3THF), and $MgCl_2$(2THF) are 4-fold coordinated. On the other hand, the $Mg_2Cl_3^+$(4THF) dimer and $Mg_3Cl_5^+$(6THF) trimer prefer 5-fold and 6-fold coordination, respectively. These results are consistent with the earlier theoretical study by Wan and Prendergast[269] and a XANES spectroscopy study by Nakayama et al.[270] When computing the reaction energies (ΔE_{D-H}) of MACCs in THF, Canepa et al.[271] employed the Debye−Hückel correction to the reaction energy obtained from DFT calculations at infinite dilution (ΔE).

Polymer electrolytes are yet another class of alternatives to organic solvents, with improved mechanical stability, moisture resistance, electrochemical windows, and thermal stability.[272] Many computational studies have focused on poly(ethylene oxide) (PEO) and related polymers blended with Li salts, but the performance of such electrolytes are generally limited by poor low-temperature conductivity due to the unfulfilled requirement of segmental chain motion for ion transport.[273] Johansson et al.[274] modeled an amorphous Li salt−PEO polymer electrolyte by considering Li ion-*n*-glyme [CH_3O-(CH_2CH_2O)nCH_3, n = 4−6] complexes and revealed 23 different stable complexes with Li-coordination numbers of 4 to 6. Further development of a solid-state composite polymer electrolyte based on PEO as a matrix, $LiClO_4$ as the salt, and inorganic hybrid poly(cyclotriphosphazene-*co*-4,40-sulfonyldiphenol) (PZS) microspheres as filters leads to enhanced Li conductivity. Balbuena et al.[275] performed both ab initio and classical MD simulations and proposed a higher Li diffusion coefficient in PZS than in PEO electrolyte membranes. Subsequently, Maitra and Heuer[276] showed that fast cation hopping between different chains is crucial for the transport of ions in polymer electrolytes. Seo et al.[277] used kinetic Monte Carlo and hybrid lattice Monte Carlo simulations to study the cationic diffusion in homopolymer and block copolymer systems and found an increased diffusivity of ions in block copolymers with increasing molecular weight, which is in agreement with experimental findings.[278] However, simulations of polymer architectures face unique challenges such as the lack of methodologies to study the interplay between morphology and its control over ionic transport.[279,280] In particular, the development of methods to study dynamics of ions while accounting for dielectric inhomogeneities[281−284] could pave the way for future development of polymer electrolytes with improved ionic diffusion, stability, and flexibility.

4.2.2. Solid Electrolytes. Although solid electrolytes have been known since the 1970s,[285,286] they have enjoyed a resurgence of interest during the past decade with an increased emphasis on thermal safety as alkali-ion batteries move beyond consumer electronics to automotive and grid energy storage applications. In this section, we review computational studies of solid electrolytes belonging to three broad chemical groups, namely oxides, sulfides, and others. Figure 32 shows the crystal structures of selected superionic conductors from each group.

1. Oxides, which include the well-known natrium superionic conductors (NASICONs), $Na_{1+x}Zr_2Si_xP_{3-x}O_{12}$,[285,286] lithium super ionic conductor (LISICON) type $Li_{14}Zn(GeO_4)_4$,[287] perovskite-type $Li_xLa_{2/3-x}TiO_3$ (LLTO),[288] and Li garnets with composition $Li_xLn_3M_2O_{12}$ (x = 5−7, M = Te, W, Zr; Ln = lanthanides).[230,231,289]

2. Sulfides, which include the $Li_2S-P_2S_5$ glass/glass-ceramics,[290,291] thio-LISICON LGPS family with chemical formula $Li_{4-x}M_{1-x}P_xS_4$ ($0 < x < 1$; M = Si, Ge, Sn),[14] argyrodites with formula Li_6PS_5X (X = Cl, Br, I),[292] Na_3PS_4,[16] and its analogues.

https://dx.doi.org/10.1021/acs.chemrev.9b00601
Chem. Rev. 2020, 120, 6977−7019

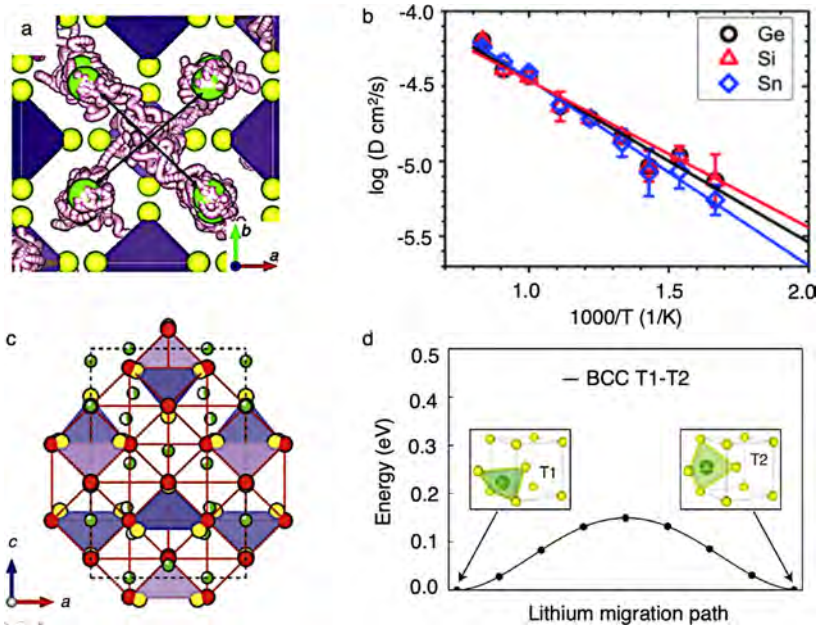

Figure 33. (a) Li-ions trajectory from AIMD simulations showing Li^+ diffusion pathways along *ab* plane in addition to the *c* channel. Reproduced with permission from ref 318. Copyright 2013 American Chemical Society. (b) Li diffusion characteristics after isovalent cation (Si^{4+} and Sn^{4+}) substitutions in LGPS structure. Reproduced with permission from ref 319. Copyright 2013 Royal Society of Chemistry. (c) Mapping of the S (anion) sublattice in crystal structure of LGPS to a bcc framework. (d) Li-ion migration path and calculated migration barrier in bcc type sulfur sublattice arrangement in LGPS. LiS_4 tetrahedra are colored as green. Reproduced with permission from ref 320. Copyright 2017 Nature Publishing Group.

3. Others such as nitrides (e.g., Li_3N[293−295]), oxynitrides (e.g., lithium phosphorus oxynitride or LiPON[296,297]), and oxyhalides such as the antiperovskite Li_3OX (X = Cl, Br).[298]

4.2.2.1. Oxides. The lithium-stuffed garnets based on $Li_7La_3Zr_2O_{12}$ (LLZO) are among the most well-studied solid electrolytes due to their relatively high ionic conductivities (typically 0.1 mS/cm or higher) and their stability against Li metal. The cubic-type LLZO[230,299] exhibits Li ionic conductivity on the order of 10^{-4} S cm^{-1} (at room temperature), which drops to a significantly lower value of 10^{-6} S cm^{-1} for the low-temperature tetragonal phase.[300,301] Jalem et al.[302] investigated the ion dynamics and Li occupancy of LLZO using AIMD simulations. They showed that the high Li conductivity in LLZO can be attributed to a concerted migration mechanism over a three-dimensional network of face-sharing tetrahedral and octahedral interstitial sites that are partially filled.[302] Similar conclusions were drawn using NEB calculations[303] for LLZO and for other superionic conductors.

The ionic conductivity of the garnets has been shown both experimentally and computationally to be highly sensitive to doping. As the lithium composition increases from $x = 3$ to $x = 7$ in the $Li_xLn_3M_2O_{12}$ garnet (Ln = La, Rb; M = Zr, Ta), lithium ions begin to occupy the higher energy octahedral sites. This occurs because the number of tetrahedral sites are limited and partial occupancy of octahedral sites allows for a reduction of electrostatic repulsion between Li ions.[304] The net effect is to reduce the energy difference between the tetrahedral and octahedral sites, resulting in a lower migration barrier and a higher Li conductivity.[305,306] With AIMD simulations, Miara et al.[306] showed that Ta^{5+} doping of LLZO substantially reduces the activation barrier and increases the conductvity of LLZO, with a maximum conductivity at $Li_{6.75}La_3Zr_{1.75}Ta_{0.25}O_{12}$, while small amounts of Rb doping initially lowers the activation barrier but then causes a rapid decrease in conductivity at higher concentrations. The effect of dopants on conductivity is attributed to changes in lithium concentration and hence the number of mobile carriers in the solid electrolyte.[307,308] Using DFT and variable cell shape MD simulations, Bernstein et al.[309] demonstrated the effect of supervalent ion (Al^{3+}) doping into the LLZO system. Upon Al incorporation, charge compensation is achieved through the creation of vacancies on the Li sublattice, resulting in an increase in the overall entropy, which in turn reduces the free energy gain from ordering and stabilizes the cubic phase. It was estimated that the high conductivity cubic phase can be achieved at a critical Al concentration of $x = 0.2$ in $Li_{7-2x}Al_x$ $La_3Zr_2O_{12}$, which is consistent with experiment.[309]

Despite the fact that aliovalent doping leads to charge-compensating Li vacancies and serves as one strategy for optimizing ionic conductivities,[309] it is still unclear to what degree the vacancy-compensation model is valid. Squires et al.[310] addressed this question by performing hybrid DFT calculations to understand defect chemistry in LLZO. The self-consistent defect concentration as a function of component chemical potentials reflects the influence of synthesis conditions and dopant concentrations on the defect chemistry, which includes O vacancies, Li interstitials, and cation antisite defects in addition to Li vacancies. For example, under reducing conditions, O vacancies prevail and act as electron traps. Li/Zr antisite defects act as the dominant compensating defect under Li-rich/Zr-poor conditions. Thus, supervalent doping does not always produce charge compensating Li vacancies. This study showed that first-principles defect calculations in combination with a grand-canonical thermodynamic model can be invaluable to understand the defect chemistry and doping response and to suggest rational synthetic schemes for optimizing the properties solid electrolytes.

Grain boundaries (GBs) and secondary phases can be a significant source of high impedance in many oxide solid electrolytes, resulting in much lower total conductivities in

https://dx.doi.org/10.1021/acs.chemrev.9b00601
Chem. Rev. 2020, 120, 6977−7019

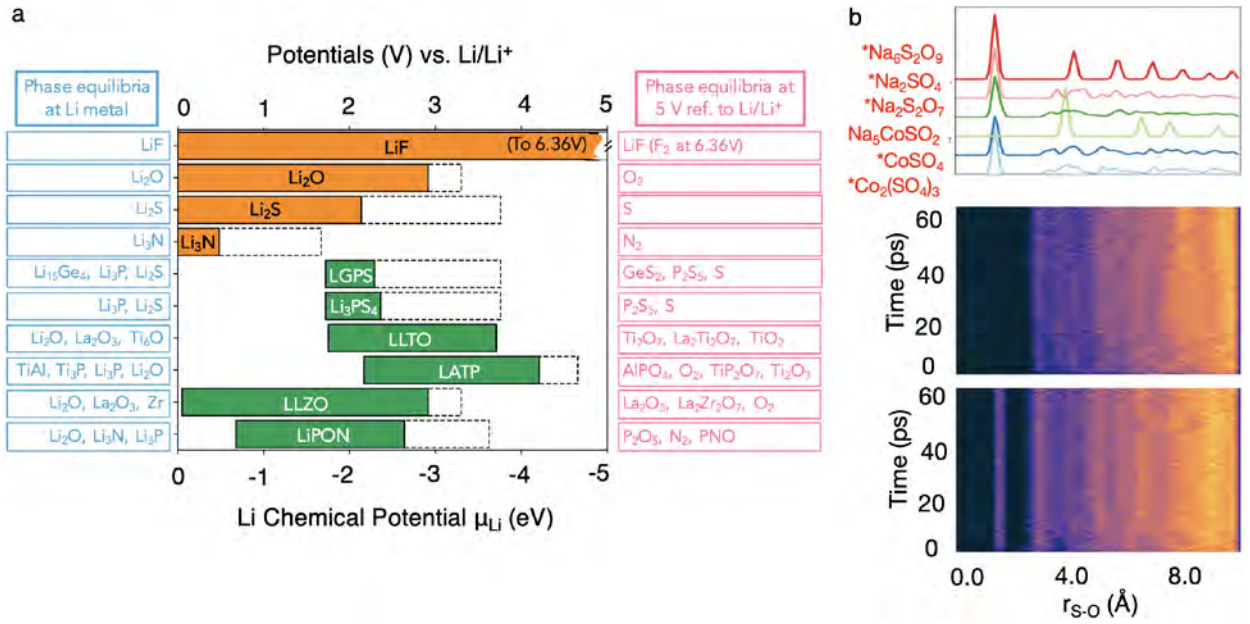

Figure 34. (a) Equilibrium composition of selective solid electrolytes at 0 and 5 V vs Li/Li^+. The dashed lines dictate the potential at which the compound is fully delithiated. Orange and green colored shaded bar represents the intrinsic electrochemical stability window for respective solid electrolyte. Reproduced with permission from ref 360. Copyright 2018 Elsevier. (b) Evolution of the S−O radial distribution function at the cathode/SE ($NaCoO_2/Na_3PS_4$) interfaces with respect to AIMD simulation time. The references labeled with an asterisk correspond to the products at $Na_{0.5}CoO_2/Na_3PS_4$ (charged) interface. Heat maps at the middle and bottom are for $NaCoO_2/Na_3PS_4$ and $Na_{0.5}CoO_2/Na_3PS_4$ interfaces, respectively. Reproduced with permission from ref 149. Copyright 2016 American Chemical Society.

polycrystalline materials relative to the bulk single crystal.[311−313] Despite the fact that the high bulk ionic conductivity in NASICONs have been known since the 1970s,[285,286] the presence of ZrO_2 or Na_3PO_4 at the GBs leads to much lower total ionic conductivity. Using NEB and AIMD simulations, Samiee et al.[314] studied the effects of aliovalent doping on both the bulk and GB conductivity of NASICON $Na_3Zr_2Si_2PO_{12}$. Interestingly, it was found that Mg^{2+} and Ni^{2+} have relatively low solubility in the NASICON structure and segregate to the secondary Na_3PO_4 phase, where they have much higher solubility. The doping of Na_3PO_4 significantly improves the GB conductivity, consequently increasing the total ionic conductivity to above 2 mS/cm.

4.2.2.2. Sulfides. Compared to the oxides, far more computational studies have focused on the sulfide solid electrolyte materials. The reasons are three-fold. First, the ionic conductivity of the sulfides tend to be higher than the oxides, which means that sufficient diffusion statistics can be accessed within reasonable AIMD simulation time frames.[315−317] Second, sulfides tend to have much lower intrinsic electrochemical and chemical stability compared to oxides, which has stimulated much computational effort into understanding the interfacial reaction products and their effects on battery performance. Finally, the recent explosion in the number of newly discovered crystalline sulfide superionic conductors in both Li-ion and Na-ion chemistries have given rise to many computationally driven discovery and optimization efforts.

Among the most promising SEs to emerge in recent years is the $Li_{10}GeP_2S_{12}$ (LGPS) family of superionic conductors with ionic conductivities exceeding 10 mS/cm.[14,321−323] Shortly after its reported discovery by Kamaya et al.,[14] two major computational works by Mo, Ong, and Ceder[318,319] provided much needed insights into the diffusion mechanisms and electrochemical stability of the LGPS superionic conductor as well as potential avenues for further optimization. Contrary to initial beliefs that it is a 1D conductor that is stable across a >5 V window, AIMD simulations, and Li grand potential phase diagrams demonstrated that it is in fact an anisotropic 3D conductor (see Figure 33a) that is intrinsically unstable at typical anode and cathode voltages, i.e., ∼0 V and above 2.5 V vs Li/Li^+ (see Figure 34a), respectively.[318] These computational findings were subsequently verified using neutron diffraction experiments.[324] Further, it was demonstrated by Ong et al.[319] that the Si/Sn analogues are likely to retain the same high ionic conductivity as LGPS itself (Figure 33b) but with far lower cost. However, the oxide analogues of LGPS are unlikely to be stable and are predicted by AIMD to have far lower ionic conductivities. These predictions were subsequently confirmed experimentally with the successful synthesis of $Li_{10}SnP_2S_{12}$,[321] $Li_{10}SiP_2S_{12}$,[322] and $Li_{11}AlP_2S_{12}$.[323] $Na_{10}SnP_2S_{12}$ has also been computationally predicted and synthesized, though with somewhat lower ionic conductivity than the Li compounds.[325]

The high conductivity of the LGPS family, as well as $Li_7P_3S_{11}$ glass-ceramic,[326] has been attributed to their body-centered cubic-like anion framework, which allows direct Li hops between adjacent tetrahedral sites with low activation barrier (see Figure 33c,d).[320] Using this design principle, Richards et al.[327] identified a new lithium superionic conductor $Li_{1+2x}Zn_{1-x}PS_4$ ($x = 0−0.75$) with room temperature Li^+-conductivity predicted to be >10 mS cm^{-1}, which has been verified experimentally.[328]

Another class of highly promising Li SEs are the argyrodites with formula Li_6PS_5X (X = Cl, Br, I). A particularly interesting aspect of the argyrodites is the diffusion topology, which comprises of interconnected Li_6S cages. Hopping within the cages, while effectively barrierless, does not contribute to long-range Li conduction. However, AIMD simulations have shown that anion site disorder with excess Li increases the occupancy of Li in the connecting sites, leading to several orders of magnitude increase in ionic conductivity.[316]

https://dx.doi.org/10.1021/acs.chemrev.9b00601
Chem. Rev. 2020, 120, 6977−7019

For Na-ion chemistry, it is interesting to note that the Na sulfide superionic conductors that have been discovered thus far typically have different crystal structures and diffusion topologies from the lithium sulfide superionic conductors. By far the two most promising classes of Na sulfide superionic conductors belong to the Na_3PnX_4 family (Pn = P, Sb, As; X = S, Se).[16,329−333] Similar to LGPS, AIMD simulations have provided critical insights into the diffusion mechanisms in this class of superionic conductors.[325,334] For example, it was computationally established that stoichiometric Na_3PS_4, whether in the tetragonal or cubic polymorph, has relatively poor ionic conductivity, and it is only with the introduction of Na defects such as interstitials or vacancies that conductivities above 0.1 mS/cm are achieved.[335] The formation of such defects can be facilitated with the introduction of aliovalent cation (e.g., P^{5+} for Si^{4+} or Sn^{4+})[335] or anion (e.g., S^{2-} for Cl^-)[330,336] doping, with conductivities above 1 mS/cm predicted by AIMD and confirmed experimentally.[330,337] Interestingly, Cl-doped Na_3PS_4 (NPSC) produces NaCl as a reaction byproduct at the interface, which helps to mitigate the further decomposition of Na_3PS_4, hence improving the electrochemical stability and cycling. Cation-substituted $Na_3P_xAs_{1-x}S_4$[338] and Na_3SbS_4[339,340] have also been shown to result in significant improvement in the aqueous stability, although the toxicity of As is a major concern, while anion-substituted Na_3PSe_4[329,341] and Na_3SbSe_4[342] exhibit higher ionic conductivities, albeit at a substantial reduction in stability and increase in cost.

Recently, several works[343−346] reported the discovery of the $Na_{11}Sn_2PnX_{12}$ (Pn = P, Sb; X = S,Se) phase, having among the highest sodium ionic conductivity (>1 mS/cm at room temperature) to date for sulfide-based materials. Zhang et al.[343] proposed that the equi-energetic sodium sites lead to quasi-isotropic diffusion, which is the origin of the high ionic conductivity. On the other hand, Duchardt et al.[344] proposed a vacancy-controlled Na^+ superionic conduction mechanism. They argued that the $Na_{11}Sn_2PS_{12}$ structure is analogous to the Na_3PS_4 structure containing a vacant Wyckoff position (8b), and this vacant site facilitates the migration of sodium ions.[344] Subsequently, Oh et al.[347] carried out a comprehensive investigation on the diffusion mechanism of $Na_{11}Sn_2PS_{12}$ using extended AIMD simulations. This study demonstrated that 8b sites do not participate in diffusion unless they are occupied by sodium. Interestingly, aliovalent substitution to create sodium vacancies or interstitials was found to have a negligible effect on the ionic conductivity. On the other hand, isolvalent substitution to create an expanded lattice, and hence, wider diffusion channels, lead to enhanced ionic conductivity. Analyses of the site occupancies indicated that $Na_{11}Sn_2PS_{12}$ exhibits nearly isotropic Na diffusion, where all Na sites along with well distributed sodium vacancies actively participate in overall conductivity.

For multivalent Mg^{2+} chemistry, chalcogenide spinels, MgM_2X_2 (M = Sc, In; X = S, Se), have been proposed as potential solid electrolytes, although they suffer from self-discharge due to considerable electronic conductivity. Using first-principles calculations, Canepa et al.[348] evaluated the defect formation energies as a function of synthesis conditions, revealing Mg-vacancies and Mg-M antisites (M = Sc or In) as the dominant point defects. It was also found that the anion-excess conditions and slow cooling can lead to low electronic conductivity. As a proof of concept, the introduction of aliovalent dopants, such as Ce and Ti on Sc, were shown to mitigate the electronic conductivity observed in $MgSc_2Se_4$. These examples highlight the importance of defects in the field of solid electrolytes.

4.2.2.3. Solid−Solid Interfacial Stability. As the electrolyte is subject to both high and low extrema in alkali chemical potential, a substantial body of computational work has been devoted to analyzing the interfacial reactivity between solid electrolytes and electrodes. Indeed, several high-throughput (HT) computational studies have been performed on various chemistries.[149,349−354] These studies relied on thermodynamic equilibrium criteria, assuming either a sufficiently high alkali mobility such that the cathode and anode could be treated as alkali sinks and sources, respectively,[318] or full interspecies exchange.[349] The general conclusion from these HT studies is that sulfides have a much narrower window of electrochemical and chemical stability compared to oxides, and that few, if any, superionic conductors are inherently stable against alkali metal anodes. The thermodynamic approximations have proven to be remarkably effective, and reaction products predicted using these approaches (see Figure 34a) have been verified experimentally.[326,353,355−357] High-throughput studies have provided invaluable insights into the chemical origins of electrolyte−electrode instability. For instance, the high reactivity between transition metal oxide cathodes (e.g., $NaCoO_2$) and the thiophosphate based superionic conductors (e.g., Na_3PS_4) can be attributed to the highly exothermic exchange reaction to form phosphate groups.[353] Such high reaction energies can be mitigated with the suitable choice of cathode (e.g., polyanion cathodes) and/or buffer layer (e.g., Al_2O_3).[149,354]

Nevertheless, it should be noted that kinetics do play a substantial role in determining the products formed at the interface. A recent study by Tang et al.[149] using AIMD simulations of explicit interfacial models of $NaCoO_2/Na_3PS_4$ interface found that the reaction products comprises SO_4^{2-} compounds and Na_3P, without any evidence for PO_4^{3-} formation, in disagreement with the predictions from thermodynamic approximations (see Figure 34b). A fundamental limitation is that such AIMD simulations can only be performed on relatively short time scales (O(10 ps)). It should also be noted that there have been earlier studies[358] attempting to use DFT computations to investigate the explicit structure, electronic states, and transport at the $LiCoO_2$ cathode/β-Li_3PS_4 solid electrolyte interface. However, these studies relied on 0K DFT relaxations (as opposed to finite-temperature MD simulations) of a coherent interface. It is unclear whether the conclusions drawn from such a simulation model and approach are valid at real-world interfaces. For instance, one would expect substantial reactivity between $LiCoO_2$ and β-Li_3PS_4 from purely thermodynamic considerations alone.[350,353]

An interesting question is whether the formation of electrochemical double layers at the interface of a solid-state Li ion battery plays a crucial role. Stegmaier et al.[359] modeled a Li_3OCl−cathode interface by treating the cathode as a metallic intercalation material using a polarizable continuum model with dielectric constant of 1000. Using DFT-computed formation energies of the charge carriers in Li_3OCl, it was found that Li^+ vacancies are dominant at the cathode. In addition, the repulsive or attractive interaction between defects was found to be very short-ranged (on the order of a lattice constant). This is due to the fact that the structural relaxations around Li^+ defects in Li_3OCl are local, resulting in strong screening. Such short-range repulsive interactions of the vacancies at the interface helps to

https://dx.doi.org/10.1021/acs.chemrev.9b00601
Chem. Rev. 2020, 120, 6977−7019

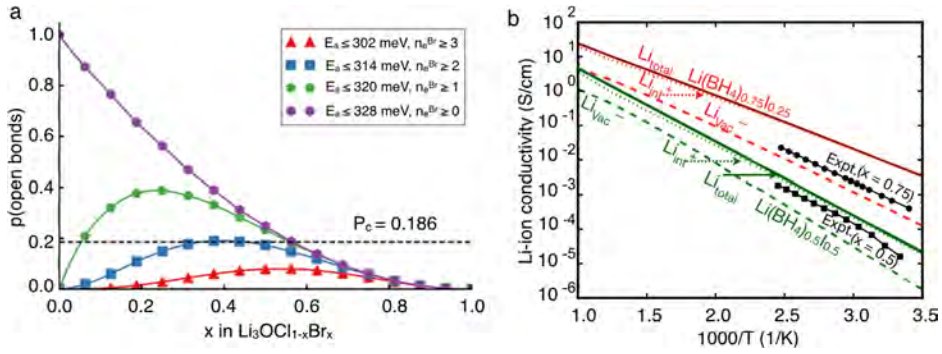

Figure 35. (a) Probability of open bonds, p(open bonds), in antiperovskite $Li_3OCl_{1-x}Br_x$ system at various Br^- concentrations. Each curve corresponds to specific barrier cutoff and N_e^{Br} denotes the number of Br^- surrounding Li at terminal points. Black dashed line indicates the bond percolation threshold. (b) Computed Li^+-ion conductivities of $Li(BH_4)_{0.75}I_{0.25}$, $Li(BH_4)_{0.5}I_{0.5}$, and $Li_{0.75}K_{0.25}BH_4$ as a function of temperature (attempt frequency = 1013). Reproduced with permission from ref 368. Copyright 2018 American Physical Society.

build large vacancy concentrations in a single layer at the SE/cathode interface, forming a compact double layer.[359]

4.2.2.4. Other Chemistries. Compared to the oxides and sulfides, other chemistries, such as the nitrides, oxynitrides, and oxyhalides, offer varying trade-offs between ionic conductivity and electrochemical/chemical stability. Al-Qawasmeh and Holzwarth[361] investigated two lithium oxonitridophosphates: $Li_{14}P_2O_3N_6$ and Li_7PN_4. Both SEs were found to relatively stable against Li metal anode with significantly less exothermic reaction energies with Li compared to Li_3PO_4.[362] These findings are in agreement with experimental observations.[363]

A number of computational studies[364−366] have also been carried out on the antiperovskites Li_3OX (X = Cl, Br), a new class of superionic conductors first proposed by Zhao and Daemen.[298] For example, Deng et al.[364] using NEB calculations demonstrated that a combination of Cl-rich diffusion channel associated with Br-rich hopping end points leads to low vacancy migration barriers in mixed halide antiperovskite, $Li_3OCl_{1-x}Br_x$. By combining NEB calculations with a bond percolation model, they identified an optimal composition of $Li_3OCl_{0.75}Br_{0.25}$ to maximize Li conductivity (see Figure 35a), which is further confirmed using AIMD simulations. More recently, it has been shown that the presence of H in Li-halide hydroxides (Li_2OHX) results in significantly higher Li^+ conductivity due to a mechanism that involves OH^- group rotations creating Frenkel defects.[367]

Using KMC simulations, Yao et al.[368] calculated the room-temperature lithium ion conductivities for the highly promising iodide-mixed $LiBH_4$ superionic conductor. Simulation results suggest that a lower I concentration ($Li(BH_4)_{0.75}I_{0.25}$) facilitates the formation of more defects, leading to a higher lithium ion conductivity of 5.7×10^{-3} S/cm, which is 2 orders of magnitude higher than $Li(BH_4)_{0.5}I_{0.5}$ (see Figure 35b). Cation/anion substituents were proposed as a means to stabilize $LiBH_4$-based lithium ion conductors with among the highest Li^+-ion conduction in $LiBH_4$ systems.

While AIMD is becoming increasingly accessible with algorithmic, software, and computing power advancements, the poor scaling of ab initio methods still limits its application to relatively small model systems and short time simulations. On the other hand, linear-scaling classical potentials such as the embedded atom method (EAM) have substantial compromises in terms of transferability and accuracy. As discussed in section 3.3.3, machine learning interatomic potentials (ML-IAPs) trained on DFT computations have emerged in recent years as a fascinating alternative that offers near-DFT accuracy with linear scaling. Such ML-IAPs have been applied to the study of solid electrolyte materials. For example, Li et al.[369] trained a neural network potential (NNP) for Li_3PO_4, the major component for amorphous thin-film solid electrolyte LIPON. Trained on DFT total energies for various atomic configurations, the NNP shows good predictive capabilities for critical quantities related to Li vacancy formation energies and migration barriers and is able to reproduce diffusivities matching AIMD simulations for crystalline Li_3PO_4. The NNP was subsequently employed in large-scale simulations of Li diffusion in amorphous Li_3PO_4, and the obtained activation energy of 0.55 eV matches experimental measurements ~0.57 eV. Deng et al.[142] also trained a linear potential combining the spectral neighbor analysis potential (SNAP) formalism[141] with electrostatic interactions for one of the earliest discovered Li superionic conductors, Li_3N. The electrostatic SNAP (eSNAP) shows good predictive power on quantities benchmarked from DFT but only uses a fraction of data required to train NNPs. Large-scale MD simulations were performed on bulk Li_3N to calculate the Haven ratio, a quantity generally not accessible by AIMD simulations. The values obtained agree with NMR measurements along different crystallography orientations, and another large-scale simulation revealed faster Li ionic kinetics within the twist grain boundary of Li_3N compared to the bulk.

5. PERSPECTIVES

The aim of this review has been to describe the theory (section 2) and computational approaches (section 3) that connect the electronic structure and dynamical properties of the components of rechargeable batteries to their electrochemical properties at the macroscopic level. The behavior of a rechargeable battery at the engineering level can be described and modeled with powerful phenomenological theories that are rooted in the laws of thermodynamics and based on elementary principles of kinetics. The voltage of a battery and the phase stability of the materials that make up the battery, for example, can be understood and predicted with knowledge of the free energies of the participating phases (section 2.1). Furthermore, the rates with which a battery can be charged and discharged depend on kinetic properties at a phenomenological level that is encoded in different measures of ion mobility and in the parameters of response functions describing nonequilibrium electrochemical processes at electrode/electrolyte interfaces (section 2.2). There are also well-established phenomenological theories that describe the evolution of phase transformations within an

https://dx.doi.org/10.1021/acs.chemrev.9b00601
Chem. Rev. 2020, 120, 6977−7019

electrode as the concentration of the shuttled ion is varied (section 2.3). While remarkably simple and at the same time powerful, phenomenological theories require experimental measurements to establish the materials specific thermodynamic potentials and kinetic coefficients that they rely on. An alternative to an experimental approach is to instead calculate thermodynamic and kinetic quantities from first principles. While first-principles electronic structure methods are now reasonably mature and reliable (section 3.1.1), the electrochemical processes of rechargeable batteries are in general thermally activated, making temperature and entropy crucial variables that need to be accounted for. Hence, any first-principles approach that connects to phenomenological models of batteries must rely on statistical mechanics (section 3.2.1).

In this review, we have described rigorous approaches to calculate equilibrium thermodynamic properties and ionic transport coefficients from first principles. As is evident from a survey of the literature summarized in sections 4.1 and 4.2, these computational approaches have proven to be an invaluable complement to a wide array of experimental probes in providing fundamental insights about the behavior of battery materials. The list of properties that can be calculated from first-principles with rigor, however, is unfortunately still limited. There are many phenomena where the link between electronic structure and the parameters of macroscopic response functions remain poorly understood. In some instances, the accurate and validated phenomenological response functions themselves are still lacking.

We identify the following areas where future research would enable significant advances in our ability to model and design new battery chemistries and concepts:

- The development of statistical mechanics methods to predict ingredients for phase field models of topotactic phase transformations, including gradient energy coefficients and ionic mobilities in regions where phases are thermodynamically unstable and susceptible to spinodal decomposition.
- Mesoscale models that describe the chemomechanical coupling that drive stacking sequence change phase transformations in layered intercalation compounds. A large fraction of commercial and candidate electrode materials have a layered crystal structure that undergo changes in the stacking sequence between their two-dimensional building blocks as the concentration of the intercalating guest ions is varied. There are currently no rigorous phenomenological models that couple the chemical driving forces due to composition changes and the mechanical interactions that accompany local transitions in stacking sequences.
- It is increasingly recognized that particle fracture plays an important role in degradation processes of rechargeable batteries. A key challenge in battery applications is that the mechanical properties, in particular the fracture toughness, is very sensitive to environmental conditions, which continuously change with a change in the voltage as the battery is cycled.[370]
- Perhaps least well understood are the complex atomic and electronic processes that occur at the electrode−electrolyte interfaces of rechargeable batteries. More in situ experiments and multiscale modeling with electronic and atomic-level resolution is necessary to characterize the structure of the interface and to determine kinetic processes that occur there during battery charging and discharging. The insights of such studies then need to be distilled into interface response functions similar to that of a Butler−Volmer equation. However, a link needs to be established between quantities and properties that can be calculated at the atomistic level and the phenomenological coefficients that appear in such a response function.
- A critical gap remains in our ability to simulate materials with chemical accuracy at the meso-/microscales. This is particularly relevant to the understanding of chemical reactions and transport at the electrode−electrolyte interfaces as well as within the electrodes and electrolytes themselves (e.g., grain boundaries/secondary phases). While recent developments in machine learning interatomic potentials show promise in relatively simple chemistries, methodological developments that enable universal application to complex chemistries and bonding types, especially electron transfer, are sorely needed.

AUTHOR INFORMATION

Corresponding Authors

Shyue Ping Ong − *Department of NanoEngineering, University of California, San Diego, La Jolla, California 92093-0448, United States*; orcid.org/0000-0001-5726-2587; Phone: (858) 534-2668; Email: ongsp@eng.ucsd.edu

Anton Van der Ven − *Materials Department, University of California, Santa Barbara, Santa Barbara, California 93106-5050, United States*; Email: avdv@engineering.ucsb.edu

Authors

Zhi Deng − *Department of NanoEngineering, University of California, San Diego, La Jolla, California 92093-0448, United States*

Swastika Banerjee − *Department of NanoEngineering, University of California, San Diego, La Jolla, California 92093-0448, United States*

Complete contact information is available at: https://pubs.acs.org/10.1021/acs.chemrev.9b00601

Notes

The authors declare no competing financial interest.

Biographies

Anton Van der Ven is a Professor of Materials at the University of California, Santa Barbara. His research seeks to unravel the links between the electronic structure of solids and their macroscopic properties using first-principles statistical mechanics. He studies a wide variety of materials classes for electrochemical energy storage and high temperature aerospace applications. His group develops statistical mechanics methods and accompanying software tools to predict the properties of complex crystals from first principles. Van der Ven studied metallurgy and applied materials science at the Katholieke Universiteit Leuven and obtained a Ph.D. in Materials Science at the Massachusetts Institute of Technology.

Zhi Deng is a Postdoc of NanoEngineering at the University of California, San Diego. His research interests focus on understanding thermodynamic and kinetic properties of materials in rechargeable batteries and designing solid-state electrolytes using first-principles methods and atomistic simulations. He studied Materials Science and Engineering at Tsinghua University and obtained his Ph.D. in NanoEngineering from the University of California, San Diego.

https://dx.doi.org/10.1021/acs.chemrev.9b00601
Chem. Rev. 2020, 120, 6977−7019

Swastika Banerjee is a Postdoc of NanoEngineering at the University of California, San Diego. Her research interest includes large-scale energy storage and understanding electron−hole transport in semiconductors based on first-principles methods coupled with Boltzmann transport equation. Prior to moving to San Diego, she was postdoctoral research fellow and affiliate in the Materials Sciences Division, Lawrence Berkeley National Laboratory, and Shenzhen University, focusing on the Battery Materials Research. She obtained her Ph.D. in Computational Materials Science from Jawaharlal Nehru Centre for Advanced Scientific Research (JNCASR, Bangalore) and pursued a Master of Science in Chemistry from Indian Institute of Technology, Kharagpur.

Shyue Ping Ong is an Associate Professor of NanoEngineering at the University of California, San Diego. His group, the Materials Virtual Lab, focuses on the interdisciplinary application of machine learning and first-principles computations to accelerate materials design. His major technological areas of interest include energy storage, solid-state lighting, and alloys for extreme environments. He is a key developer of the Materials Project and the Python Materials Genomics (pymatgen) materials library, as well as several materials machine learning software packages. Dr. Ong obtained his Ph.D. in Materials Science and Engineering from the Massachusetts of Technology and his Master in Electrical and Information Science Engineering from the University of Cambridge.

ACKNOWLEDGMENTS

A. Van der Ven, Z. Deng, and S. P. Ong were supported as part of the NorthEast Center for Chemical Energy Storage (NECCES), an Energy Frontier Research Center funded by the U.S. Department of Energy, Office of Science, Basic Energy Sciences, under award no. DE-SC0012583. S. Banerjee was supported by Shell.

REFERENCES

(1) Whittingham, M. S. Electrical energy storage and intercalation chemistry. *Science* **1976**, *192*, 1126−7.
(2) Whittingham, M. S. Lithium Batteries and Cathode Materials. *Chem. Rev.* **2004**, *104*, 4271−4302.
(3) Whittingham, M. S. Ultimate limits to intercalation reactions for lithium batteries. *Chem. Rev.* **2014**, *114*, 11414−11443.
(4) Canepa, P.; Sai Gautam, G.; Hannah, D. C.; Malik, R.; Liu, M.; Gallagher, K. G.; Persson, K. A.; Ceder, G. Odyssey of Multivalent Cathode Materials: Open Questions and Future Challenges. *Chem. Rev.* **2017**, *117*, 4287−4341.
(5) Hohenberg, W.; Kohn, P. Inhomogeneous electron gas. *Phys. Rev.* **1964**, *136*, B864.
(6) Kohn, W.; Sham, L. J. Self-Consistent Equations Including Exchange and Correlation Effects. *Phys. Rev.* **1965**, *140*, A1133.
(7) Perdew, J. P.; Burke, K.; Ernzerhof, M. Generalized Gradient Approximation Made Simple. *Phys. Rev. Lett.* **1996**, *77*, 3865−3868.
(8) Sun, J.; Ruzsinszky, A.; Perdew, J. Strongly Constrained and Appropriately Normed Semilocal Density Functional. *Phys. Rev. Lett.* **2015**, *115*, No. 036402.
(9) Lejaeghere, K.; et al. Reproducibility in density functional theory calculations of solids. *Science* **2016**, *351*, aad3000−aad3000.
(10) Jain, A.; Ong, S. P.; Hautier, G.; Chen, W.; Richards, W. D.; Dacek, S.; Cholia, S.; Gunter, D.; Skinner, D.; Ceder, G.; Persson, K. A. Commentary: The Materials Project: A materials genome approach to accelerating materials innovation. *APL Mater.* **2013**, *1*, No. 011002.
(11) Nitta, N.; Yushin, G. High-capacity anode materials for lithium-ion batteries: choice of elements and structures for active particles. *Particle & Particle Systems Characterization* **2014**, *31*, 317−336.
(12) McDowell, M. T.; Lee, S. W.; Nix, W. D.; Cui, Y. 25th anniversary article: understanding the lithiation of silicon and other alloying anodes for lithium-ion batteries. *Adv. Mater.* **2013**, *25*, 4966−4985.
(13) Xu, K. Nonaqueous Liquid Electrolytes for Lithium-Based Rechargeable Batteries. *Chem. Rev.* **2004**, *104*, 4303−4418.
(14) Kamaya, N.; Homma, K.; Yamakawa, Y.; Hirayama, M.; Kanno, R.; Yonemura, M.; Kamiyama, T.; Kato, Y.; Hama, S.; Kawamoto, K.; Mitsui, A. A lithium superionic conductor. *Nat. Mater.* **2011**, *10*, 682−686.
(15) Kato, Y.; Hori, S.; Saito, T.; Suzuki, K.; Hirayama, M.; Mitsui, A.; Yonemura, M.; Iba, H.; Kanno, R. High-power all-solid-state batteries using sulfide superionic conductors. *Nat. Energy* **2016**, *1*, 16030.
(16) Hayashi, A.; Noi, K.; Sakuda, A.; Tatsumisago, M. Superionic glass-ceramic electrolytes for room-temperature rechargeable sodium batteries. *Nat. Commun.* **2012**, *3*, 856.
(17) Radin, M. D.; Hy, S.; Sina, M.; Fang, C.; Liu, H.; Vinckeviciute, J.; Zhang, M.; Whittingham, M. S.; Meng, Y. S.; Van der Ven, A. Narrowing the Gap between Theoretical and Practical Capacities in Li-Ion Layered Oxide Cathode Materials. *Adv. Energy Mater.* **2017**, *7*, 1602888.
(18) Wagemaker, M.; Mulder, F. M.; Van der Ven, A. The role of surface and interface energy on phase stability of nanosized insertion compounds. *Adv. Mater.* **2009**, *21*, 2703−2709.
(19) Van der Ven, A.; Wagemaker, M. Effect of surface energies and nano-particle size distribution on open circuit voltage of Li-electrodes. *Electrochem. Commun.* **2009**, *11*, 881−884.
(20) Padhi, A.; Nanjundaswamya, K.; Goodenough, J. Phospho-olivines as Positive-Electrode Materials for Rechargeable Lithium Batteries. *J. Electrochem. Soc.* **1997**, *144*, 1188−1194.
(21) Reimers, J. N.; Dahn, J. Electrochemical and in situ X-ray diffraction studies of lithium intercalation in Li x CoO2. *J. Electrochem. Soc.* **1992**, *139*, 2091−2097.
(22) Ohzuku, T.; Ueda, A. Solid-state redox reactions of LiCoO2 (R3m) for 4 V secondary lithium cells. *J. Electrochem. Soc.* **1994**, *141*, 2972−2977.
(23) Amatucci, G.; Tarascon, J.; Klein, L. CoO2, the end member of the Li x CoO2 solid solution. *J. Electrochem. Soc.* **1996**, *143*, 1114−1123.
(24) Thackeray, M.; David, W.; Bruce, P.; Goodenough, J. B. Lithium insertion into manganese spinels. *Mater. Res. Bull.* **1983**, *18*, 461−472.
(25) Thackeray, M. M. Manganese oxides for lithium batteries. *Prog. Solid State Chem.* **1997**, *25*, 1−71.
(26) Delmas, C.; Fouassier, C.; Hagenmuller, P. Structural classification and properties of the layered oxides. *Physica B+C* **1980**, *99*, 81−85.
(27) Van der Ven, A.; Aydinol, M. K.; Ceder, G. First-Principles Evidence for Stage Ordering in Li x CoO2. *J. Electrochem. Soc.* **1998**, *145*, 2149−2155.
(28) Chen, Z.; Lu, Z.; Dahn, J. Staging phase transitions in Li x CoO2. *J. Electrochem. Soc.* **2002**, *149*, A1604−A1609.
(29) Yu, H.-C.; Ling, C.; Bhattacharya, J.; Thomas, J. C.; Thornton, K.; Van der Ven, A. Designing the next generation high capacity battery electrodes. *Energy Environ. Sci.* **2014**, *7*, 1760.
(30) Newman, J.; Thomas-Alyea, K. E. *Electrochemical Systems*; John Wiley & Sons, 2012.
(31) Bard, A. J.; Faulkner, L. R. *Electrochemical Methods: Fundamentals and Applications*, 2nd ed.; John Wiley & Sons, 2001.
(32) Voorhees, P. W.; Johnson, W. C. The thermodynamics of elastically stressed crystals. *Solid State Phys.* **2004**, *59*, 1−201.
(33) Ganser, M.; Hildebrand, F. E.; Klinsmann, M.; Hanauer, M.; Kamlah, M.; McMeeking, R. M. An Extended Formulation of Butler-Volmer Electrochemical Reaction Kinetics Including the Influence of Mechanics. *J. Electrochem. Soc.* **2019**, *166*, H167−H176.
(34) Xu, K. Electrolytes and Interphases in Li-Ion Batteries and Beyond. *Chem. Rev.* **2014**, *114*, 11503−11618.
(35) Pinson, M. B.; Bazant, M. Z. Theory of SEI formation in rechargeable batteries: capacity fade, accelerated aging and lifetime prediction. *J. Electrochem. Soc.* **2013**, *160*, A243−A250.
(36) Swift, M. W.; Qi, Y. First-principles prediction of potentials and space-charge layers in all-solid-state batteries. *Phys. Rev. Lett.* **2019**, *122*, 167701.
(37) Maier, J. Ionic conduction in space charge regions. *Prog. Solid State Chem.* **1995**, *23*, 171−263.

https://dx.doi.org/10.1021/acs.chemrev.9b00601
Chem. Rev. 2020, 120, 6977−7019

(38) Maier, J. Nanoionics: ion transport and electrochemical storage in confined systems. *Nat. Mater.* **2005**, *4*, 805.
(39) Bazant, M. Z. Theory of chemical kinetics and charge transfer based on nonequilibrium thermodynamics. *Acc. Chem. Res.* **2013**, *46*, 1144−1160.
(40) Zeng, Y.; Smith, R. B.; Bai, P.; Bazant, M. Z. Simple formula for Marcus−Hush−Chidsey kinetics. *J. Electroanal. Chem.* **2014**, *735*, 77−83.
(41) Bai, P.; Bazant, M. Z. Charge transfer kinetics at the solidsolid interface in porous electrodes. *Nat. Commun.* **2014**, *5*, 3585.
(42) de Groot, S. R.; Mazur, P. *Non-equilibrium thermodynamics*; Dover Publications, 1984.
(43) Mazenko, G.*Nonequilibrium Statistical Mechanics*; Wiley-VCH, 2006.
(44) Allnatt, A. R. Einstein and linear response formulae for the phenomenological coefficients for isothermal matter transport in solids. *J. Phys. C: Solid State Phys.* **1982**, *15*, 5605.
(45) Allnatt, A. R.; Lidiard, A. B. *Atomic Transport in Solids*; Cambridge University Press: Cambridge, UK, 1993.
(46) Van der Ven, A.; Thomas, J. C.; Puchala, B.; Natarajan, A. R. First-principles statistical mechanics of multicomponent crystals. *Annu. Rev. Mater. Res.* **2018**, *48*, 27−55.
(47) Vineyard, G. H. Frequency factors and isotope effects in solid state rate processes. *J. Phys. Chem. Solids* **1957**, *3*, 121−127.
(48) Van der Ven, A.; Thomas, J. C.; Xu, Q.; Swoboda, B.; Morgan, D. Nondilute diffusion from first principles: Li diffusion in Li x TiS 2. *Phys. Rev. B: Condens. Matter Mater. Phys.* **2008**, *78*, 104306.
(49) Gomer, R. Diffusion of adsorbates on metal surfaces. *Rep. Prog. Phys.* **1990**, *53*, 917.
(50) Van der Ven, A.; Ceder, G. Lithium diffusion in layered Li x CoO2. *Electrochem. Solid-State Lett.* **1999**, *3*, 301−304.
(51) Van der Ven, A.; Ceder, G.; Asta, M.; Tepesch, P. D. First-principles theory of ionic diffusion with nondilute carriers. *Phys. Rev. B: Condens. Matter Mater. Phys.* **2001**, *64*, 184307.
(52) Murch, G. The Haven ratio in fast ionic conductors. *Solid State Ionics* **1982**, *7*, 177−198.
(53) Kutner, R. Chemical diffusion in the lattice gas of non-interacting particles. *Phys. Lett. A* **1981**, *81*, 239−240.
(54) Wang, J.; Raistrick, I.; Huggins, R. A. Behavior of some binary lithium alloys as negative electrodes in organic solvent-based electrolytes. *J. Electrochem. Soc.* **1986**, *133*, 457−460.
(55) Wen, C. J.; Huggins, R. A. Chemical diffusion in intermediate phases in the lithium-silicon system. *J. Solid State Chem.* **1981**, *37*, 271−278.
(56) Van der Ven, A.; Yu, H.-C.; Ceder, G.; Thornton, K. Vacancy mediated substitutional diffusion in binary crystalline solids. *Prog. Mater. Sci.* **2010**, *55*, 61−105.
(57) Van der Ven, A.; Ceder, G. First Principles Calculation of the Interdiffusion Coefficient in Binary Alloys. *Phys. Rev. Lett.* **2005**, *94*, No. 045901.
(58) Goiri, J. G.; Kolli, S. K.; Van der Ven, A. Role of short-and long-range ordering on diffusion in Ni-Al alloys. *Physical Review Materials* **2019**, *3*, No. 093402.
(59) Malik, R.; Abdellahi, A.; Ceder, G. A critical review of the Li insertion mechanisms in LiFePO4 electrodes. *J. Electrochem. Soc.* **2013**, *160*, A3179−A3197.
(60) Marcus, R. A. Electron transfer reactions in chemistry. Theory and experiment. *Rev. Mod. Phys.* **1993**, *65*, 599.
(61) Newton, M. D. Quantum chemical probes of electron-transfer kinetics: the nature of donor-acceptor interactions. *Chem. Rev.* **1991**, *91*, 767−792.
(62) Ohzuku, T.; Ueda, A.; Yamamoto, N. Zero-strain insertion material of Li [Li1/3Ti5/3] O 4 for rechargeable lithium cells. *J. Electrochem. Soc.* **1995**, *142*, 1431−1435.
(63) Cahn, J. W. On spinodal decomposition. *Acta Metall.* **1961**, *9*, 795−801.
(64) Cahn, J. W. Phase Separation by Spinodal Decomposition in Isotropic Systems. *J. Chem. Phys.* **1965**, *42*, 93−99.
(65) Hilliard, J. E.*Phase Transformations*; American Society for Metals, 1970; pp 470−560.
(66) Cahn, J. W.; Hilliard, J. E. Free Energy of a Nonuniform System. I. Interfacial Free Energy. *J. Chem. Phys.* **1958**, *28*, 258−267.
(67) Cahn, J. W.; Hilliard, J. E. Free Energy of a Nonuniform System. III. Nucleation in a Two-Component Incompressible Fluid. *J. Chem. Phys.* **1959**, *31*, 688−699.
(68) Vasileiadis, A.; de Klerk, N. J.; Smith, R. B.; Ganapathy, S.; Harks, P. P. R.; Bazant, M. Z.; Wagemaker, M. Toward Optimal Performance and In-Depth Understanding of Spinel Li4Ti5O12 Electrodes through Phase Field Modeling. *Adv. Funct. Mater.* **2018**, *28*, 1705992.
(69) Ganapathy, S.; Vasileiadis, A.; Heringa, J. R.; Wagemaker, M. The Fine Line between a Two-Phase and Solid-Solution Phase Transformation and Highly Mobile Phase Interfaces in Spinel Li4+ xTi5O12. *Adv. Energy Mater.* **2017**, *7*, 1601781.
(70) Bohn, E.; Eckl, T.; Kamlah, M.; McMeeking, R. A model for lithium diffusion and stress generation in an intercalation storage particle with phase change. *J. Electrochem. Soc.* **2013**, *160*, A1638−A1652.
(71) Van der Ven, A.; Garikipati, K.; Kim, S.; Wagemaker, M. The role of coherency strains on phase stability in Li x FePO4: needle crystallites minimize coherency strain and overpotential. *J. Electrochem. Soc.* **2009**, *156*, A949−A957.
(72) Chen, G.; Song, X.; Richardson, T. J. Electron microscopy study of the LiFePO4 to FePO4 phase transition. *Electrochem. Solid-State Lett.* **2006**, *9*, A295−A298.
(73) Cahn, J. W. Coherent fluctuations and nucleation in isotropic solids. *Acta Metall.* **1962**, *10*, 907−913.
(74) Thomas, J. C.; Van der Ven, A. The exploration of nonlinear elasticity and its efficient parameterization for crystalline materials. *J. Mech. Phys. Solids* **2017**, *107*, 76−95.
(75) Khachaturyan, A. G.*Theory of Structural Transformations in Solids*; Dover Publications, 2008.
(76) Meethong, N.; Huang, H.; Speakman, S. A.; Carter, W. C.; Chiang, Y. Strain accommodation during phase transformations in olivine-based cathodes as a materials selection criterion for high-power rechargeable batteries. *Adv. Funct. Mater.* **2007**, *17*, 1115−1123.
(77) Tang, M.; Carter, W. C.; Chiang, Y.-M. Electrochemically driven phase transitions in insertion electrodes for lithium-ion batteries: examples in lithium metal phosphate olivines. *Annu. Rev. Mater. Res.* **2010**, *40*, 501−529.
(78) Cogswell, D. A.; Bazant, M. Z. Coherency strain and the kinetics of phase separation in LiFePO4 nanoparticles. *ACS Nano* **2012**, *6*, 2215−2225.
(79) Morgan, D.; Van der Ven, A.; Ceder, G. Li conductivity in Li x MPO 4 (M= Mn, Fe, Co, Ni) olivine materials. *Electrochem. Solid-State Lett.* **2004**, *7*, A30−A32.
(80) Islam, M. S.; Driscoll, D. J.; Fisher, C. A.; Slater, P. R. Atomic-scale investigation of defects, dopants, and lithium transport in the LiFePO4 olivine-type battery material. *Chem. Mater.* **2005**, *17*, 5085−5092.
(81) Srinivasan, V.; Newman, J. Discharge model for the lithium iron-phosphate electrode. *J. Electrochem. Soc.* **2004**, *151*, A1517−A1529.
(82) Han, B.; Van der Ven, A.; Morgan, D.; Ceder, G. Electrochemical modeling of intercalation processes with phase field models. *Electrochim. Acta* **2004**, *49*, 4691−4699.
(83) Singh, G. K.; Ceder, G.; Bazant, M. Z. Intercalation dynamics in rechargeable battery materials: General theory and phase-transformation waves in LiFePO4. *Electrochim. Acta* **2008**, *53*, 7599−7613.
(84) Bai, P.; Cogswell, D. A.; Bazant, M. Z. Suppression of phase separation in LiFePO4 nanoparticles during battery discharge. *Nano Lett.* **2011**, *11*, 4890−4896.
(85) Malik, R.; Zhou, F.; Ceder, G. Kinetics of non-equilibrium lithium incorporation in LiFePO4. *Nat. Mater.* **2011**, *10*, 587−590.
(86) Rudraraju, S.; Van der Ven, A.; Garikipati, K. Mechanochemical spinodal decomposition: a phenomenological theory of phase transformations in muli-component, crystalline solids. *Npj Comput. Mater.* **2016**, *2*, 16012.

https://dx.doi.org/10.1021/acs.chemrev.9b00601
Chem. Rev. 2020, 120, 6977−7019

(87) Dahn, J. Phase diagram of Li x C 6. *Phys. Rev. B: Condens. Matter Mater. Phys.* **1991**, *44*, 9170.
(88) Yabuuchi, N.; Kubota, K.; Dahbi, M.; Komaba, S. Research development on sodium-ion batteries. *Chem. Rev.* **2014**, *114*, 11636−11682.
(89) Gabrisch, H.; Yazami, R.; Fultz, B. The character of dislocations in LiCoO2. *Electrochem. Solid-State Lett.* **2002**, *5*, A111−A114.
(90) Kaufman, J. L.; Vinckevičiūte, J.; Krishna Kolli, S.; Gabriel Goiri, J.; Van der Ven, A. Understanding intercalation compounds for sodium-ion batteries and beyond. *Philos. Trans. R. Soc., A* **2019**, *377*, 20190020.
(91) Radin, M. D.; Alvarado, J.; Meng, Y. S.; Van der Ven, A. Role of Crystal Symmetry in the Reversibility of Stacking-Sequence Changes in Layered Intercalation Electrodes. *Nano Lett.* **2017**, *17*, 7789−7795.
(92) Courtney, I. A.; Dahn, J. Electrochemical and in situ X-ray diffraction studies of the reaction of lithium with tin oxide composites. *J. Electrochem. Soc.* **1997**, *144*, 2045−2052.
(93) Chen, L.-Q. Phase-Field Models for Microstructure Evolution. *Annu. Rev. Mater. Res.* **2002**, *32*, 113−140.
(94) Gibou, F.; Fedkiw, R.; Osher, S. A review of level-set methods and some recent applications. *J. Comput. Phys.* **2018**, *353*, 82−109.
(95) Klinsmann, M.; Rosato, D.; Kamlah, M.; McMeeking, R. M. An assessment of the phase field formulation for crack growth. *Computer Methods in Applied Mechanics and Engineering* **2015**, *294*, 313−330.
(96) Klinsmann, M.; Rosato, D.; Kamlah, M.; McMeeking, R. M. Modeling crack growth during Li insertion in storage particles using a fracture phase field approach. *J. Mech. Phys. Solids* **2016**, *92*, 313−344.
(97) Klinsmann, M.; Rosato, D.; Kamlah, M.; McMeeking, R. M. Modeling crack growth during Li extraction in storage particles using a fracture phase field approach. *J. Electrochem. Soc.* **2016**, *163*, A102−A118.
(98) Martin, R. M.*Electronic Structure: Basic Theory and Practical Methods*; Cambridge University Press: Cambridge, UK, 2004; Vol. *1*.
(99) Zhou, F.; Cococcioni, M.; Marianetti, C. A.; Morgan, D.; Ceder, G. First-principles prediction of redox potentials in transition-metal compounds with LDA+U. *Phys. Rev. B: Condens. Matter Mater. Phys.* **2004**, *70*, 235121.
(100) Wang, L.; Maxisch, T.; Ceder, G. Oxidation energies of transition metal oxides within the GGA+U framework. *Phys. Rev. B: Condens. Matter Mater. Phys.* **2006**, *73*, 195107.
(101) Heyd, J.; Scuseria, G. E.; Ernzerhof, M. Hybrid functionals based on a screened Coulomb potential" [J. Chem. Phys. 118, 8207 (2003)]. *J. Chem. Phys.* **2003**, *118*, 8207.
(102) Heyd, J.; Scuseria, G. E.; Ernzerhof, M. Erratum_ "Hybrid functionals based on a screened Coulomb potential" [J. Chem. Phys. 118, 8207 (2003)]. *J. Chem. Phys.* **2006**, *124*, 219906.
(103) Chevrier, V. L.; Ong, S. P.; Armiento, R.; Chan, M. K. Y.; Ceder, G. Hybrid density functional calculations of redox potentials and formation energies of transition metal compounds. *Phys. Rev. B: Condens. Matter Mater. Phys.* **2010**, *82*, No. 075122.
(104) Perdew, J. P.; Ruzsinszky, A.; Csonka, G. I.; Vydrov, O. A.; Scuseria, G. E.; Constantin, L. A.; Zhou, X.; Burke, K. Restoring the Density-Gradient Expansion for Exchange in Solids and Surfaces. *Phys. Rev. Lett.* **2008**, *100*, 136406.
(105) Sun, J.; Remsing, R. C.; Zhang, Y.; Sun, Z.; Ruzsinszky, A.; Peng, H.; Yang, Z.; Paul, A.; Waghmare, U.; Wu, X.; Klein, M. L.; Perdew, J. P. SCAN: An Efficient Density Functional Yielding Accurate Structures and Energies of Diversely-Bonded Materials. *arXiv:1511.01089*; Cornell University, 2015; 1 https://arxiv.org/abs/1511.01089.
(106) Aryasetiawan, F.; Gunnarsson, O. The GW method. *Rep. Prog. Phys.* **1998**, *61*, 237−312.
(107) Klimeš, J.; Bowler, D.; Michaelides, A. Van der Waals density functionals applied to solids. *Phys. Rev. B: Condens. Matter Mater. Phys.* **2011**, *83*, 195131.
(108) Lee, K.; Murray, E.; Kong, L.; Lundqvist, B.; Langreth, D. Higher-accuracy van der Waals density functional. *Phys. Rev. B: Condens. Matter Mater. Phys.* **2010**, *82*, 081101.
(109) Aydinol, M. K.; Kohan, A. F.; Ceder, G.; Cho, K.; Joannopoulos, J. Ab initio study of lithium intercalation in metal oxides and metal dichalcogenides. *Phys. Rev. B: Condens. Matter Mater. Phys.* **1997**, *56*, 1354−1365.
(110) Jaynes, E. T. Information theory and statistical mechanics. *Phys. Rev.* **1957**, *106*, 620.
(111) Zhou, F.; Maxisch, T.; Ceder, G. Configurational Electronic Entropy and the Phase Diagram of Mixed-Valence Oxides: The Case of Li_xFePO_4. *Phys. Rev. Lett.* **2006**, *97*, 155704.
(112) Wallace, D. C.*Thermodynamics of Crystals*; Courier Corporation, 1998.
(113) Ashcroft, N. W.; Mermin, N. D. *Solid State Physics*; Holt, Rinehart and Winston, 1976.
(114) Sanchez, J.; Ducastelle, F.; Gratias, D. Generalized cluster description of multicomponent systems. *Phys. A* **1984**, *128*, 334−350.
(115) De Fontaine, D. Cluster approach to order-disorder transformations in alloys. *Solid State Phys.* **1994**, *47*, 33−176.
(116) Sanchez, J. M. Cluster expansion and the configurational theory of alloys. *Phys. Rev. B: Condens. Matter Mater. Phys.* **2010**, *81*, 224202.
(117) van de Walle, A.; Ceder, G. Automating first-principles phase diagram calculations. *J. Phase Equilib.* **2002**, *23*, 348.
(118) Hart, G. L. W.; Blum, V.; Walorski, M. J.; Zunger, A. Evolutionary approach for determining first-principles hamiltonians. *Nat. Mater.* **2005**, *4*, 391−394.
(119) Mueller, T.; Ceder, G. Bayesian approach to cluster expansions. *Phys. Rev. B: Condens. Matter Mater. Phys.* **2009**, *80*, No. 024103.
(120) Kristensen, J.; Zabaras, N. J. Bayesian uncertainty quantification in the evaluation of alloy properties with the cluster expansion method. *Comput. Phys. Commun.* **2014**, *185*, 2885−2892.
(121) Landau, D. P.; Binder, K. *A Guide to Monte Carlo Simulations in Statistical Physics*; Cambridge University Press: Cambridge, UK, 2014.
(122) van de Walle, A.; Asta, M. Self-driven lattice-model Monte Carlo simulations of alloy thermodynamic properties and phase diagrams. *Modelling Simul. Mater. Sci. Eng.* **2002**, *10*, 521−538.
(123) Dalton, A. S.; Belak, A. A.; Van der Ven, A. Thermodynamics of Lithium in TiO_2 (B) from First Principles. *Chem. Mater.* **2012**, *24*, 1568−1574.
(124) Natarajan, A. R.; Thomas, J. C.; Puchala, B.; Van der Ven, A. Symmetry-adapted order parameters and free energies for solids undergoing order-disorder phase transitions. *Phys. Rev. B: Condens. Matter Mater. Phys.* **2017**, *96*, 134204.
(125) Jonsson, H.; Mills, G.; Jacobsen, K. W. *Nudged Elastic Band Method for Finding Minimum Energy Paths of Transitions*; World Scientific Publishing Co. Pte. Ltd.: Singapore, 1998.
(126) Henkelman, G.; Uberuaga, B. P.; Jonsson, H. A climbing image nudged elastic band method for finding saddle points and minimum energy paths. *J. Chem. Phys.* **2000**, *113*, 9901.
(127) Bortz, A. B.; Kalos, M. H.; Lebowitz, J. L. A new algorithm for Monte Carlo simulation of Ising spin systems. *J. Comput. Phys.* **1975**, *17*, 10−18.
(128) Bulnes, F.; Pereyra, V.; Riccardo, J. Collective surface diffusion: n-fold way kinetic Monte Carlo simulation. *Phys. Rev. E: Stat. Phys., Plasmas, Fluids, Relat. Interdiscip. Top.* **1998**, *58*, 86.
(129) Barnett, R. N.; Landman, U. Born-Oppenheimer molecular-dynamics simulations of finite systems: Structure and dynamics of $(H_2O)_2$. *Phys. Rev. B: Condens. Matter Mater. Phys.* **1993**, *48*, 2081−2097.
(130) Car, R.; Parrinello, M. Unified Approach for Molecular Dynamics and Density-Functional Theory. *Phys. Rev. Lett.* **1985**, *55*, 2471−2474.
(131) Jones, J. E. On the Determination of Molecular Fields. II. From the Equation of State of a Gas. *Proc. R. Soc. London, Ser. A* **1924**, *106*, 463−477.
(132) Buckingham, R. A. The classical equation of state of gaseous helium, neon and argon. *Proc. R. Soc. London Ser. Math. Phys. Sci.* **1938**, *168*, 264−283.
(133) Daw, M. S.; Baskes, M. I. Embedded-atom method: Derivation and application to impurities, surfaces, and other defects in metals. *Phys. Rev. B: Condens. Matter Mater. Phys.* **1984**, *29*, 6443−6453.

https://dx.doi.org/10.1021/acs.chemrev.9b00601
Chem. Rev. 2020, 120, 6977−7019

(134) Behler, J.; Parrinello, M. Generalized Neural-Network Representation of High-Dimensional Potential-Energy Surfaces. *Phys. Rev. Lett.* **2007**, *98*, 146401.
(135) Novoselov, I.; Yanilkin, A.; Shapeev, A.; Podryabinkin, E. Moment tensor potentials as a promising tool to study diffusion processes. *Comput. Mater. Sci.* **2019**, *164*, 46−56.
(136) Shapeev, A. V. Moment Tensor Potentials: A Class of Systematically Improvable Interatomic Potentials. *Multiscale Model. Simul.* **2016**, *14*, 1153−1173.
(137) Bartók, A. P.; Payne, M. C.; Kondor, R.; Csányi, G. Gaussian Approximation Potentials: The Accuracy of Quantum Mechanics, without the Electrons. *Phys. Rev. Lett.* **2010**, *104*, 136403.
(138) Bartók, A. P.; Kondor, R.; Csányi, G. On representing chemical environments. *Phys. Rev. B: Condens. Matter Mater. Phys.* **2013**, *87*, 184115.
(139) Wood, M. A.; Thompson, A. P. Extending the accuracy of the SNAP interatomic potential form. *J. Chem. Phys.* **2018**, *148*, 241721.
(140) Wood, M. A.; Thompson, A. P. Quantum-Accurate Molecular Dynamics Potential for Tungsten, *arXiv.1702.07042*; Cornell University, 2017; 1, https://arxiv.org/abs/1702.07042.
(141) Thompson, A. P.; Swiler, L. P.; Trott, C. R.; Foiles, S. M.; Tucker, G. J. Spectral neighbor analysis method for automated generation of quantum-accurate interatomic potentials. *J. Comput. Phys.* **2015**, *285*, 316−330.
(142) Deng, Z.; Chen, C.; Li, X.-G.; Ong, S. P. An electrostatic spectral neighbor analysis potential for lithium nitride. *npj Comput. Mater.* **2019**, *5*, 75.
(143) Li, X.-G.; Hu, C.; Chen, C.; Deng, Z.; Luo, J.; Ong, S. P. Quantum-accurate spectral neighbor analysis potential models for Ni-Mo binary alloys and fcc metals. *Phys. Rev. B: Condens. Matter Mater. Phys.* **2018**, *98*, No. 094104.
(144) Chen, C.; Deng, Z.; Tran, R.; Tang, H.; Chu, I.-H.; Ong, S. P. Accurate force field for molybdenum by machine learning large materials data. *Phys. Rev. Mater.* **2017**, *1*, No. 043603.
(145) Zuo, Y.; Chen, C.; Li, X.; Deng, Z.; Chen, Y.; Behler, J.; Csányi, G.; Shapeev, A. V.; Thompson, A. P.; Wood, M. A.; Ong, S. P. A Performance and Cost Assessment of Machine Learning Interatomic Potentials *J. Phys. Chem A* **2019**; DOI: 10.1021/acs.jpca.9b08723.
(146) Leung, K. Predicting the voltage dependence of interfacial electrochemical processes at lithium-intercalated graphite edge planes. *Phys. Chem. Chem. Phys.* **2015**, *17*, 1637−1643.
(147) Leung, K. Electronic Structure Modeling of Electrochemical Reactions at Electrode/Electrolyte Interfaces in Lithium Ion Batteries. *J. Phys. Chem. C* **2013**, *117*, 1539−1547.
(148) Leung, K. First-Principles Modeling of the Initial Stages of Organic Solvent Decomposition on Li x Mn 2 O 4 (100) Surfaces. *J. Phys. Chem. C* **2012**, *116*, 9852−9861.
(149) Tang, H.; Deng, Z.; Lin, Z.; Wang, Z.; Chu, I.-H.; Chen, C.; Zhu, Z.; Zheng, C.; Ong, S. P. Probing Solid-Solid Interfacial Reactions in All-Solid-State Sodium-ion Batteries with First Principles Calculations. *Chem. Mater.* **2018**, *30*, 163−173.
(150) Hautier, G.; Jain, A.; Ong, S. P.; Kang, B.; Moore, C.; Doe, R.; Ceder, G. Phosphates as Lithium-Ion Battery Cathodes: An Evaluation Based on High-Throughput ab Initio Calculations. *Chem. Mater.* **2011**, *23*, 3495−3508.
(151) Jain, A.; Hautier, G.; Moore, C.; Kang, B.; Lee, J.; Chen, H.; Twu, N.; Ceder, G. A Computational Investigation of $Li_9 M_3(P_2 O_7)_3 (PO_4)_2$ (M = V, Mo) as Cathodes for Li Ion Batteries. *J. Electrochem. Soc.* **2012**, *159*, A622−A633.
(152) Qu, X.; Jain, A.; Rajput, N. N.; Cheng, L.; Zhang, Y.; Ong, S. P.; Brafman, M.; Maginn, E.; Curtiss, L. A.; Persson, K. A. The Electrolyte Genome project: A big data approach in battery materials discovery. *Comput. Mater. Sci.* **2015**, *103*, 56−67.
(153) Cheng, L.; Assary, R. S.; Qu, X.; Jain, A.; Ong, S. P.; Rajput, N. N.; Persson, K.; Curtiss, L. A. Accelerating Electrolyte Discovery for Energy Storage with High-Throughput Screening. *J. Phys. Chem. Lett.* **2015**, *6*, 283−291.
(154) Borodin, O.; Olguin, M.; Spear, C. E.; Leiter, K. W.; Knap, J. Towards high throughput screening of electrochemical stability of battery electrolytes. *Nanotechnology* **2015**, *26*, 354003.
(155) Mathew, K.; et al. Atomate: A high-level interface to generate, execute, and analyze computational materials science workflows. *Comput. Mater. Sci.* **2017**, *139*, 140−152.
(156) Makeev, M. A.; Rajput, N. N. Computational screening of electrolyte materials: status quo and open problems. *Curr. Opin. Chem. Eng.* **2019**, *23*, 58−69.
(157) Van der Ven, A.; Aydinol, M. K.; Ceder, G.; Kresse, G.; Hafner, J. First-principles investigation of phase stability in Li x CoO 2. *Phys. Rev. B: Condens. Matter Mater. Phys.* **1998**, *58*, 2975−2987.
(158) Wolverton, C.; Zunger, A. First-principles prediction of vacancy order-disorder and intercalation battery voltages in Li x CoO 2. *Phys. Rev. Lett.* **1998**, *81*, 606.
(159) Arroyo y de Dompablo, M. E.; Van der Ven, A.; Ceder, G. First-principles calculations of lithium ordering and phase stability on Li x NiO 2. *Phys. Rev. B: Condens. Matter Mater. Phys.* **2002**, *66*, No. 064112.
(160) Van der Ven, A.; Ceder, G. Ordering in Lix (Ni0. 5Mn0. 5) O2 and its relation to charge capacity and electrochemical behavior in rechargeable lithium batteries. *Electrochem. Commun.* **2004**, *6*, 1045−1050.
(161) Carlier, D.; Van der Ven, A.; Delmas, C.; Ceder, G. First-principles investigation of phase stability in the O2-$LiCoO_2$ system. *Chem. Mater.* **2003**, *15*, 2651−2660.
(162) Bhattacharya, J.; Van der Ven, A. First-principles study of competing mechanisms of nondilute Li diffusion in spinel $Li_x TiS_2$. *Phys. Rev. B: Condens. Matter Mater. Phys.* **2011**, *83*, 144302.
(163) Wagemaker, M.; Van Der Ven, A.; Morgan, D.; Ceder, G.; Mulder, F.; Kearley, G. Thermodynamics of spinel Li_xTiO_2 from first principles. *Chem. Phys.* **2005**, *317*, 130−136.
(164) Bhattacharya, J.; Van der Ven, A. Phase stability and nondilute Li diffusion in spinel $Li_{1+x} Ti_2 O_4$. *Phys. Rev. B: Condens. Matter Mater. Phys.* **2010**, *81*, 104304.
(165) Lee, E.; Persson, K. A. Solid-Solution Li Intercalation as a Function of Cation Order/Disorder in the High-Voltage $Li_x Ni_{0.5} Mn_{1.5} O_4$ Spinel. *Chem. Mater.* **2013**, *25*, 2885−2889.
(166) Hao, S.; Lu, Z.; Wolverton, C. Quaternary phase diagrams of spinel $Li_{y\ 1-y} Mn_x Ni_{2-x} O_4$ and composite cathode voltages for concentration gradient materials. *Phys. Rev. B: Condens. Matter Mater. Phys.* **2016**, *94*, No. 014114.
(167) Belak, A. A.; Wang, Y.; Van der Ven, A. Kinetics of Anatase Electrodes: The Role of Ordering, Anisotropy, and Shape Memory Effects. *Chem. Mater.* **2012**, *24*, 2894−2898.
(168) Meng, Y. S.; Hinuma, Y.; Ceder, G. An investigation of the sodium patterning in NaxCoO2 (0.5 × 1) by density functional theory methods. *J. Chem. Phys.* **2008**, *128*, 104708.
(169) Hinuma, Y.; Meng, Y. S.; Ceder, G. Temperature-concentration phase diagram of *P* 2 -$Na_x CoO_2$ from first-principles calculations. *Phys. Rev. B: Condens. Matter Mater. Phys.* **2008**, *77*, 224111.
(170) Kaufman, J. L.; Van der Ven, A. $Na_x CoO_2$ phase stability and hierarchical orderings in the O3/P3 structure family. *Phys. Rev. Materials* **2019**, *3*, No. 015402.
(171) Toriyama, M. Y.; Kaufman, J. L.; Van der Ven, A. Potassium Ordering and Structural Phase Stability in Layered $K_x CoO_2$. *ACS Appl. Energy Mater.* **2019**, *2*, 2629−2636.
(172) Emly, A.; Van der Ven, A. Mg intercalation in layered and spinel host crystal structures for Mg batteries. *Inorg. Chem.* **2015**, *54*, 4394−4402.
(173) Chen, T.; Sai Gautam, G.; Huang, W.; Ceder, G. First-Principles Study of the Voltage Profile and Mobility of Mg Intercalation in a Chromium Oxide Spinel. *Chem. Mater.* **2018**, *30*, 153−162.
(174) Kolli, S. K.; Van der Ven, A. Controlling the electrochemical properties of spinel intercalation compounds. *ACS Applied Energy Materials* **2018**, *1*, 6833−6839.
(175) Vinckevičiutė, J.; Radin, M. D.; Van der Ven, A. Stacking-Sequence Changes and Na Ordering in Layered Intercalation Materials. *Chem. Mater.* **2016**, *28*, 8640−8650.

(176) Thompson, A. H. Electrochemical Potential Spectroscopy: A New Electrochemical Measurement. *J. Electrochem. Soc.* **1979**, *126*, 608.
(177) Winn, D. A.; Shemilt, J. M.; Steele, B. C. H. Titanium Disulphide: A Solid Solution Electrode for Sodium and Lithium. *Mater. Res. Bull.* **1976**, *11*, 559−566.
(178) Kubota, K.; Asari, T.; Yoshida, H.; Yaabuuchi, N.; Shiiba, H.; Nakayama, M.; Komaba, S. Understanding the Structural Evolution and Redox Mechanism of a $NaFeO_2$ -$NaCoO_2$ Solid Solution for Sodium-Ion Batteries. *Adv. Funct. Mater.* **2016**, *26*, 6047−6059.
(179) Bonnick, P.; Sun, X.; Lau, K.-C.; Liao, C.; Nazar, L. F. Monovalent versus Divalent Cation Diffusion in Thiospinel Ti_2S_4. *J. Phys. Chem. Lett.* **2017**, *8*, 2253−2257.
(180) Radin, M. D.; Van der Ven, A. Simulating Charge, Spin, and Orbital Ordering: Application to Jahn−Teller Distortions in Layered Transition-Metal Oxides. *Chem. Mater.* **2018**, *30*, 607−618.
(181) Hibma, T. X-ray study of the ordering of the alkali ions in the intercalation compounds Na_xTiS_2 and Li_xTiS_2. *J. Solid State Chem.* **1980**, *34*, 97−106.
(182) Hibma, T. Ordering of the alkali-ions in Na_xTiS_2 and Li_xTiS_2. *Physica B+C* **1980**, *99*, 136−140.
(183) Radin, M. D.; Van der Ven, A. Stability of prismatic and octahedral coordination in layered oxides and sulfides intercalated with alkali and alkaline-earth metals. *Chem. Mater.* **2016**, *28*, 7898−7904.
(184) Berthelot, R.; Carlier, D.; Delmas, C. Electrochemical investigation of the P2−Na_x CoO_2 phase diagram. *Nat. Mater.* **2011**, *10*, 74.
(185) Komaba, S.; Murata, W.; Ishikawa, T.; Yabuuchi, N.; Ozeki, T.; Nakayama, T.; Ogata, A.; Gotoh, K.; Fujiwara, K. Electrochemical Na Insertion and Solid Electrolyte Interphase for Hard-Carbon Electrodes and Application to Na-Ion Batteries. *Adv. Funct. Mater.* **2011**, *21*, 3859−3867.
(186) Yabuuchi, N.; Kajiyama, M.; Iwatate, J.; Nishikawa, H.; Hitomi, S.; Okuyama, R.; Usui, R.; Yamada, Y.; Komaba, S. P2-type $Na_x[Fe_{1/2}Mn_{1/2}]O_2$ made from earth-abundant elements for rechargeable Na batteries. *Nat. Mater.* **2012**, *11*, 512−517.
(187) Zheng, C.; Radhakrishnan, B.; Chu, I.-H.; Wang, Z.; Ong, S. P. Effects of Transition-Metal Mixing on Na Ordering and Kinetics in Layered P 2 Oxides. *Phys. Rev. Appl.* **2017**, *7*, No. 064003.
(188) Wang, X.; Tamaru, M.; Okubo, M.; Yamada, A. Electrode Properties of P2−$Na_{2/3}$ Mn_y Co_{1y} O_2 as Cathode Materials for Sodium-Ion Batteries. *J. Phys. Chem. C* **2013**, *117*, 15545−15551.
(189) Van der Ven, A.; Bhattacharya, J.; Belak, A. A. Understanding Li Diffusion in Li-Intercalation Compounds. *Acc. Chem. Res.* **2013**, *46*, 1216−1225.
(190) Lee, J.; Urban, A.; Li, X.; Su, D.; Hautier, G.; Ceder, G. Unlocking the Potential of Cation-Disordered Oxides for Rechargeable Lithium Batteries. *Science* **2014**, *343*, 519−522.
(191) Urban, A.; Lee, J.; Ceder, G. The Configurational Space of Rocksalt-Type Oxides for High-Capacity Lithium Battery Electrodes. *Adv. Energy Mater.* **2014**, *4*, 1400478.
(192) Richards, W. D.; Dacek, S. T.; Kitchaev, D. A.; Ceder, G. Fluorination of Lithium-Excess Transition Metal Oxide Cathode Materials. *Adv. Energy Mater.* **2018**, *8*, 1701533.
(193) Kitchaev, D. A.; Lun, Z.; Richards, W. D.; Ji, H.; Clément, R. J.; Balasubramanian, M.; Kwon, D.-H.; Dai, K.; Papp, J. K.; Lei, T.; McCloskey, B. D.; Yang, W.; Lee, J.; Ceder, G. Design principles for high transition metal capacity in disordered rocksalt Li-ion cathodes. *Energy Environ. Sci.* **2018**, *11*, 2159−2171.
(194) Maxisch, T.; Zhou, F.; Ceder, G. Ab initio study of the migration of small polarons in olivine Li $_x$ FePO $_4$ and their association with lithium ions and vacancies. *Phys. Rev. B: Condens. Matter Mater. Phys.* **2006**, *73*, 104301.
(195) Ong, S. P.; Mo, Y.; Ceder, G. Low hole polaron migration barrier in lithium peroxide. *Phys. Rev. B: Condens. Matter Mater. Phys.* **2012**, *85*, No. 081105.
(196) Xiao, P.; Henkelman, G. Kinetic Monte Carlo Study of Li Intercalation in $LiFePO_4$. *ACS Nano* **2018**, *12*, 844−851.
(197) Delacourt, C.; Poizot, P.; Tarascon, J.-M.; Masquelier, C. The existence of a temperature-driven solid solution in Li $_x$ FePO $_4$ for $0 \leq x \leq 1$. *Nat. Mater.* **2005**, *4*, 254.
(198) Dodd, J. L.; Yazami, R.; Fultz, B. Phase Diagram of Li_xFePO_4. *ECS Trans.* **2006**, *1*, 27−38.
(199) Abdellahi, A.; Akyildiz, O.; Malik, R.; Thornton, K.; Ceder, G. Particle-size and morphology dependence of the preferred interface orientation in LiFePO $_4$ nano-particles. *J. Mater. Chem. A* **2014**, *2*, 15437−15447.
(200) Liu, H.; Strobridge, F. C.; Borkiewicz, O. J.; Wiaderek, K. M.; Chapman, K. W.; Chupas, P. J.; Grey, C. P. Capturing metastable structures during high-rate cycling of $LiFePO_4$ nanoparticle electrodes. *Science* **2014**, *344*, 1252817−1252817.
(201) Saracibar, A.; Van der Ven, A.; Arroyo-de Dompablo, M. E. Crystal Structure, Energetics, And Electrochemistry of Li_2 $FeSiO_4$ Polymorphs from First Principles Calculations. *Chem. Mater.* **2012**, *24*, 495−503.
(202) Eames, C.; Armstrong, A.; Bruce, P.; Islam, M. Insights into changes in voltage and structure of Li_2FeSiO_4 polymorphs for lithium-ion batteries. *Chem. Mater.* **2012**, *24*, 2155−2161.
(203) Lin, Y.-C.; et al. Thermodynamics, Kinetics and Structural Evolution of -$LiVOPO_4$ over Multiple Lithium Intercalation. *Chem. Mater.* **2016**, *28*, 1794−1805.
(204) Lin, Y.-C.; Hidalgo, M. F. V.; Chu, I.-H.; Chernova, N. A.; Whittingham, M. S.; Ong, S. P. Comparison of the polymorphs of $VOPO_4$ as multi-electron cathodes for rechargeable alkali-ion batteries. *J. Mater. Chem. A* **2017**, *5*, 17421−17431.
(205) Persson, K.; Hinuma, Y.; Meng, Y. S.; Van der Ven, A.; Ceder, G. Thermodynamic and kinetic properties of the Li-graphite system from first-principles calculations. *Phys. Rev. B: Condens. Matter Mater. Phys.* **2010**, *82*, 125416.
(206) Persson, K.; Sethuraman, V. A.; Hardwick, L. J.; Hinuma, Y.; Meng, Y. S.; van der Ven, A.; Srinivasan, V.; Kostecki, R.; Ceder, G. Lithium Diffusion in Graphitic Carbon. *J. Phys. Chem. Lett.* **2010**, *1*, 1176−1180.
(207) Guo, Y.; Smith, R. B.; Yu, Z.; Efetov, D. K.; Wang, J.; Kim, P.; Bazant, M. Z.; Brus, L. E. Li intercalation into graphite: direct optical imaging and Cahn−Hilliard reaction dynamics. *J. Phys. Chem. Lett.* **2016**, *7*, 2151−2156.
(208) Chandesris, M.; Caliste, D.; Jamet, D.; Pochet, P. Thermodynamics and Related Kinetics of Staging in Intercalation Compounds. *J. Phys. Chem. C* **2019**, *123*, 23711−23720.
(209) Stevens, D. A.; Dahn, J. R. The Mechanisms of Lithium and Sodium Insertion in Carbon Materials. *J. Electrochem. Soc.* **2001**, *148*, A803.
(210) Chevrier, V.; Dahn, J. R. First principles model of amorphous silicon lithiation. *J. Electrochem. Soc.* **2009**, *156*, A454−A458.
(211) Chang, D.; Huo, H.; Johnston, K. E.; Ménétrier, M.; Monconduit, L.; Grey, C. P.; Van der Ven, A. Elucidating the origins of phase transformation hysteresis during electrochemical cycling of Li−Sb electrodes. *J. Mater. Chem. A* **2015**, *3*, 18928−18943.
(212) Chang, D.; Chen, M.-H.; Van der Ven, A. Factors Contributing to Path Hysteresis of Displacement and Conversion Reactions in Li Ion Batteries. *Chem. Mater.* **2015**, *27*, 7593−7600.
(213) Morris, A. J.; Needs, R.; Salager, E.; Grey, C.; Pickard, C. J. Lithiation of silicon via lithium Zintl-defect complexes from first principles. *Phys. Rev. B: Condens. Matter Mater. Phys.* **2013**, *87*, 174108.
(214) Morris, A. J.; Grey, C.; Pickard, C. J. Thermodynamically stable lithium silicides and germanides from density functional theory calculations. *Phys. Rev. B: Condens. Matter Mater. Phys.* **2014**, *90*, No. 054111.
(215) Mayo, M.; Morris, A. J. Structure Prediction of Li−Sn and Li−Sb Intermetallics for Lithium-Ion Batteries Anodes. *Chem. Mater.* **2017**, *29*, 5787−5795.
(216) Mayo, M.; Griffith, K. J.; Pickard, C. J.; Morris, A. J. Ab initio study of phosphorus anodes for lithium-and sodium-ion batteries. *Chem. Mater.* **2016**, *28*, 2011−2021.

https://dx.doi.org/10.1021/acs.chemrev.9b00601
Chem. Rev. 2020, 120, 6977−7019

(217) Johari, P.; Qi, Y.; Shenoy, V. B. The Mixing Mechanism during Lithiation of Si Negative Electrode in Li-Ion Batteries: An Ab Initio Molecular Dynamics Study. *Nano Lett.* **2011**, *11*, 5494−5500.
(218) Jung, S. C.; Han, Y.-K. Ab initio molecular dynamics simulation of lithiation-induced phase-transition of crystalline silicon. *Electrochim. Acta* **2012**, *62*, 73−76.
(219) Key, B.; Bhattacharyya, R.; Morcrette, M.; Seznéc, V.; Tarascon, J.-M.; Grey, C. P. Real-Time NMR Investigations of Structural Changes in Silicon Electrodes for Lithium-Ion Batteries. *J. Am. Chem. Soc.* **2009**, *131*, 9239−9249.
(220) Artrith, N.; Urban, A.; Ceder, G. Constructing first-principles phase diagrams of amorphous Li_x Si using machine-learning-assisted sampling with an evolutionary algorithm. *J. Chem. Phys.* **2018**, *148*, 241711.
(221) Stallworth, P.; Fontanella, J.; Wintersgill, M.; Scheidler, C. D.; Immel, J. J.; Greenbaum, S.; Gozdz, A. NMR, DSC and high pressure electrical conductivity studies of liquid and hybrid electrolytes. *J. Power Sources* **1999**, *81*−*82*, 739−747.
(222) Kraytsberg, A.; Ein-Eli, Y. Higher, Stronger, Better··· A Review of 5 V Cathode Materials for Advanced Lithium-Ion Batteries. *Adv. Energy Mater.* **2012**, *2*, 922−939.
(223) Besenhard, J. O. *Handbook of Battery Materials*; John Wiley & Sons, 2008.
(224) Li, Z.; Huang, J.; Yann Liaw, B.; Metzler, V.; Zhang, J. A review of lithium deposition in lithium-ion and lithium metal secondary batteries. *J. Power Sources* **2014**, *254*, 168−182.
(225) Winter, M. The Solid Electrolyte − Interphase The Most Important and the Least Understood Solid Electrolyte in Rechargeable Li Batteries. *Z. Phys. Chem.* **2009**, *223*, 1395−1406.
(226) Aurbach, D.; Markovsky, B.; Weissman, I.; Levi, E.; Ein-Eli, Y. On the correlation between surface chemistry and performance of graphite negative electrodes for Li ion batteries. *Electrochim. Acta* **1999**, *45*, 67−86.
(227) Wang, G.; Shen, X.; Yao, J.; Park, J. Graphene nanosheets for enhanced lithium storage in lithium ion batteries. *Carbon* **2009**, *47*, 2049−2053.
(228) Arreaga-Salas, D. E.; Sra, A. K.; Roodenko, K.; Chabal, Y. J.; Hinkle, C. L. Progression of Solid Electrolyte Interphase Formation on Hydrogenated Amorphous Silicon Anodes for Lithium-Ion Batteries. *J. Phys. Chem. C* **2012**, *116*, 9072−9077.
(229) Seino, Y.; Ota, T.; Takada, K.; Hayashi, A.; Tatsumisago, M. A sulphide lithium super ion conductor is superior to liquid ion conductors for use in rechargeable batteries. *Energy Environ. Sci.* **2014**, *7*, 627−631.
(230) Murugan, R.; Thangadurai, V.; Weppner, W. Fast Lithium Ion Conduction in Garnet-Type $Li_7La_3Zr_2O_{12}$. *Angew. Chem., Int. Ed.* **2007**, *46*, 7778−7781.
(231) Thangadurai, V.; Narayanan, S.; Pinzaru, D. Garnet-type solid-state fast Li ion conductors for Li batteries: critical review. *Chem. Soc. Rev.* **2014**, *43*, 4714.
(232) Heine, J.; Hilbig, P.; Qi, X.; Niehoff, P.; Winter, M.; Bieker, P. Fluoroethylene Carbonate as Electrolyte Additive in Tetraethylene Glycol Dimethyl Ether Based Electrolytes for Application in Lithium Ion and Lithium Metal Batteries. *J. Electrochem. Soc.* **2015**, *162*, A1094−A1101.
(233) Østergaard, T. M.; Giordano, L.; Castelli, I. E.; Maglia, F.; Antonopoulos, B. K.; Shao-Horn, Y.; Rossmeisl, J. Oxidation of Ethylene Carbonate on Li Metal Oxide Surfaces. *J. Phys. Chem. C* **2018**, *122*, 10442−10449.
(234) Goodenough, J. B.; Kim, Y. Challenges for Rechargeable Li Batteries†. *Chem. Mater.* **2010**, *22*, 587−603.
(235) Tasaki, K. Solvent Decompositions and Physical Properties of Decomposition Compounds in Li-Ion Battery Electrolytes Studied by DFT Calculations and Molecular Dynamics Simulations. *J. Phys. Chem. B* **2005**, *109*, 2920−2933.
(236) Borodin, O.; Smith, G. D. Quantum Chemistry and Molecular Dynamics Simulation Study of Dimethyl Carbonate: Ethylene Carbonate Electrolytes Doped with $LiPF_6$. *J. Phys. Chem. B* **2009**, *113*, 1763−1776.
(237) Borodin, O. Polarizable Force Field Development and Molecular Dynamics Simulations of Ionic Liquids. *J. Phys. Chem. B* **2009**, *113*, 11463−11478.
(238) Seo, D. M.; Borodin, O.; Han, S.-D.; Boyle, P. D.; Henderson, W. A. Electrolyte Solvation and Ionic Association II. Acetonitrile-Lithium Salt Mixtures: Highly Dissociated Salts. *J. Electrochem. Soc.* **2012**, *159*, A1489−A1500.
(239) Wang, Y.; Nakamura, S.; Ue, M.; Balbuena, P. B. Theoretical Studies To Understand Surface Chemistry on Carbon Anodes for Lithium-Ion Batteries: Reduction Mechanisms of Ethylene Carbonate. *J. Am. Chem. Soc.* **2001**, *123*, 11708−11718.
(240) Yu, J.; Balbuena, P. B.; Budzien, J.; Leung, K. Hybrid DFT Functional-Based Static and Molecular Dynamics Studies of Excess Electron in Liquid Ethylene Carbonate. *J. Electrochem. Soc.* **2011**, *158*, A400−A410.
(241) Xing, L.; Borodin, O. Oxidation induced decomposition of ethylene carbonate from DFT calculations − importance of explicitly treating surrounding solvent. *Phys. Chem. Chem. Phys.* **2012**, *14*, 12838−12843.
(242) Li, Y.; Leung, K.; Qi, Y. Computational Exploration of the Li-Electrode|Electrolyte Interface in the Presence of a Nanometer Thick Solid-Electrolyte Interphase Layer. *Acc. Chem. Res.* **2016**, *49*, 2363−2370.
(243) Shkrob, I. A.; Zhu, Y.; Marin, T. W.; Abraham, D. Reduction of Carbonate Electrolytes and the Formation of Solid-Electrolyte Interface (SEI) in Lithium-Ion Batteries. 1. Spectroscopic Observations of Radical Intermediates Generated in One-Electron Reduction of Carbonates. *J. Phys. Chem. C* **2013**, *117*, 19255−19269.
(244) Leung, K. Two-electron reduction of ethylene carbonate: A quantum chemistry re-examination of mechanisms. *Chem. Phys. Lett.* **2013**, *568*−*569*, 1−8.
(245) Metzger, M.; Marino, C.; Sicklinger, J.; Haering, D.; Gasteiger, H. A. Anodic Oxidation of Conductive Carbon and Ethylene Carbonate in High-Voltage Li-Ion Batteries Quantified by On-Line Electrochemical Mass Spectrometry. *J. Electrochem. Soc.* **2015**, *162*, A1123−A1134.
(246) Imhof, R.; Novák, P. Oxidative Electrolyte Solvent Degradation in Lithium-Ion Batteries: An In Situ Differential Electrochemical Mass Spectrometry Investigation. *J. Electrochem. Soc.* **1999**, *146*, 1702−1706.
(247) Kumar, N.; Leung, K.; Siegel, D. J. Crystal Surface and State of Charge Dependencies of Electrolyte Decomposition on $LiMn_2O_4$ Cathode. *J. Electrochem. Soc.* **2014**, *161*, E3059−E3065.
(248) Xu, S.; Luo, G.; Jacobs, R.; Fang, S.; Mahanthappa, M. K.; Hamers, R. J.; Morgan, D. Ab Initio Modeling of Electrolyte Molecule Ethylene Carbonate Decomposition Reaction on $Li(Ni,Mn,Co)O_2$ Cathode Surface. *ACS Appl. Mater. Interfaces* **2017**, *9*, 20545−20553.
(249) Tebbe, J. L.; Fuerst, T. F.; Musgrave, C. B. Degradation of Ethylene Carbonate Electrolytes of Lithium Ion Batteries via Ring Opening Activated by $LiCoO_2$ Cathode Surfaces and Electrolyte Species. *ACS Appl. Mater. Interfaces* **2016**, *8*, 26664−26674.
(250) Metzger, M.; Strehle, B.; Solchenbach, S.; Gasteiger, H. A. Origin of H2 Evolution in LIBs: H2O Reduction vs. Electrolyte Oxidation. *J. Electrochem. Soc.* **2016**, *163*, A798−A809.
(251) Aykol, M.; Kirklin, S.; Wolverton, C. Thermodynamic Aspects of Cathode Coatings for Lithium-Ion Batteries. *Adv. Energy Mater.* **2014**, *4*, 1400690.
(252) Aykol, M.; Kim, S.; Hegde, V. I.; Snydacker, D.; Lu, Z.; Hao, S.; Kirklin, S.; Morgan, D.; Wolverton, C. High-throughput computational design of cathode coatings for Li-ion batteries. *Nat. Commun.* **2016**, *7*, 13779.
(253) Ramos-Sanchez, G.; Soto, F. A.; Martinez de la Hoz, J. M.; Liu, Z.; Mukherjee, P. P.; El-Mellouhi, F.; Seminario, J. M.; Balbuena, P. B. Computational Studies of Interfacial Reactions at Anode Materials: Initial Stages of the Solid-Electrolyte-Interphase Layer Formation. *J. Electrochem. En. Conv. Stor.* **2016**, *13*, No. 031002.
(254) Methekar, R. N.; Northrop, P. W. C.; Chen, K.; Braatz, R. D.; Subramanian, V. R. Kinetic Monte Carlo Simulation of Surface Heterogeneity in Graphite Anodes for Lithium-Ion Batteries: Passive Layer Formation. *J. Electrochem. Soc.* **2011**, *158*, A363.

https://dx.doi.org/10.1021/acs.chemrev.9b00601
Chem. Rev. 2020, 120, 6977−7019

(255) Suo, L.; Borodin, O.; Gao, T.; Olguin, M.; Ho, J.; Fan, X.; Luo, C.; Wang, C.; Xu, K. Water-in-salt" electrolyte enables high-voltage aqueous lithium-ion chemistries. *Science* **2015**, *350*, 938−943.
(256) Suo, L.; Borodin, O.; Sun, W.; Fan, X.; Yang, C.; Wang, F.; Gao, T.; Ma, Z.; Schroeder, M.; vonCresce, A.; Russell, S. M.; Armand, M.; Angell, A.; Xu, K.; Wang, C. Advanced High-Voltage Aqueous Lithium-Ion Battery Enabled by "Water-in-Bisalt" Electrolyte. *Angew. Chem., Int. Ed.* **2016**, *55*, 7136−7141.
(257) Okoshi, M.; Chou, C.-P.; Nakai, H. Theoretical Analysis of Carrier Ion Diffusion in Superconcentrated Electrolyte Solutions for Sodium-Ion Batteries. *J. Phys. Chem. B* **2018**, *122*, 2600−2609.
(258) Elstner, M.; Porezag, D.; Jungnickel, G.; Elsner, J.; Haugk, M.; Frauenheim, T.; Suhai, S.; Seifert, G. Self-consistent-charge density-functional tight-binding method for simulations of complex materials properties. *Phys. Rev. B: Condens. Matter Mater. Phys.* **1998**, *58*, 7260−7268.
(259) Frauenheim, T.; Seifert, G.; Elstner, M.; Niehaus, T.; Köhler, C.; Amkreutz, M.; Sternberg, M.; Hajnal, Z.; Carlo, A. D.; Suhai, S. Atomistic simulations of complex materials: ground-state and excited-state properties. *J. Phys.: Condens. Matter* **2002**, *14*, 3015−3047.
(260) Huddleston, J. G.; Willauer, H. D.; Swatloski, R. P.; Visser, A. E.; Rogers, R. D. Room temperature ionic liquids as novel media for 'clean' liquid−liquid extraction. *Chem. Commun.* **1998**, 1765−1766.
(261) Chou, S.-L.; Wang, J.-Z.; Sun, J.-Z.; Wexler, D.; Forsyth, M.; Liu, H.-K.; MacFarlane, D. R.; Dou, S.-X. High Capacity, Safety, and Enhanced Cyclability of Lithium Metal Battery Using a V_2 O_5 Nanomaterial Cathode and Room Temperature Ionic Liquid Electrolyte. *Chem. Mater.* **2008**, *20*, 7044−7051.
(262) Kim, G.-T.; Jeong, S.; Xue, M.-Z.; Balducci, A.; Winter, M.; Passerini, S.; Alessandrini, F.; Appetecchi, G. Development of ionic liquid-based lithium battery prototypes. *J. Power Sources* **2012**, *199*, 239−246.
(263) Galinski, M.; Lewandowski, A.; Stepniak, I. Ionic liquids as electrolytes. *Electrochim. Acta* **2006**, *51*, 5567−5580.
(264) Ong, S. P.; Andreussi, O.; Wu, Y.; Marzari, N.; Ceder, G. Electrochemical Windows of Room-Temperature Ionic Liquids from Molecular Dynamics and Density Functional Theory Calculations. *Chem. Mater.* **2011**, *23*, 2979−2986.
(265) Howlett, P. C.; Izgorodina, E. I.; Forsyth, M.; MacFarlane, D. R. Electrochemistry at Negative Potentials in Bis-(trifluoromethanesulfonyl)amide Ionic Liquids. *Z. Phys. Chem.* **2006**, *220*, 1483−1498.
(266) Gizbar, H.; Vestfrid, Y.; Chusid, O.; Gofer, Y.; Gottlieb, H. E.; Marks, V.; Aurbach, D. Alkyl Group Transmetalation Reactions in Electrolytic Solutions Studied by Multinuclear NMR. *Organometallics* **2004**, *23*, 3826−3831.
(267) Mizrahi, O.; Amir, N.; Pollak, E.; Chusid, O.; Marks, V.; Gottlieb, H.; Larush, L.; Zinigrad, E.; Aurbach, D. Electrolyte Solutions with a Wide Electrochemical Window for Rechargeable Magnesium Batteries. *J. Electrochem. Soc.* **2008**, *155*, A103.
(268) Pour, N.; Gofer, Y.; Major, D. T.; Aurbach, D. Structural Analysis of Electrolyte Solutions for Rechargeable Mg Batteries by Stereoscopic Means and DFT Calculations. *J. Am. Chem. Soc.* **2011**, *133*, 6270−6278.
(269) Wan, L. F.; Prendergast, D. The Solvation Structure of Mg Ions in Dichloro Complex Solutions from First-Principles Molecular Dynamics and Simulated X-ray Absorption Spectra. *J. Am. Chem. Soc.* **2014**, *136*, 14456−14464.
(270) Nakayama, Y.; Kudo, Y.; Oki, H.; Yamamoto, K.; Kitajima, Y.; Noda, K. Complex Structures and Electrochemical Properties of Magnesium Electrolytes. *J. Electrochem. Soc.* **2008**, *155*, A754−A759.
(271) Canepa, P.; Jayaraman, S.; Cheng, L.; Rajput, N. N.; Richards, W. D.; Gautam, G. S.; Curtiss, L. A.; Persson, K. A.; Ceder, G. Elucidating the structure of the magnesium aluminum chloride complex electrolyte for magnesium-ion batteries. *Energy Environ. Sci.* **2015**, *8*, 3718−3730.
(272) Abraham, K. M.; Jiang, Z. A Polymer Electrolyte-Based Rechargeable Lithium/Oxygen Battery. *J. Electrochem. Soc.* **1996**, *143*, 1−5.
(273) Borodin, O.; Smith, G. D. Mechanism of Ion Transport in Amorphous Poly(ethylene oxide)/LiTFSI from Molecular Dynamics Simulations. *Macromolecules* **2006**, *39*, 1620−1629.
(274) Johansson, P.; Tegenfeldt, J.; Lindgren, J. Modelling amorphous lithium salt−PEO polymer electrolytes: ab initio calculations of lithium ion−tetra-, penta- and hexaglyme complexes. *Polymer* **1999**, *40*, 4399−4406.
(275) Balbuena, P. B.; Lamas, E. J.; Wang, Y. Molecular modeling studies of polymer electrolytes for power sources. *Electrochim. Acta* **2005**, *50*, 3788−3795.
(276) Maitra, A.; Heuer, A. Cation Transport in Polymer Electrolytes: A Microscopic Approach. *Phys. Rev. Lett.* **2007**, *98*, 227802.
(277) Seo, Y.; Brown, J. R.; Hall, L. M. Diffusion of Selective Penetrants in Interfacially Modified Block Copolymers from Molecular Dynamics Simulations. *ACS Macro Lett.* **2017**, *6*, 375−380.
(278) Timachova, K.; Villaluenga, I.; Cirrincione, L.; Gobet, M.; Bhattacharya, R.; Jiang, X.; Newman, J.; Madsen, L. A.; Greenbaum, S. G.; Balsara, N. P. Anisotropic Ion Diffusion and Electrochemically Driven Transport in Nanostructured Block Copolymer Electrolytes. *J. Phys. Chem. B* **2018**, *122*, 1537−1544.
(279) Bhatt, M. D.; O'Dwyer, C. Recent progress in theoretical and computational investigations of Li-ion battery materials and electrolytes. *Phys. Chem. Chem. Phys.* **2015**, *17*, 4799−4844.
(280) Mogurampelly, S.; Borodin, O.; Ganesan, V. Computer Simulations of Ion Transport in Polymer Electrolyte Membranes. *Annu. Rev. Chem. Biomol. Eng.* **2016**, *7*, 349−371.
(281) Graf, P.; Nitzan, A.; Kurnikova, M. G.; Coalson, R. D. A Dynamic Lattice Monte Carlo Model of Ion Transport in Inhomogeneous Dielectric Environments: Method and Implementation. *J. Phys. Chem. B* **2000**, *104*, 12324−12338.
(282) Marchi, M.; Borgis, D.; Levy, N.; Ballone, P. A dielectric continuum molecular dynamics method. *J. Chem. Phys.* **2001**, *114*, 4377.
(283) Maggs, A. C.; Rossetto, V. Local Simulation Algorithms for Coulomb Interactions. *Phys. Rev. Lett.* **2002**, *88*, 196402.
(284) Jadhao, V.; Solis, F. J.; Olvera de la Cruz, M. A variational formulation of electrostatics in a medium with spatially varying dielectric permittivity. *J. Chem. Phys.* **2013**, *138*, No. 054119.
(285) Hong, H. Y.-P. Crystal structures and crystal chemistry in the system $Na_{1+x}Zr_2Si_xP_{3-x}O_{12}$. *Mater. Res. Bull.* **1976**, *11*, 173−182.
(286) Goodenough, J. B.; Hong, H. Y.-p.; Kafalas, J. A. Fast Na+-ion Transport in Skeleton Structures. *Mater. Res. Bull.* **1976**, *11*, 203−220.
(287) Hong, H. Y.-P. Crystal Structure and Ionic Conductivity of $Li_{14}Zn(GeO_4)_4$ and Other New Li^+ Superionic Conductors. *Mater. Res. Bull.* **1978**, *13* (2), 117−124.
(288) Inaguma, Y.; Liquan, C.; Itoh, M.; Nakamura, T.; Uchida, T.; Ikuta, H.; Wakihara, M. High ionic conductivity in lithium lanthanum titanate. *Solid State Commun.* **1993**, *86*, 689−693.
(289) Thangadurai, V.; Kaack, H.; Weppner, W. J. F. Novel Fast Lithium Ion Conduction in Garnet-Type $Li_5La_3M_2O_{12}$ (M: Nb, Ta). *J. Am. Ceram. Soc.* **2003**, *86*, 437−440.
(290) Kanno, R.; Murayama, M. Lithium Ionic Conductor Thio-LISICON: The Li_2 S GeS_2 P_2 S_5 System. *J. Electrochem. Soc.* **2001**, *148*, A742−A746.
(291) Tatsumisago, M.; Hayashi, A. Sulfide Glass-Ceramic Electrolytes for All-Solid-State Lithium and Sodium Batteries. *Int. J. Appl. Glass Sci.* **2014**, *5*, 226−235.
(292) Deiseroth, H.-J.; Kong, S.-T.; Eckert, H.; Vannahme, J.; Reiner, C.; Zaiß, T.; Schlosser, M. Li_6PS_5X: A Class of Crystalline Li-Rich Solids With an Unusually High Li^+ Mobility. *Angew. Chem., Int. Ed.* **2008**, *47*, 755−758.
(293) Boukamp, B. A.; Huggins, R. A. Lithium ion conductivity in lithium nitride. *Phys. Lett. A* **1976**, *58*, 231−233.
(294) Weppner, W.; Hartwig, P.; Rabenau, A. Consideration of lithium nitride halides as solid electrolytes in practical galvanic cell applications. *J. Power Sources* **1981**, *6*, 251−259.
(295) Kitahama, K.; Furukawa, Y.; Kawai, S.; Nakamura, O. SYNTHESIS AND NMR STUDY OF SOLID ELECTROLYTES IN THE SYSTEM Li:˜I-LiCI. *Solid State Ionics* **1981**, *3-4*, 335−339.

https://dx.doi.org/10.1021/acs.chemrev.9b00601
Chem. Rev. 2020, 120, 6977−7019

(296) Bates, J.; Dudney, N.; Gruzalski, G.; Zuhr, R.; Choudhury, A.; Luck, C.; Robertson, J. Fabrication and characterization of amorphous lithium electrolyte thin films and rechargeable thin-film batteries. *J. Power Sources* **1993**, *43*, 103−110.
(297) Suzuki, N.; Inaba, T.; Shiga, T. Electrochemical properties of LiPON films made from a mixed powder target of Li_3PO_4 and Li_2O. *Thin Solid Films* **2012**, *520*, 1821−1825.
(298) Zhao, Y.; Daemen, L. L. Superionic Conductivity in Lithium-Rich Anti-Perovskites. *J. Am. Chem. Soc.* **2012**, *134*, 15042−15047.
(299) Geiger, C. A.; Alekseev, E.; Lazic, B.; Fisch, M.; Armbruster, T.; Langner, R.; Fechtelkord, M.; Kim, N.; Pettke, T.; Weppner, W. Crystal Chemistry and Stability of "Li_7 La_3 Zr_2 O_{12}" Garnet: A Fast Lithium-Ion Conductor. *Inorg. Chem.* **2011**, *50*, 1089−1097.
(300) Awaka, J.; Kijima, N.; Hayakawa, H.; Akimoto, J. Synthesis and structure analysis of tetragonal $Li_7La_3Zr_2O_{12}$ with the garnet-related type structure. *J. Solid State Chem.* **2009**, *182*, 2046−2052.
(301) Awaka, J.; Takashima, A.; Kataoka, K.; Kijima, N.; Idemoto, Y.; Akimoto, J. Crystal Structure of Fast Lithium-ion-conducting Cubic $Li_7La_3Zr_2O_{12}$. *Chem. Lett.* **2011**, *40*, 60−62.
(302) Jalem, R.; Yamamoto, Y.; Shiiba, H.; Nakayama, M.; Munakata, H.; Kasuga, T.; Kanamura, K. Concerted Migration Mechanism in the Li Ion Dynamics of Garnet-Type Li_7 La_3 Zr_2 O_{12}. *Chem. Mater.* **2013**, *25*, 425−430.
(303) He, X.; Zhu, Y.; Mo, Y. Origin of fast ion diffusion in super-ionic conductors. *Nat. Commun.* **2017**, *8*, 15893.
(304) Xie, H.; Alonso, J. A.; Li, Y.; Fernández-Díaz, M. T.; Goodenough, J. B. Lithium Distribution in Aluminum-Free Cubic Li_7 La_3 Zr_2 O_{12}. *Chem. Mater.* **2011**, *23*, 3587−3589.
(305) Xu, M.; Park, M. S.; Lee, J. M.; Kim, T. Y.; Park, Y. S.; Ma, E. Mechanisms of Li^+ transport in garnet-type cubic Li_{3+x} La_3 M_2 O_{12} (M = Te, Nb, Zr). *Phys. Rev. B: Condens. Matter Mater. Phys.* **2012**, *85*, No. 052301.
(306) Miara, L. J.; Ong, S. P.; Mo, Y.; Richards, W. D.; Park, Y.; Lee, J.-M.; Lee, H. S.; Ceder, G. Effect of Rb and Ta Doping on the Ionic Conductivity and Stability of the Garnet Li_{7+2x-y} $(La_{3-x}$ $Rb_x)(Zr_{2-y}$ $Ta_y)O_{12}$ $(0 \le x \le 0.375, 0 \le y \le 1)$ Superionic Conductor: A First Principles Investigation. *Chem. Mater.* **2013**, *25*, 3048−3055.
(307) Jolley, A. G.; Cohn, G.; Hitz, G. T.; Wachsman, E. D. Improving the ionic conductivity of NASICON through aliovalent cation substitution of Na3Zr2Si2PO12. *Ionics* **2015**, *21*, 3031−3038.
(308) Mottet, M.; Marcolongo, A.; Laino, T.; Tavernelli, I. Doping in garnet-type electrolytes: Kinetic and thermodynamic effects from molecular dynamics simulations. *Phys. Rev. Materials* **2019**, *3*, No. 035403.
(309) Bernstein, N.; Johannes, M. D.; Hoang, K. Origin of the Structural Phase Transition in $Li_7La_3Zr_2O_{12}$. *Phys. Rev. Lett.* **2012**, *109*, 205702.
(310) Squires, A. G.; Scanlon, D. O.; Morgan, B. J. Native Defects and their Doping Response in the Lithium Solid Electrolyte Li7La3Zr2O12. *Chem. Mater.* **2019**.
(311) Bohnke, O. Conductivity measurements on nasicon and nasicon-modified materials. *Solid State Ionics* **1999**, *122*, 127−136.
(312) Fuentes, R. O.; Figueiredo, F. M.; Marques, F. M. B.; Franco, J. I. Influence of microstructure on the electrical properties of NASICON materials. *Solid State Ionics* **2001**, *140*, 173−179.
(313) Moriwake, H.; Gao, X.; Kuwabara, A.; Fisher, C. A.J.; Kimura, T.; Ikuhara, Y. H.; Kohama, K.; Tojigamori, T.; Ikuhara, Y. Domain boundaries and their influence on Li migration in solid-state electrolyte (La,Li)TiO3. *J. Power Sources* **2015**, *276*, 203−207.
(314) Samiee, M.; Radhakrishnan, B.; Rice, Z.; Deng, Z.; Meng, Y. S.; Ong, S. P.; Luo, J. Divalent-doped Na3Zr2Si2PO12 natrium superionic conductor: Improving the ionic conductivity via simultaneously optimizing the phase and chemistry of the primary and secondary phases. *J. Power Sources* **2017**, *347*, 229−237.
(315) Deng, Z.; Mo, Y.; Ong, S. P. Computational studies of solid-state alkali conduction in rechargeable alkali-ion batteries. *NPG Asia Mater.* **2016**, *8*, e254−e254.
(316) Deng, Z.; Zhu, Z.; Chu, I.-H.; Ong, S. P. Data-Driven First-Principles Methods for the Study and Design of Alkali Superionic Conductors. *Chem. Mater.* **2017**, *29*, 281−288.
(317) He, X.; Zhu, Y.; Epstein, A.; Mo, Y. Statistical variances of diffusional properties from ab initio molecular dynamics simulations. *npj Comput. Mater.* **2018**, *4*, 18.
(318) Mo, Y.; Ong, S. P.; Ceder, G. First Principles Study of the Li10GeP2S12 Lithium Super Ionic Conductor Material. *Chem. Mater.* **2012**, *24*, 15−17.
(319) Ong, S. P.; Mo, Y.; Richards, W. D.; Miara, L.; Lee, H. S.; Ceder, G. Phase stability, electrochemical stability and ionic conductivity of the Li101MP2 × 12 (M = Ge, Si, Sn, Al or P, and X = O, S or Se) family of superionic conductors. *Energy Environ. Sci.* **2013**, *6*, 148.
(320) Wang, Y.; Richards, W. D.; Ong, S. P.; Miara, L. J.; Kim, J. C.; Mo, Y.; Ceder, G. Design principles for solid-state lithium superionic conductors. *Nat. Mater.* **2015**, *14*, 1026−1031.
(321) Bron, P.; Johansson, S.; Zick, K.; Schmedt auf der Günne, J.; Dehnen, S.; Roling, B. Li_{10} SnP_2 S_{12}: An Affordable Lithium Superionic Conductor. *J. Am. Chem. Soc.* **2013**, *135*, 15694−15697.
(322) Kuhn, A.; Gerbig, O.; Zhu, C.; Falkenberg, F.; Maier, J.; Lotsch, B. V. A new ultrafast superionic Li-conductor: ion dynamics in Li_{11} Si_2 PS_{12} and comparison with other tetragonal LGPS-type electrolytes. *Phys. Chem. Chem. Phys.* **2014**, *16*, 14669−14674.
(323) Zhou, P.; Wang, J.; Cheng, F.; Li, F.; Chen, J. A solid lithium superionic conductor Li11AlP2S12 with a thio-LISICON analogous structure. *Chem. Commun.* **2016**, *52*, 6091−6094.
(324) Weber, D. A.; Senyshyn, A.; Weldert, K. S.; Wenzel, S.; Zhang, W.; Kaiser, R.; Berendts, S.; Janek, J.; Zeier, W. G. Structural Insights and 3D Diffusion Pathways within the Lithium Superionic Conductor Li_{10} GeP_2 S_{12}. *Chem. Mater.* **2016**, *28*, 5905−5915.
(325) Richards, W. D.; Tsujimura, T.; Miara, L. J.; Wang, Y.; Kim, J. C.; Ong, S. P.; Uechi, I.; Suzuki, N.; Ceder, G. Design and synthesis of the superionic conductor Na10SnP2S12. *Nat. Commun.* **2016**, *7*, 11009.
(326) Chu, I.-H.; Nguyen, H.; Hy, S.; Lin, Y.-C.; Wang, Z.; Xu, Z.; Deng, Z.; Meng, Y. S.; Ong, S. P. Insights into the Performance Limits of the Li7P3S11 Superionic Conductor: A Combined First-Principles and Experimental Study. *ACS Appl. Mater. Interfaces* **2016**, *8*, 7843−7853.
(327) Richards, W. D.; Wang, Y.; Miara, L. J.; Kim, J. C.; Ceder, G. Design of Li_{1+2x} Zn_{1-x} PS_4, a new lithium ion conductor. *Energy Environ. Sci.* **2016**, *9*, 3272−3278.
(328) Kaup, K.; Lalère, F.; Huq, A.; Shyamsunder, A.; Adermann, T.; Hartmann, P.; Nazar, L. F. Correlation of Structure and Fast Ion Conductivity in the Solid Solution Series Li_{1+2x} Zn_{1-x} PS_4. *Chem. Mater.* **2018**, *30*, 592−596.
(329) Zhang, L.; Yang, K.; Mi, J.; Lu, L.; Zhao, L.; Wang, L.; Li, Y.; Zeng, H. Na_3 PSe_4: A Novel Chalcogenide Solid Electrolyte with High Ionic Conductivity. *Adv. Energy Mater.* **2015**, *5*, 1501294.
(330) Chu, I.-H.; Kompella, C. S.; Nguyen, H.; Zhu, Z.; Hy, S.; Deng, Z.; Meng, Y. S.; Ong, S. P. Room-Temperature All-solid-state Rechargeable Sodium-ion Batteries with a Cl-doped Na3PS4 Superionic Conductor. *Sci. Rep.* **2016**, *6*, 33733.
(331) de Klerk, N. J. J.; Wagemaker, M. Diffusion Mechanism of the Sodium-Ion Solid Electrolyte Na_3 PS_4 and Potential Improvements of Halogen Doping. *Chem. Mater.* **2016**, *28*, 3122−3130.
(332) Banerjee, A.; Park, K. H.; Heo, J. W.; Nam, Y. J.; Moon, C. K.; Oh, S. M.; Hong, S.-T.; Jung, Y. S. Na3SbS4: A Solution Processable Sodium Superionic Conductor for All-Solid-State Sodium-Ion Batteries. *Angew. Chem.* **2016**, *128*, 9786−9790.
(333) Krauskopf, T.; Muy, S.; Culver, S. P.; Ohno, S.; Delaire, O.; Shao-Horn, Y.; Zeier, W. G. Comparing the Descriptors for Investigating the Influence of Lattice Dynamics on Ionic Transport Using the Superionic Conductor Na3PS4−xSex. *J. Am. Chem. Soc.* **2018**, *140*, 14464−14473.
(334) Kandagal, V. S.; Bharadwaj, M. D.; Waghmare, U. V. Theoretical prediction of a highly conducting solid electrolyte for sodium batteries: Na_{10} GeP_2 S_{12}. *J. Mater. Chem. A* **2015**, *3*, 12992−12999.

https://dx.doi.org/10.1021/acs.chemrev.9b00601
Chem. Rev. 2020, 120, 6977−7019

(335) Zhu, Z.; Chu, I.-H.; Deng, Z.; Ong, S. P. Role of Na+ Interstitials and Dopants in Enhancing the Na+ Conductivity of the Cubic Na3PS4 Superionic Conductor. *Chem. Mater.* **2015**, *27*, 8318−8325.
(336) Feng, X.; Chien, P.-H.; Zhu, Z.; Chu, I.-H.; Wang, P.; Immediato-Scuotto, M.; Arabzadeh, H.; Ong, S. P.; Hu, Y.-Y. Studies of Functional Defects for Fast Na-Ion Conduction in Na3yPS4xClx with a Combined Experimental and Computational Approach. *Adv. Funct. Mater.* **2019**, *29*, 1807951.
(337) Rao, R. P.; Chen, H.; Wong, L. L.; Adams, S. Na_{3+x} M_x P_{1-x} S_4 (M = Ge^{4+}, Ti^{4+}, Sn^{4+}) enables high rate all-solid-state Na-ion batteries $Na_{2+2\delta}$ $Fe_{2-\delta}$ $(SO_4)_3$|Na_{3+x} M_x P_{1-x} S_4|Na_2 Ti_3 O_7. *J. Mater. Chem. A* **2017**, *5*, 3377−3388.
(338) Yu, Z.; Shang, S.-L.; Seo, J.-H.; Wang, D.; Luo, X.; Huang, Q.; Chen, S.; Lu, J.; Li, X.; Liu, Z.-K.; Wang, D. Exceptionally High Ionic Conductivity in Na3P0.62As0.38S4 with Improved Moisture Stability for Solid-State Sodium-Ion Batteries. *Adv. Mater.* **2017**, *29*, 1605561.
(339) Wang, H.; Chen, Y.; Hood, Z. D.; Sahu, G.; Pandian, A. S.; Keum, J. K.; An, K.; Liang, C. An Air-Stable Na3SbS4 Superionic Conductor Prepared by a Rapid and Economic Synthetic Procedure. *Angew. Chem., Int. Ed.* **2016**, *55*, 8551−8555.
(340) Rush, L. E.; Hood, Z. D.; Holzwarth, N. A. W. Unraveling the electrolyte properties of Na_3SbS_4 through computation and experiment. *Phys. Rev. Materials* **2017**, *1*, No. 075405.
(341) Bo, S.-H.; Wang, Y.; Kim, J. C.; Richards, W. D.; Ceder, G. Computational and Experimental Investigations of Na-Ion Conduction in Cubic Na_3 PSe_4. *Chem. Mater.* **2016**, *28*, 252−258.
(342) Wang, N.; Yang, K.; Zhang, L.; Yan, X.; Wang, L.; Xu, B. Improvement in ion transport in Na3PSe4−Na3SbSe4 by Sb substitution. *J. Mater. Sci.* **2018**, *53*, 1987−1994.
(343) Zhang, Z.; Ramos, E.; Lalère, F.; Assoud, A.; Kaup, K.; Hartman, P.; Nazar, L. F. Na11Sn2PS12: a new solid state sodium superionic conductor. *Energy Environ. Sci.* **2018**, *11*, 87−93.
(344) Duchardt, M.; Ruschewitz, U.; Adams, S.; Dehnen, S.; Roling, B. Vacancy-Controlled Na+ Superion Conduction in Na11Sn2PS12. *Angew. Chem., Int. Ed.* **2018**, *57*, 1351−1355.
(345) Heo, J. W.; Banerjee, A.; Park, K. H.; Jung, Y. S.; Hong, S.-T. New Na-Ion Solid Electrolytes Na_{4-x} Sn_{1-x} Sb_x S_4 ($0.02 \leq x \leq 0.33$) for All-Solid-State Na-Ion Batteries. *Adv. Energy Mater.* **2018**, *8*, 1702716.
(346) Duchardt, M.; Neuberger, S.; Ruschewitz, U.; Krauskopf, T.; Zeier, W. G.; Schmedt auf der Günne, J.; Adams, S.; Roling, B.; Dehnen, S. Superion Conductor Na11.1Sn2.1P0.9Se12: Lowering the Activation Barrier of Na+ Conduction in Quaternary 1−4−5−6 Electrolytes. *Chem. Mater.* **2018**, *30*, 4134−4139.
(347) Oh, K.; Chang, D.; Park, I.; Yoon, K.; Kang, K. First-Principles Investigations on Sodium Superionic Conductor Na_{11} Sn_2 PS_{12}. *Chem. Mater.* **2019**, *31*, 6066−6075.
(348) Canepa, P.; Sai Gautam, G.; Broberg, D.; Bo, S.-H.; Ceder, G. Role of Point Defects in Spinel Mg Chalcogenide Conductors. *Chem. Mater.* **2017**, *29*, 9657−9667.
(349) Miara, L. J.; Richards, W. D.; Wang, Y. E.; Ceder, G. First-Principles Studies on Cation Dopants and Electrolyte|Cathode Interphases for Lithium Garnets. *Chem. Mater.* **2015**, *27*, 4040−4047.
(350) Zhu, Y.; He, X.; Mo, Y. Origin of Outstanding Stability in the Lithium Solid Electrolyte Materials: Insights from Thermodynamic Analyses Based on First-Principles Calculations. *ACS Appl. Mater. Interfaces* **2015**, *7*, 23685−23693.
(351) Richards, W. D.; Miara, L. J.; Wang, Y.; Kim, J. C.; Ceder, G. Interface Stability in Solid-State Batteries. *Chem. Mater.* **2016**, *28*, 266−273.
(352) Zhu, Y.; He, X.; Mo, Y. First principles study on electrochemical and chemical stability of solid electrolyte−electrode interfaces in all-solid-state Li-ion batteries. *J. Mater. Chem. A* **2016**, *4*, 3253−3266.
(353) Tian, Y.; Shi, T.; Richards, W. D.; Li, J.; Kim, J. C.; Bo, S.-H.; Ceder, G. Compatibility issues between electrodes and electrolytes in solid-state batteries. *Energy Environ. Sci.* **2017**, *10*, 1150−1166.
(354) Xiao, Y.; Miara, L. J.; Wang, Y.; Ceder, G. Computational Screening of Cathode Coatings for Solid-State Batteries. *Joule* **2019**, *3*, 1252−1275.
(355) Han, F.; Gao, T.; Zhu, Y.; Gaskell, K. J.; Wang, C. A Battery Made from a Single Material. *Adv. Mater.* **2015**, *27*, 3473−3483.
(356) Han, F.; Zhu, Y.; He, X.; Mo, Y.; Wang, C. Electrochemical Stability of Li_{10} GeP_2 S_{12} and Li_7 La_3 Zr_2 O_{12} Solid Electrolytes. *Adv. Energy Mater.* **2016**, *6*, 1501590.
(357) Wenzel, S.; Randau, S.; Leichtweiß, T.; Weber, D. A.; Sann, J.; Zeier, W. G.; Janek, J. Direct Observation of the Interfacial Instability of the Fast Ionic Conductor Li_{10} GeP_2 S_{12} at the Lithium Metal Anode. *Chem. Mater.* **2016**, *28*, 2400−2407.
(358) Haruyama, J.; Sodeyama, K.; Han, L.; Takada, K.; Tateyama, Y. SpaceCharge Layer Effect at Interface between Oxide Cathode and Sulfide Electrolyte in All-Solid-State Lithium-Ion Battery. *Chem. Mater.* **2014**, *26*, 4248−4255.
(359) Stegmaier, S.; Voss, J.; Reuter, K.; Luntz, A. C. Li^+ Defects in a Solid-State Li Ion Battery: Theoretical Insights with a Li_3 OCl Electrolyte. *Chem. Mater.* **2017**, *29*, 4330−4340.
(360) Nolan, A. M.; Zhu, Y.; He, X.; Bai, Q.; Mo, Y. Computation-Accelerated Design of Materials and Interfaces for All-Solid-State Lithium-Ion Batteries. *Joule* **2018**, *2*, 2016−2046.
(361) Al-Qawasmeh, A.; Holzwarth, N. A. W. Li14P2O3N6 and Li7PN4: Computational study of two nitrogen rich crystalline LiPON electrolyte materials. *J. Power Sources* **2017**, *364*, 410−419.
(362) Lepley, N. D.; Holzwarth, N. A. W. Modeling interfaces between solids: Application to Li battery materials. *Phys. Rev. B: Condens. Matter Mater. Phys.* **2015**, *92*, 214201.
(363) Li, J.; Ma, C.; Chi, M.; Liang, C.; Dudney, N. J. Lithium-Ion Batteries: Solid Electrolyte: the Key for High-Voltage Lithium Batteries (Adv. Energy Mater. 4/2015). *Adv. Energy Mater.* **2015**, *5*, 18.
(364) Deng, Z.; Radhakrishnan, B.; Ong, S. P. Rational Composition Optimization of the Lithium-Rich Li_3 OCl_{1-x} Br_x Anti-Perovskite Superionic Conductors. *Chem. Mater.* **2015**, *27*, 3749−3755.
(365) Emly, A.; Kioupakis, E.; Van der Ven, A. Phase Stability and Transport Mechanisms in Antiperovskite Li_3 OCl and Li_3 OBr Superionic Conductors. *Chem. Mater.* **2013**, *25*, 4663−4670.
(366) Chen, M.-H.; Emly, A.; Van der Ven, A. Anharmonicity and phase stability of antiperovskite Li 3 OCl. *Phys. Rev. B: Condens. Matter Mater. Phys.* **2015**, *91*, 214306.
(367) Song, A.-Y.; Xiao, Y.; Turcheniuk, K.; Upadhya, P.; Ramanujapuram, A.; Benson, J.; Magasinski, A.; Olguin, M.; Meda, L.; Borodin, O.; Yushin, G. Protons Enhance Conductivities in Lithium Halide Hydroxide/Lithium Oxyhalide Solid Electrolytes by Forming Rotating Hydroxy Groups. *Adv. Energy Mater.* **2018**, *8*, 1700971.
(368) Yao, Z.; Kim, S.; Michel, K.; Zhang, Y.; Aykol, M.; Wolverton, C. Stability and conductivity of cation- and anion-substituted LiBH 4 -based solid-state electrolytes. *Phys. Rev. Materials* **2018**, *2*, No. 065402.
(369) Li, W.; Ando, Y.; Minamitani, E.; Watanabe, S. Study of Li atom diffusion in amorphous Li3PO4 with neural network potential. *J. Chem. Phys.* **2017**, *147*, 214106.
(370) Qi, Y.; Xu, Q.; Van der Ven, A. Chemically induced crack instability when electrodes fracture. *J. Electrochem. Soc.* **2012**, *159*, A1838−A1843.

https://dx.doi.org/10.1021/acs.chemrev.9b00601
Chem. Rev. 2020, 120, 6977−7019